UC Irvine
UC Irvine Electronic Theses and Dissertations

Title

Studies of Electronic Structure and Proton-Coupled Electron Transfer in Transition-Metal Complexes Containing Redox-Active Ligands

Permalink

https://escholarship.org/uc/item/5fb6g63p

Author

Ramirez, Claudia Paola

Publication Date

2019

Peer reviewed|Thesis/dissertation

UNIVERSITY OF CALIFORNIA,
IRVINE

Studies of Electronic Structure and Proton-Coupled Electron Transfer in Transition-Metal
Complexes Containing Redox-Active Ligands

DISSERTATION

submitted in partial satisfaction of the requirements
for the degree of

DOCTOR OF PHILOSOPHY
in Chemistry

by

Claudia Paola Ramirez

Dissertation Committee:
Professor Alan F. Heyduk, Chair
Professor William J. Evans
Professor Shane Ardo

2019

DEDICATION

To

My mentors, friends, family, and Tig

TABLE OF CONTENTS

Page

LIST OF TABLES

LIST OF SCHEMES

LIST OF EQUATIONS

ACKNOWLEDGEMENTS

First, I would like to thank my advisor, Alan Heyduk. Thank you for mentoring and guiding me towards the most epic finish line I will ever cross. You are a thoughtful and meticulous scientist with just the right amount of skepticism, and I hope to keep growing in those aspects. You believed in me when I was to beat down to believe in myself. I still remember sitting in your office and you saying with so much conviction, "Mastering out is NOT an option." Your genuine belief in me gave me what I needed to keep going and that means so much to me. Being a part of your group allowed me to grow intellectually and gave me the ability to confidently talk about my chemistry in a way I could have never imagined when I first arrived at UCI. Thank you for giving me that place to grow. Last but not least, I will never forget taking your physical inorganic class. Classes were so hard for me, but you were able to teach difficult material in a way that I could understand (for the most part) and you continually teach us things even if they are "basic gen chem experiments". Thank you for being a great teacher. I'm excited to see where my career takes me, and I can't thank you enough for your part in my journey; third choice and all!

I also have so much gratitude for my thesis committee members, Shane Ardo and Bill Evans. Shane, you have a contagious passion for science and the work that you. I really admire that and wherever I go I want to have that same kind of love for the work that I do every day. Thank you for allowing me to be a part of your group and providing your continuous support. Being a part of a new research group taught me to be independent early on and a little more fearless in the lab, and I am so grateful for that experience. Bill, you were the reason I came to UCI and you and your group made me feel so welcomed and gave me a sense of belonging. It was my first experience in a chemistry research lab and working with a glovebox and everyone in the group helped mentor me to learn the ropes. The group was a great reflection of you. You are inquisitive,

detail-oriented, and so kind. Six years later I still reference the packet from organometallics class; that thing is so useful. Throughout my journey you have always been there to talk science, give me advice and lemons! Thank you for believing in me when I doubted myself and for helping me reach this incredible milestone in my life.

Andy, even though you were not on my committees you have always shown me such incredible support. You were always checking in on me, my chemistry, and my running and I appreciate that so much. I will always remember an exercise you did during one of your group meetings. You walked in with a big wooden beam and had students walk across the beam. They did it easily and you asked what it would be like to try to walk across the beam if it was suspended between two buildings. Of course, everyone agreed that it wouldn't be quite as easy because we would be afraid of falling. Till this day, any time I am procrastinating because I am letting fear keep me from trying a reaction or prep that is out of my comfort zone, I remember that and force myself to just go do it. You have also inspired me to be an engaging speaker and educator. Thank you!

Of course, a special thank you to Jenny Yang and all the inorganic community at UCI. You all make this an amazing place to learn and grow. The work here would not be possible without the wonderful UCI facilities. I am particularly grateful to Joe Ziller and all the x-ray fellows who helped me obtain every piece of structural data.

To the incredible friends that I have made during my time at UCI. You are all great scientist with unique strengths, and I feel so fortunate to have been able to share my PhD with you all. Victoria, Jordan, Jen, David, Bronte, and Mikey thank you all for helping me grow as a scientist and individual. I love you all very much.

Victoria, you are so fierce yet equally kind. I am constantly inspired by your work ethic and will power. You have been a part of my journey from the very beginning and being able to share every step of this science marathon with you has made the tough times more manageable and the victories that much sweeter. Most importantly, thank you for taking on a real marathon with me! I look forward to keeping the running tradition alive and sharing many more professional victories together.

Jen you are so sharp and a natural problem solver. I am so grateful that we crossed paths in Shane's group because you are like the older sister I never had. You were a huge part of my life during my toughest time in graduate school and having your support was so crucial. You always had my back, whether it was to hear me talk about the same problems repeatedly, go get a good workout in, or just go out and have a good time. Thank you for bringing back the joy for me! You are so motivated and a true fighter. I have no doubt that you are going to be an incredibly accomplished scientist.

Mikey and Bronte, my dream team! The best part of these last two years was getting to share every single day with you two. From moving gloveboxes and getting through tough subgroups to sharing our academic victories and drinking wine in Temecula. At some point we moved past lab mates and became a little family that is so incredibly special to me. You both continuously inspire me to be a better scientist and teammate so thank you for that.

A mis papas, gracias por todo el amor y apoyo incondicional que me han dado por estos treinta años. Gracias a su trabajo y sacrificio he podido realizar todos mis sueños y metas. Con sus mismas acciones me han demostrado como ser una persona dedicada y trabajador, pero que permanece humilde. Gracias por siempre estar presente en vida, por darme una familia con mucho amor y atención. Ustedes me han educado sobre las cosas más importantes en la vida, las cosas

que no se aprenden en la escuela. Siempre han demostrado que es más importante dar que recibir y me inspiran a ser igual de generosa que ustedes. Espero poder darles todo lo que me han dado a mí. ¡Los quiero mucho!

Alexis, you have been my partner in crime since the very beginning and I know that as long as you are around, I will never be alone. I am so proud of the woman you have become and feel so lucky to have you as my sister. Thank you for teaching me to speak my mind and be a little tougher. I can't wait to see where life takes us, and I want you to know that I would fight someone for you too!

Lastly, to my sunshine and soon-to-be husband, Tig. Thank you for the unconditional love and support you have provided through the end of this journey. You have brought so much fun and spontaneity into my life but have respected my need to stay committed to this process. I know that I would still be here without you but having you in my life has made reaching the finish line so much easier. This is OUR accomplishment now and getting to share every moment of this with you makes it so much sweeter. Change and the unknown can be terrifying but knowing that you will always be there makes me feel fearless. I can't wait to start the next chapter of our lives together, wherever that may be. I love you; let the new adventures begin!

CLAUDIA P. RAMIREZ

EDUCATION

University of California Irvine, Irvine, CA
Doctor of Philosophy, Chemistry, GPA: 3.6   June 2013−May 2019
Advisor: Professor Alan F. Heyduk

St. Mary's University, San Antonio, TX
Bachelor of Science in Chemistry, Minor: Biology, GPA: 3.8   June 2011

Chaminade University, Honolulu, HI
St. Mary's University Marianist Student Exchange Program   Spring 2010

RESEARCH EXPERIENCE

Graduate Researcher, University of California Irvine, Irvine, CA   December 2013−Present

- Synthesized a series of platinum and palladium complexes containing a redox-active ligand with a protic N-H bond for which the pK_a and bond dissociation free energy were determined using spectroscopic and electrochemical techniques. Reactivity were carried out to demonstrate the hydrogen atom noninnocence at the ligand.
- Expanded the fundamental understanding of charge transfer in group 10 molecular dyes for solar energy conversion through the synthesis of air-sensitive metal complexes using air-free glovebox and Schlenk-line techniques.
- Used of x-ray diffraction, density functional theory, electrochemical, and spectroscopic studies to analyze the influence of complex charge and metal ion identity on the electronic structure of transition-metal complexes.
- Synthesized iridium coordination compounds and CdSe quantum dots and characterized them using absorbance and fluorescence spectroscopy in efforts to develop inorganic photoacids with excited-state reactivity.

Summer Student Researcher, UCI Competitive Edge Program, Irvine, CA   July 2013−September 2013

- Synthesized and characterized highly air and moisture sensitive rare-earth complexes in efforts to increase stability and promote reactivity with substrates such as N_2 and CO_2

Production Chemist, Blue Line Corporation, San Antonio, TX   May 2011−May 2013

- Performed analyses, tests, and research experiments in connection with the development of new and improved rare-earth metal salts and solutions.
- Responsible for the calibration and upkeep of analytical instruments as well as managing the inventory of samples and laboratory reagents.
- Performed routine analysis of raw materials, intermediates, and final products and generated the pertinent certificates of analysis.
- Proficiently used production calculators to generate batch tickets used by plant technicians in manufacturing and developed production calculators for new products.
- Managed the mass-production of $LaCl_3$ solution and produced efficiency reports for the customer by thoroughly tracking and analyzing raw materials and products.
- Collaborated with R&D chemist to develop a method to reprocess a waste stream and recover

lanthanide material.

Research Intern, PURE Program: UT Health Science Center, San Antonio, TX   June 2010–August 2010

- Participated in research in a retinal neurobiology laboratory using immunochemistry techniques to quantify and compare the amount of the chloride co-transporter, KCC2, in the retina of control and diabetic mice.

TEACHING EXPERIENCE

Teaching Assistant, University of California, Irvine, Irvine, CA   September 2013–Present

General Chemistry Laboratory Teaching Assistant
- Trained entry-level students in laboratory safety, lab notebook use, and proper laboratory principles and techniques such as: electronic absorption spectroscopy, acid-base titrations, colligative properties, and calorimetry.

Advanced Inorganic Chemistry Laboratory Teaching Assistant
- Trained senior-level students in proper research level laboratory techniques including air-free manipulations using Schlenk-line, high vacuum line, and glove box techniques during the synthesis and characterization of classic inorganic metal complexes.

Discussion Leader for Inorganic Chemistry and General Chemistry
- Taught chemistry problem solving skills to entry, honors and majors, and senior level students by leading engaging discussion sessions.
- Helped students develop a thorough understanding of difficult topics by presenting information using creative methods and analogies.

Analytical & General Chemistry Laboratory Head TA
- Work in collaboration with the professor to manage course materials, organize and process grades, advise and mentor course TAs, and serve as a resource for students.
- Developed and incorporated writing lessons and assignments that taught entry level general chemistry students how to write scientific lab reports as part of a year-long teaching project.

Chemistry Tutor, Pinnacle Tutoring Services   December 2017–Present

- Review class material and coach chemistry high school students through practice problems and homework assignments.

Tutor, St. Mary's University Learning Assistance Center   August 2009–December 2009

- Reviewed class material and provided exam reviews on a one-on-one basis or in groups of up to six students for organic chemistry and general biology.

PRESENTATIONS
- "Electronic Coupling in Ligand-Centered Mixed-Valence Complexes of Nickel, Palladium, and Platinum," American Chemical Society National Meeting, March 2018
- "Electronic Coupling in Ligand-Centered Mixed-Valence Complexes of Nickel, Palladium, and Platinum," UCI Inorganic Seminar Series, January 2018
- "Design and Photophysical Characterization of Inorganic Coordination Compounds for Studies of Excited-state Proton Transfer", SoCal Organometallics Meeting, April 2016
- "Why MLCT Excited-States Make Poor Photoacids and How to Overcome It," American Chemical Society National Meeting, March 2016

- "Inorganic Photoacids as Visible-Light Absorbers for Artificial Proton Pumps," Southern California Inorganic Photochemistry Conference, September 2014
- "Rare-Earths: Exploring the +2 Oxidation State," UCI Competitive Edge Summer Research Program, August 2013

PUBLICATIONS

In preparation: Ramirez, C.P., Wojnar, M.K., Ziller J.W., and Heyduk A.F., "Understanding Ligand-Ligand Coupling in Mixed-Valent Complexes of Redox-Active Ligands." Submitting to RSC Chemical Science

AWARDS

Contributions to Education by a Chemistry Department TA 2016
Awarded to a TA that cultivates excellent rapport with students and goes above what is required for the TA assignment
Chemistry Department Pedagogical Fellowship 2015
Awarded to an outstanding graduate student TA who will help with the TA Trainer program for the upcoming year
Michael E. Gebel Award 2015
Awarded to a student working in environmental chemistry with broader life experience before graduate school
Blue Star Award, Employee of the Quarter 2012
Employee of the Quarter Award at Blue Line Corporation
Competitive Undergraduate Education Program Award 2009
Travel award to attend the 2009 Society of Toxicology Annual Meeting

SKILLS

Languages: Spanish (Fluent)
Computer: Microsoft Word, Excel, PowerPoint, MATLAB, Turbomole
UCI Center for Engaged Instruction: Student-Centered Course Design Certification

COMMUNITY SERVICE

Big Sister Mentor, Big Brothers Big Sisters Orange County January 2016–March 2017
Volunteer, Ardo Group Chemistry Outreach Fall 2014–June 2016
Volunteer, Iota Sigma Pi: Chemistry Day at the Zoo Fall 2013
Team Leader, Susan G. Komen Race for the Cure Spring 2012–Spring 2013
Volunteer, Kinetic Kids Basketball Fall 2012

ABSTRACT OF THE DISSERTATION

Studies of Electronic Structure and Proton Coupled Electron Transfer in Transition-Metal Complexes Coordinated to Redox-Active Ligands

By

Claudia Paola Ramirez

University of California, Irvine, 2019

Professor Alan F. Heyduk, Chair

The series of projects discussed in this dissertation are linked by the universal theories of electron transfer and proton-coupled electron transfer. Each work has focused on the synthesis and characterization of transition metal complexes containing redox-active ligands.

The ability to understand and subsequently manipulate interligand interactions between redox-active ligands bound to the same metal center is the focus of the work presented in *Chapter 2*. A series of square-planar metal complexes containing a group 10 metal and the redox-active ligand, 3,5-di-*tert*-butyl(2,6-diisopropylphenyl)-*ortho*-iminosemiquinonate (isq$^{\bullet-}$), were prepared and used to generate the mixed-valence, one-electron reduced species $[M(isq^{\bullet})(ap)]^-$ and one-electron oxidized species $[M(isq^{\bullet})(iq)]^+$. The degree of ligand-ligand coupling was determined by calculating the electronic coupling parameter, H_{ab}. The mixed-valence anions are strongly delocalized Class III complexes, whereas the mixed-valence cations fall into the Class II regime. The effect of metal ion on ligand-ligand communication follows a less-pronounced, but non-Periodic trend with H_{ab} values following the trend Pt > Ni > Pd.

An understanding of the influence of metal choice and complex charge allowed the work to progress towards the generation of ligand frameworks that are also proton active. *Chapter 3*

details the synthesis of a family of donor–acceptor Pd(II)/Pt(II) complexes coordinated to a bipyridyl acceptor ligand and 2,4-di-tert-butyl-6-(phenylamino)phenol ([^{H}apH$_2$]) or one of its derivatives, [^{R}apH$_2$] (R = H, CF$_3$, OMe, Me$_2$) as the donor ligand. Protonation of the amidophenolate amine was carried out to generate protonated cationic complexes of the form [M(^{R}ap**H**)(^{X}bpy)]$^{1+}$ (R = H, CF$_3$, OMe, Me$_2$; X = H, *t*Bu). Subsequent pK_a measurements and reactivity studies with galvinoxyl$^•$ confirmed that the [^{R}ap**H**]$^{1-}$ ligand framework could act as a redox, proton, and hydrogen-atom noninnocent ligand. These systems provide a deeper understanding of the factors that influence BDFE values and how they can be modulated to control the thermodynamics of hydrogen-atom transfer.

Lastly, *Chapter 4* describes previous work that ties together that investigates excited-state proton transfer in transition-metal complexes. The synthesis and photophysical characterization of a series of low-spin d^6 iridium compounds was carried out to probe their viability as inorganic photoacids or photobases for intermolecular excited-state proton-transfer reactions. [Ir^{III}(2-(3-hydroxyphenyl)pyridine)$_2$(N^N)]PF$_6$,) complexes, where N^N = 1,10-phenanthroline (**Ir-phen**), 2,2'-biquinoline (**Ir-bq**), or 4,4'-di-*tert*-butyl-2,2'-bipyridine (**Ir-dtb**), were investigated as potential photoacids and [Ir(2-(3-methoxyphenyl)pyridine)$_2$(2,2'-biquinoline-4,4'-dicarboxylic acid)]PF$_6$ and [Ru^{II}(bipyridine)$_2$(dcbq)] as potential photobases. Spectroscopic characterization showed that functionalizing the ligand scaffold with a protic functional group quenches the intense photoluminescence observed in prototypical iridium-based emitters. This unforeseen result hindered the ability to measure excited state pK_a values by fluorescence titrations. Further analyses of the electronic structure and potential quenching mechanisms of the complexes must be done in order to make the structural changes required to promote long-lived excited states with large ΔpK_a values.

Chapter 1
Introduction

Charge Transfer and Transition-Metal Coordination Compounds

Electron-transfer is one of the simplest, yet most fundamental types of chemical reactions. It is considered a critical link between the subdisciplines of chemistry and has widespread applications in fields like biology and physics. Review articles on the topic argue that our very own existence is dependent on the process of electron transfer because most life forms depend on photosynthesis for energy production.[1] This universal relevance has promoted the research of synthetic molecular systems that are capable of carrying out efficient electron transfer processes. An intramolecular oxidation-reduction process in a transition metal complex can be classified into three main types: (1) metal-to-ligand charge transfer, (2) ligand-to-metal charge transfer, and (3) ligand-to-ligand charge transfer.[2,3] Metal-to-ligand charge-transfer (MLCT) and ligand-to-ligand charge-transfer (LL'CT) are the two pertinent types for the work described herein and their respective molecular orbital diagrams are depicted in Figure 1.1 and 1.2 respectively.[4,5]
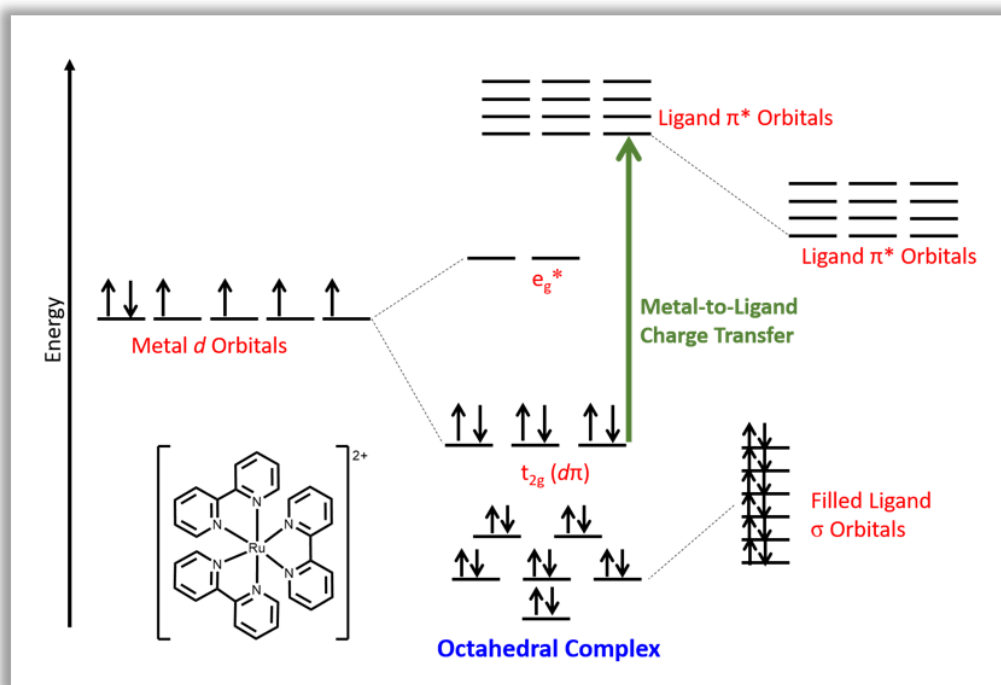
Figure 1.1. Simplified molecular orbital diagram for an octahedral (ML_6) transition metal complex with π acceptor ligands.
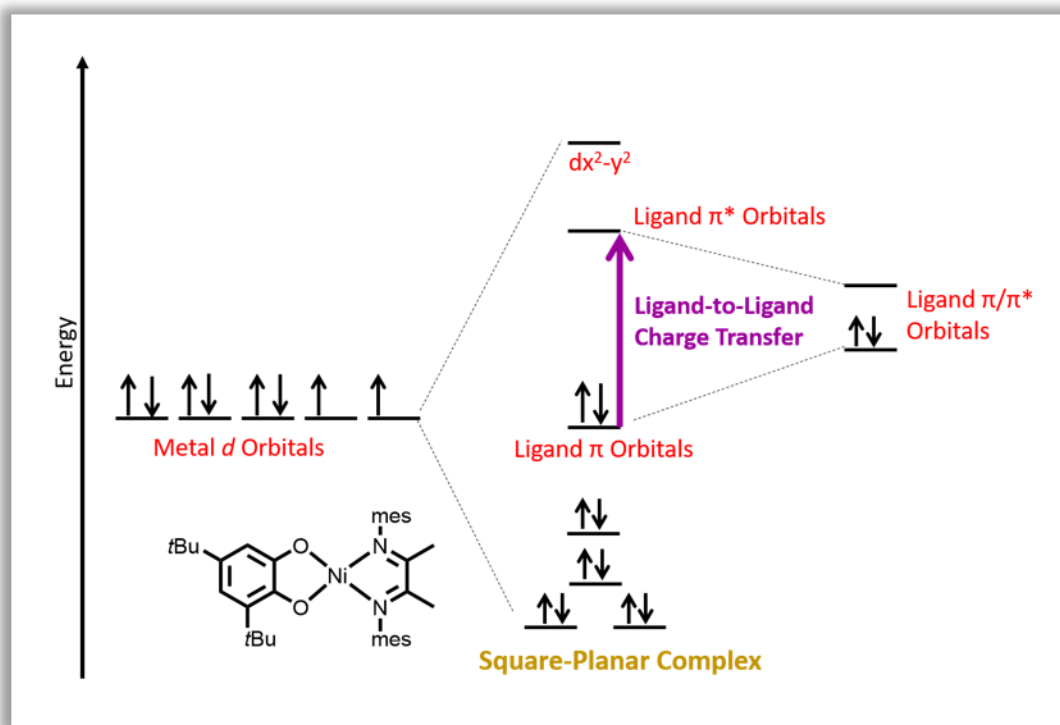
Figure 1.2. Simplified molecular orbital diagram for a square-planar (ML_4) transition metal complex with π acceptor ligands.

The MLCT depicted in Figure 1.1 occurs from a metal-based t_{2g} orbital (HOMO) to an empty ligand-based π* orbital (LUMO). In the case of LL'CT (Figure 1.2), the filled metal orbitals lie below the filled ligand orbitals. As a result, the electron-transfer occurs from a largely ligand-based HOMO to ligand π* LUMO. Due to their tunable optical transitions and redox properties, charge-transfer complexes have attracted attention as "light harvesters" for electron-transfer reactivity. The quintessential example of a MLCT complex is $[Ru(bpy)_3]^{2+}$ (bpy = 2,2-bipyridine). The excited-state electronic structure of $[Ru(bpy)_3]^{2+}$, ruthenium complexes with related polypyridyl ligands, and isoelectronic (d^6) complexes of Os^{II}, Rh^{III}, and Ir^{III} have been heavily investigated in efforts to harness excited-state reactivity. The studies of these systems have focused on a multitude of applications, including dye-sensitized solar cells, sensing, displays, solar fuels, and artificial photosynthesis.[6–10] In 1974, electron transfer from the excited-state of $[Ru(bpy)_3]^{2+*}$

was first reported by Whitten and Meyer. They demonstrated the excited-state quenching of $[Ru(bpy)_3]^{2+*}$ by electron transfer to methyl viologen dication (MV^{2+}) using flash photolysis as outlined by the reactions in Scheme 1.1.[11,12]
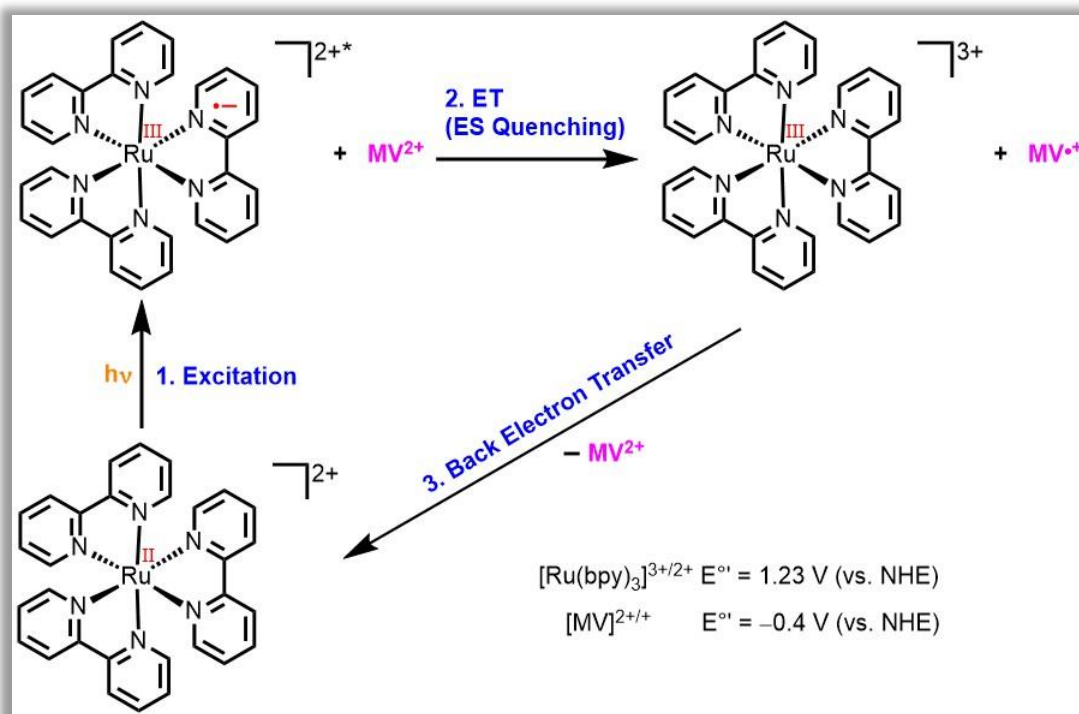
Scheme 1.1. Electron transfer from the MLCT excited state of $[Ru(bpy)_3]^{2+}$ to methyl viologen. Scheme adapted from reference 6.

This result was incredibly exciting because it occurred shortly after the discovery of Fujishima and Honda who reported that direct band gap excitation of TiO_2 in a photoelectrochemical cell resulted in the successful splitting of water into hydrogen and oxygen.[13] While limited to UV excitation, this finding was incredibly significant because it suggested that synthetic materials could mimic the natural photosynthesis apparatus and use sunlight to generate fuels by "artificial photosynthesis".[9,14] The ruthenium reactions in Scheme 1.1 can be described in terms of key energy conversion steps that would outline a potential molecular approach to artificial photosynthesis. In reaction (1) $[Ru(bpy)_3]^{2+}$ absorbs visible light to generate the excited-state

$[Ru(bpy)_3]^{2+*}$. This reaction is the "light-harvesting" step that allows $[Ru(bpy)_3]^{2+*}$ to store the light absorbed in the molecular excited state. In reaction (2), electron-transfer quenching of the $[Ru(bpy)_3]^{2+*}$ excited-state converts 2.1 eV of excited-state free energy to 1.7 eV of transiently stored redox energy as $MV^{\bullet+}$ and $[Ru(bpy)_3]^{3+}$. The quenching reaction products, $[Ru(bpy)_3]^{3+}$ and $MV^{\bullet+}$ are thermodynamically capable of splitting water based on their redox potentials – $E^{\circ'} =$ 1.23 V (vs. NHE) for the $[Ru(bpy)_3]^{3+/2+}$ couple and $E^{\circ'} = -0.4$ V for $MV^{2+/+}$. However, the electron transfer processes described by reaction 1 and 2 are ineffective due to back electron-transfer from $MV^{\bullet+}$ to $[Ru(bpy)_3]^{3+}$ (Scheme 1.1, reaction 3) and loss of the redox equivalents as heat. Nonetheless, these discoveries provided a chemical approach to artificial photosynthesis and promoted the research of transition-metal complexes as light harvesters for energy conversion and reactivity such as water splitting or reducing CO_2 to carbon fuels.[15–22]

Charge-transfer complexes have also been investigated as molecular dyes for dye-sensitized solar cells.[23–31] The charge-transfer excited-state allows the molecular dye, which is anchored to the surface of a semi-conductor, to be the light absorber, electron donor, and electron acceptor. As a result, it can directly generate the photoinduced charge separated state that is necessary to convert light energy to chemical energy and transfer the charge to the material according to the mechanisms of the device (Figure 1.3, *left*). The advantages of using a coordination complex are that (1) it provides direct optical charge-transfer and (2) the electrochemical and spectroscopic properties can be readily tuned through synthetic modification of the transition-metal complex. Although MLCT complexes like $[Ru(bpy)_3]^{2+}$ have been used, our group has been interested in using redox-active ligands to design donor–acceptor complexes with ligand-to-ligand' charge-transfer.[24,29] In a MLCT complex the donor is localized on the metal ion, and the only way to tune the energetics of the donor is by changing the metal identity, which

may not be synthetically feasible. In LL'CT complexes, the frontier molecular orbitals are localized on the redox-active ligands with metal valence orbitals residing at lower energies Ligand-based redox orbitals increase design modularity while avoiding the inefficiencies of separate light-absorbing and electron-transfer steps. Our group has demonstrated the flexibility of donor–acceptor complexes through the design and characterization of a series square-planar nickel (II) complexes using redox-active catecholate donor ligands and redox-active diimine acceptor ligands as shown in Figure 1.3 (right).[29] Systematic variation of the donor and acceptor ligands demonstrated that the electronic and electrochemical properties of LL'CT complexes could be readily tuned by changing the identity of the redox active ligand or altering the functional groups on an existing ligand.
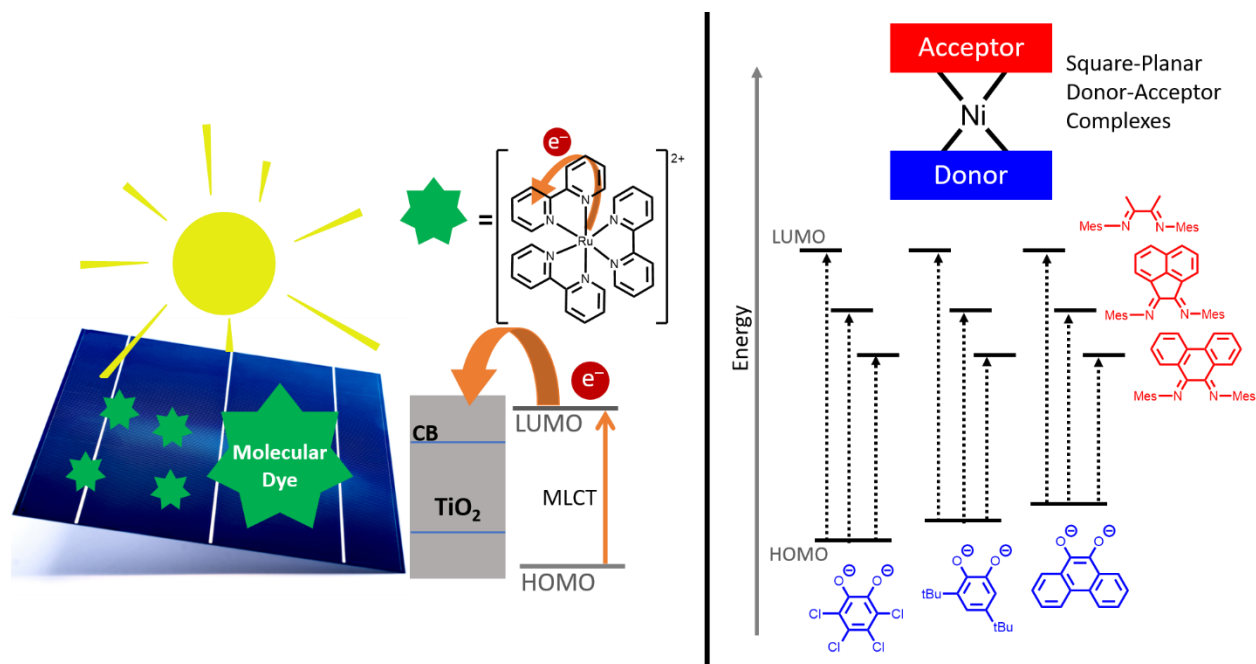
Figure 1.3. (*Left*) Schematic of a MLCT molecular dye attached to the surface of a semi-conductor to function as the light absorber. (*Right*) Nickel(II) LL'CT dyes designed to provide an array of spectroscopic and electrochemical properties. Figure adapted from reference 29.

Redox-active ligands have attracted the attention of coordination chemists over several decades for the unique electronic properties that they engender in transition metal complexes.

Early work on bis(dithiolene) complexes with nickel as the bridging metal ion, demonstrated that a redox-active ligand could undergo facile one-electron transfer reactions while coordinated to a metal ion (Scheme 1.2) – establishing a foundation for the analysis of redox reactions in transition-metal complexes containing redox-active ligands.[32–36] Computational studies revealed significant ligand–metal mixing at the frontier molecular orbitals along with systems in which the filled metal-based orbitals were lower in energy than the ligand orbitals. This supported experimental evidence that suggested redox events were taking place on the ligand rather than on the metal as shown in Scheme 1.2.
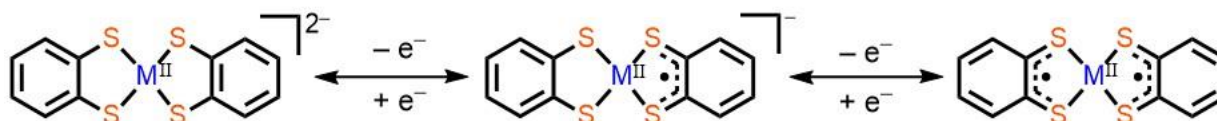
Scheme 1.2. Square-planar bis(dithiolene) complex with sequential one-electron oxidations that demonstrate the ligand noninnocence; adapted from reference 32.

Cognate ligand-based redox activity has been investigated in nickel, palladium, and platinum complexes with catechol, *ortho*-aminophenol, and *ortho*-phenylenediamine type ligands to elucidate the electronic structure and spectroscopic, electrochemical, and magnetic properties of each system.[37–42] The unique electronic structures have made coordination complexes of redox-active ligands attractive candidates for a variety of other applications including electrically conductive materials[43–45] and the development of catalysts for multi-electron reactions.[46–48]

Ligand-to-Ligand Charge-Transfer Complexes and Mixed-Valency

In order to design efficient redox-active ligand complexes, it is important to understand the interligand interactions that occur between two or more redox-active ligands bound to the same metal center. Learning how ligand interactions are influenced by the identity of the metal bridge was the motivation for the work described in *Chapter 2*. Symmetric bis(iminosemiquinonate)

metal (II) complexes were chosen as a suitable representation of the previously reported LL'CT dyes and probed in their mixed-valence forms in order to measure the electronic delocalization in each system. The theory of mixed-valency provided an avenue to analyze the magnitude of ligand-ligand coupling and identify the factors that significantly influence ligand coupling. A mixed-valence system is defined as a molecular structure that contains two identical redox sites connected by a bridging moiety that facilitates the exchange of valence electrons between the two sites. Upon reduction or oxidation, an odd electron is introduced into the system which inadvertently serves as an electronic structure probe. In a localized mixed-valence system the radical will be valence trapped and selectively reside at one redox site – generating a system with two identical redox sites in different oxidation states. In a strongly coupled system, the electron is delocalized between the two sites – generating a system where the two redox sites are in "valence-averaged" oxidation states. The strength of the electron exchange between the two sites determines the optical, electrochemical, and magnetic properties and is used two classify the degree of delocalization in the mixed-valence complex. The first example of a mixed-valence complex was the Creutz-Taube ion, $[(NH_3)_5Ru^{II}\text{-pyrazine-}Ru^{III}(NH_3)_5]^{5+}$, first reported in 1969 by Creutz and Taube (Figure 1.4).[49] This system and all its derivatives were used to elucidate how the identity, size, and functional group profile of the bridge influenced electron transfer and electron delocalization between to redox-active metals in a dinuclear complex.
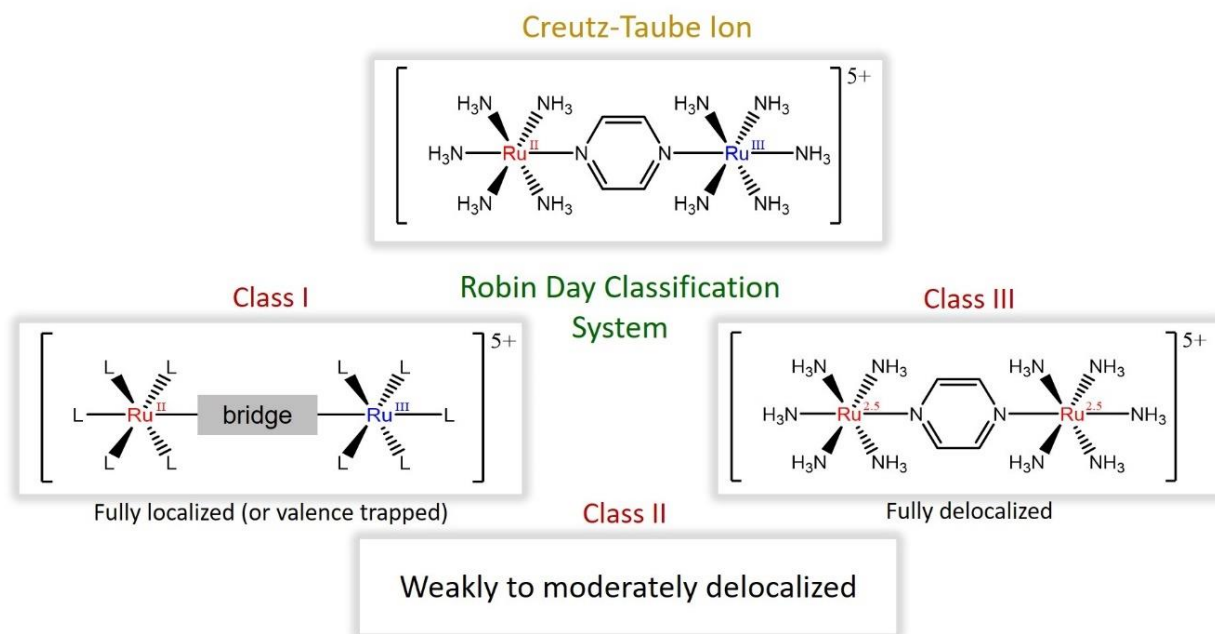
Figure 1.4. (*Top*) Creutz-Taube ion, the first synthetic example of a mixed-valence complex. (*Bottom*) The Robin-Day Classification System used to categorize the degree of delocalization in mixed-valence complexes.

According to the Robin-Day classification, mixed-valence molecules can be categorized into one of three classes based on the degree of electronic delocalization (Figure 1.4).[50] Class I systems are fully localized (or valence trapped), and as a result, the properties of the complex are consistent with those observed for the distinct, unperturbed redox sites. Class II systems are moderately delocalized and display new properties in addition to those of the separate sites. Lastly, Class III systems are fully delocalized and display new and unique properties that are not observed for the individual redox sites. It is important to note that making an assignment is not consistently a clear-cut process. At the Class II-III borderline ambiguity in the electronic structure increases and impedes on the ability to make definite assignments within that region. As a result, a more thorough classification system, described below, can be applied to quantify the electronic coupling between two redox sites.

The classical description of mixed-valency was developed by Hush in 1967. Hush used Marcus theory to relate the properties of the charge-transfer band to the activation barriers for electron transfer to establish the Marcus-Hush quantification of delocalization (Figure 1.5).[51]
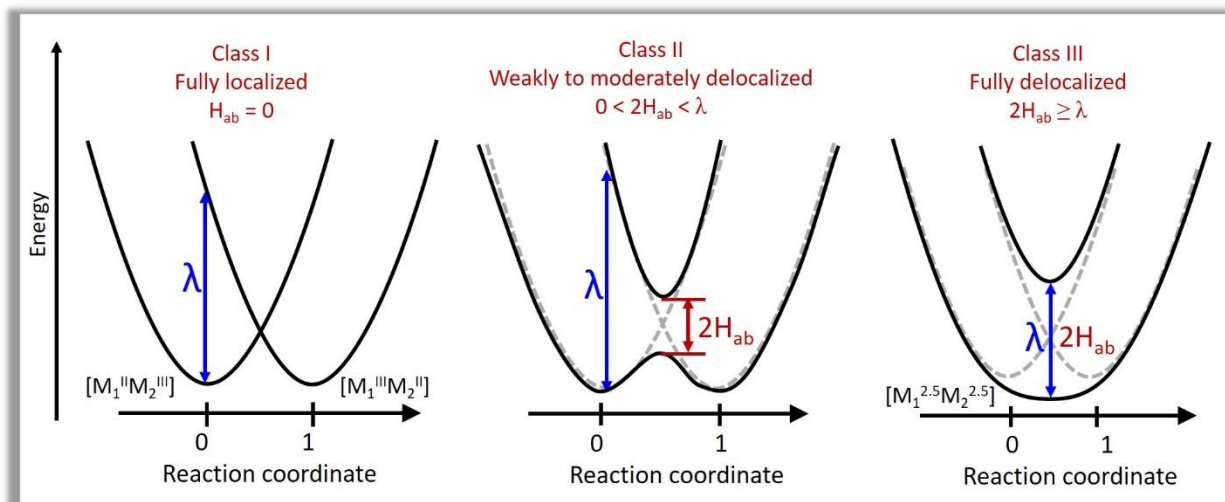
Figure 1.5. The classical theory of mixed-valence compounds developed by Hush. (*Left*) Localized Class I system (nonadiabatic states). (*Center*) Moderately delocalized Class II system. (*Right*) Fully delocalized Class III system (nonadiabatic states).

As shown in Figure 1.5, solid line parabolas are used to represent the wave functions for two potential energy surfaces; one for reactants (Ψ_a) and one for products (Ψ_b). In a Class I system, each parabola represents a unique valence isomer, $[M_1^{II}M_2^{III}]$ and $[M_1^{III}M_2^{II}]$, which contain each of the metal ions in two distinct oxidation states. The free energies of the diabatic states are defined by H_a and H_b as shown in equation 1.1a and 1.1b, where $\hat{H}$ is the effective two-state Hamiltonian operator, λ is the reorganization energy, and X varies from 0 to 1 as the reaction proceeds.

$$H_a = \langle \varphi_a | \hat{H} | \varphi_a \rangle = \lambda X^2 \qquad (1.1a)$$

$$H_b = \langle \varphi_b | \hat{H} | \varphi_b \rangle = \lambda(X - 1) \qquad (1.1b)$$

$$H_{ab} = \langle \varphi_a | \hat{H} | \varphi_b \rangle \qquad (1.2)$$

In a localized Class I system the electronic coupling between the two redox sites, defined as H_{ab}, is zero. As a result, λ is the reorganization energy required to optically excite the electron from the donor to the acceptor. In a Class II system, the two redox sites experience weak to moderate coupling which removes the degeneracy and generates a lower and higher energy surface (Figure 1.5, *center*). The splitting between the two surfaces defines the electronic coupling parameter, H_{ab} (Equation 1.2). This is the operator used to mix the individual wavefunctions to create the symmetric and antisymmetric waves. The energies of the adiabatic states, obtained by solving the two-state secular determinant, are given by Equation 1.3a and 1.3b.

$$G_1 = \frac{1}{2}\left\{(G_b + G_a) - [(G_b - G_a)^2 + 4H_{ab}^2]^{1/2}\right\} \qquad (1.3a)$$

$$G_2 = \frac{1}{2}\left\{(G_b + G_a) - [(G_b - G_a)^2 + 4H_{ab}^2]^{1/2}\right\} \qquad (1.3b)$$

The difference between the adiabatic energies is given by Equation 1.4 and as seen in Figure 1.5 the splitting at the intersection ($X = 0.5$) is $2H_{ab}$.

$$(G_2 - G_1) = \left\{[\lambda(1 - 2X)]^2 + 4H_{ab}^2\right\}^{1/2} \qquad (1.4)$$

A vertical transition between the two adiabatic states is called an intervalence charge transfer (IVCT) because the transfer of an electron results in an exchange of valency. As H_{ab} increases, the larger splitting between the two adiabatic states is countered by the reactant and product wells moving closer together so that the energy of the transition (hν) is equal to the reorganization energy (λ). In a class II system, $2H_{ab}$ is greater than zero but less than the energy of the transition (λ). In a class III system, the two redox sites are strongly coupled, and the electron is fully delocalized. The ground state surface now has one minimum and the optical transition does not involve net charge transfer because it is occurring between delocalized molecular orbitals of the systems. In the fully

delocalized state, each site is more accurately defined with an average valence state of $[M_1^{2.5}M_2^{2.5}]$ and $2H_{ab}$ is $\geq \lambda$. For Gaussian-shaped IVCT bands, H_{ab} can be calculated using equation 1.5, where ν_{max} is the energy of the transition, ε_{max} is the intensity, r_{ab} is the electron transfer distance, and $\Delta\nu_{1/2}$ is the full-width at half maximum. However, a more rigorous quantum mechanical formula, which can be applied regardless of band shape, is given by equation 1.6. Here μ is the transition dipole moment, which can be calculated from the integrated intensity of the absorption band, and e is the elementary charge of an electron.

$$H_{ab} = \frac{2.06 \times 10^{-2}(\nu_{max}\varepsilon_{max}\Delta\nu_{1/2})^{1/2}}{r_{ab}} \qquad (1.5)$$

$$H_{ab} = \frac{|\mu|}{er_{ab}}\nu_{max} \qquad (1.6)$$

Since their development, these methods have been used extensively to analyze the electronic coupling in multi-metallic mixed-valence systems bridge by organic linkers.[52–54] However, less is known about the analogous ligand-based mixed-valency in which the electronic coupling between two redox-active ligands is mediated by a bridging metal ion.[55–62] The goal of the ligand-based mixed-valency studies discussed herein is to provide insight on how the bridging metal ion can be used to tune the nature of the electronic ground-state and electron-transfer reactivity.

Proton-Coupled Electron Transfer

Related to the fundamental process of electron transfer is proton-coupled electron transfer (PCET). The term PCET was first coined in 1981 to describe the concerted transfer of electrons and protons as observed in the comproportionation reaction between $[Ru^{IV}(bpy)_2(py)(O)]^{2+}$ and $[Ru^{II}(bpy)_2(py)(OH_2)]^{2+}$ shown in Scheme 1.3.[63] In this reaction, an electron and proton are

transferred from the aquo species, $[Ru^{II}(bpy)_2(py)(OH_2)]^{2+}$, to the oxo species, $[Ru^{IV}(bpy)_2(py)(O)]^{2+}$ to generate two hydroxo species, $[Ru^{III}(bpy)_2(py)(OH)]^{2+}$.

$$[Ru^{IV}(bpy)_2(py)(O)]^{2+} + [Ru^{II}(bpy)_2(py)(OH_2)]^{2+} \underset{3 \times 10^3 \text{ M}^{-1} \text{ s}^{-1}}{\overset{2.5 \times 10^5 \text{ M}^{-1} \text{ s}^{-1}}{\rightleftharpoons}} 2[Ru^{III}(bpy)_2(py)(OH)]^{2+}$$
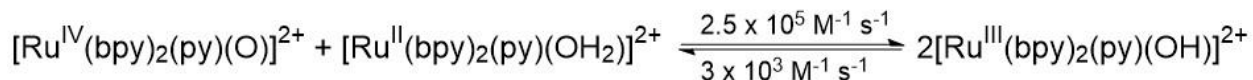
Scheme 1.3. Proton-coupled electron transfer in the comproportionation reaction between $[Ru(bpy)_2(py)(O)]^{2+}$ and $[Ru(bpy)_2(py)(OH_2)]^{2+}$. Scheme adapted from reference 63.

However, PCET is now more broadly used to describe reactions and half reactions where both electrons and protons are transferred regardless of the mechanism. PCET is at the heart of successful energy conversion and energy storage reactions which often require the buildup and transfer of multiple electrons and protons. This process is eloquently demonstrated in nature during processes like photosynthesis. During photosynthesis, plants use light harvesting chromophores like *chlorophyll a* to capture light energy and drive the conversion of CO_2 to carbohydrates, such as glucose, which stores light energy in the form of chemical bonds (Figure 1.6). The reduction of CO_2 to make glucose requires the transfer of 24 electrons (e$^-$) and 24 protons (H$^+$); photosynthesis highlights the remarkable ability of nature to perform large-scale PCET reactions.
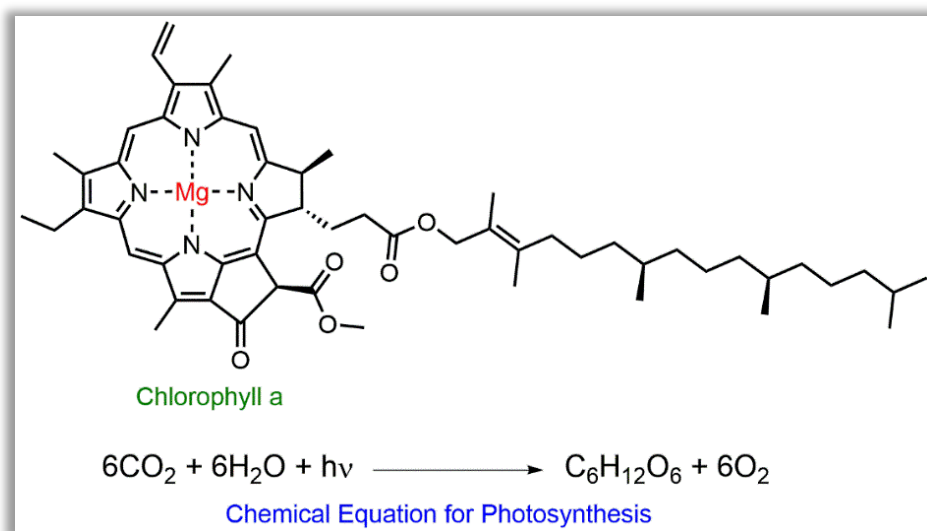
Figure 1.6. (*Top*) Chlorophyll a, the chromophore used as the primary sunlight absorber for photosynthesis. (*Bottom*) The chemical equation for the reduction of CO_2 to glucose carried out during photosynthesis.

13

Hydrogen atom transfer (HAT) and hydride transfer are two types of PCET. HAT has been distinguished from electron-proton transfer (EPT) by being defined as a reaction in which the electron (e^-) and proton (H^+) are transferred from the same reactant orbital (or bond).[64] However, this definition is considered restrictive and becomes problematic when considering the mechanism. As a result, Mayer et al. define HAT as concerted hydrogen atom ($H^\bullet$) transfer, where concerted means the process occurs in one kinetic step from one donor to one acceptor.[65] A wide range of transition metal-based systems capable of mediating PCET reactions have been investigated over the last few decades. Typically, these systems undergo a redox event at the metal center and protonation/deprotonation at the ligand. The most common type of PCET is shown in Scheme 1.3 (shown above) where a metal hydroxide complex, $[Ru^{II}(bpy)_2(py)(OH_2)]^{2+}$, interconverts with the one-electron oxidized metal-oxo species, $[Ru^{IV}(bpy)_2(py)(O)]^{2+}$. Alternatively, metal hydride complexes are also well known for carrying out HAT reactions. The difference in a metal hydride complex is that the electron and proton are both coming from the metal center. The thermochemical properties of a transition-metal PCET reagent are outlined by the thermodynamic cycle in Scheme 1.4 below. The HAT reagent is analyzed by measuring the homolytic bond dissociation free energy (BDFE) which is determined from the compound's pK_a and redox potential ($E°'$) using equation 1.6;[66–69] where the solvent constant, C_G, is equivalent to the $H^+/H^\bullet$ standard reduction potential in that solvent.

M^n-LH → pKₐ (M^n-LH) → $[M^n$-L$]^-$

$E^{\circ\prime}$ ($[M^n$-LH$])^{+/0}$ **BDFE** $E^{\circ\prime}$ ($[M^n$-L$])^{0/-}$

$[M^{n+1}$-LH$]^+$ → pKₐ ($[M^{n+1}$-LH$]^+$) → M^{n+1}-L
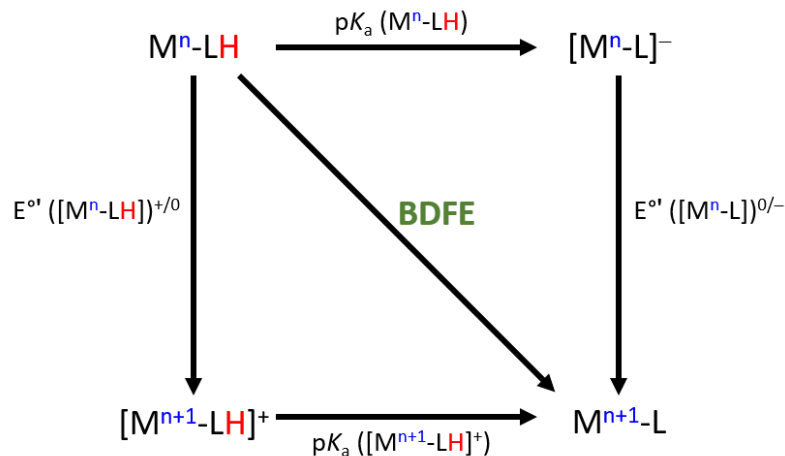
Scheme 1.4. Thermodynamic cycle of a transition metal PCET system.

$$BDFE = 1.37\big(pK_a(MH)\big) + 23.06(E'^{\circ}) + C_G \qquad (1.7)$$

While transition metal complexes containing redox-active ligands have been extensively used to store and transfer redox equivalents for PCET reactions, the development and incorporation of hydrogen atom (H$^\bullet$) or hydride (H$\mathbf{:}^-$) donor ligands is a more contemporary concept. A ligand that is redox-active and contains an acidic hydrogen atom can act as a H$^\bullet$ or H$\mathbf{:}^-$ donor. Given the importance of multi-electron and multi-proton reactivity discussed above, the design of ligand platforms that can manage proton and electron equivalents can provide new avenues in small molecule activation and catalysis.[65,70–72] The development of such frameworks must be coupled with a thorough understanding of the fundamental thermodynamic and kinetic properties of these ligands to promote their implementation. With that objective in mind, a series of complexes containing redox-active ligands that include an "active" proton that can be delivered with one electron to effect net hydrogen-atom transfer reactivity are described in *Chapter 3*.

Excited-State Proton-Coupled Electron Transfer

The highly desirable optical properties of the MLCT and LL'CT complexes discussed make them opportune candidates for photochemical reactivity. In certain molecules, photoexcitation can

15

result in an excited-state electronic structure that is significantly different from the ground-state which is capable of triggering reactivity that was not possible in the ground-state molecule. This phenomenon is commonly observed in protic molecules where light excitation causes changes in the acid-base properties and triggers PCET. Studies of excited-state PCET reactions have helped elucidate the reaction mechanisms of photosynthetic systems and what factors influence excited-state PCET. For example, it is well-known that photoexcitation can result in electronic structure changes that greatly alter proton affinity and pK_a values.[63,73–75] This is the premise for the development of photoacids and photobases, which are a class of molecules that undergo a drastic decrease or increase in pK_a, respectively, upon optical excitation. Figure 1.7 shows the well-known photoacid, 2-naphthol, and the changes in charge distribution that occur when it is photoexcited (λ_{ex} = 320–330 nm). The changes in charge distribution cause the pK_a value to decrease by 6.4 units in the excited-state.[76] This behavior demonstrates that photoacids/photobases provide a way to optically trigger local changes in pH and induce chemical reactivity.
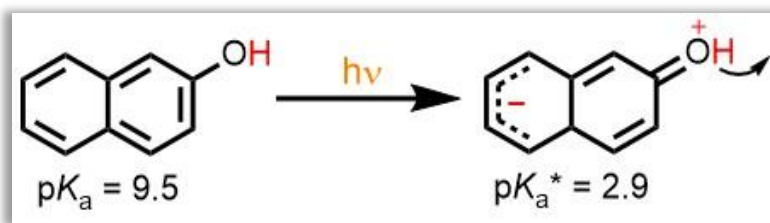
Figure 1.7. Charge redistribution that occurs in the excited-state of 2-naphthol and drives a decrease in the pK_a value of the O–H bond. Figure adapted from reference 63.

Excited-state PCET can also occur from the excited-state of luminescent MLCT complexes.[77] Many of the complexes explored in recent years for this type of reactivity are Ru(II), Os(II), Re(I), and Ir(III) complexes coordinated to ligands with protic moieties.[78] For proof of concept, Freys et al. demonstrated concerted EPT between the iridium complex, [IrbiimH$_2$]$^+$, and the electron–proton acceptor, 3,5-dinitrobenzoate anion (dnb⁻), shown in Figure 1.8 (*left*).[79] The iridium

complex forms a hydrogen-bonded adduct with the base and upon photoexcitation, transfers an electron and subsequent proton to the base. The spectroscopic changes observed for $[IrbiimH_2]^+$ and formation of Hdnb were used to monitor proton release to the base. In application driven studies, Nocera et al. investigated PCET reactions in Ru(II) and Re(I) complexes coordinated to tyrosine-like ligands as a means to model electron transfer in Photosystem II and study the mechanisms and the factors influencing ET. In these studies, the MLCT excited states of Ru and Re were quenched and the subsequent oxidation of tyrosine was monitored by laser flash photolysis. These experiments demonstrated that the PCET reactions had a pH dependence for intramolecular oxidation of the tyrosine-like ligand in both metal systems.[80,81] Related systems have been heavily investigated to mimic biological systems, elucidate mechanisms and rates, and probe the influence of factors like pH, temperature, kinetic isotopes, hydrogen bonding, and ligand field effects.[63]
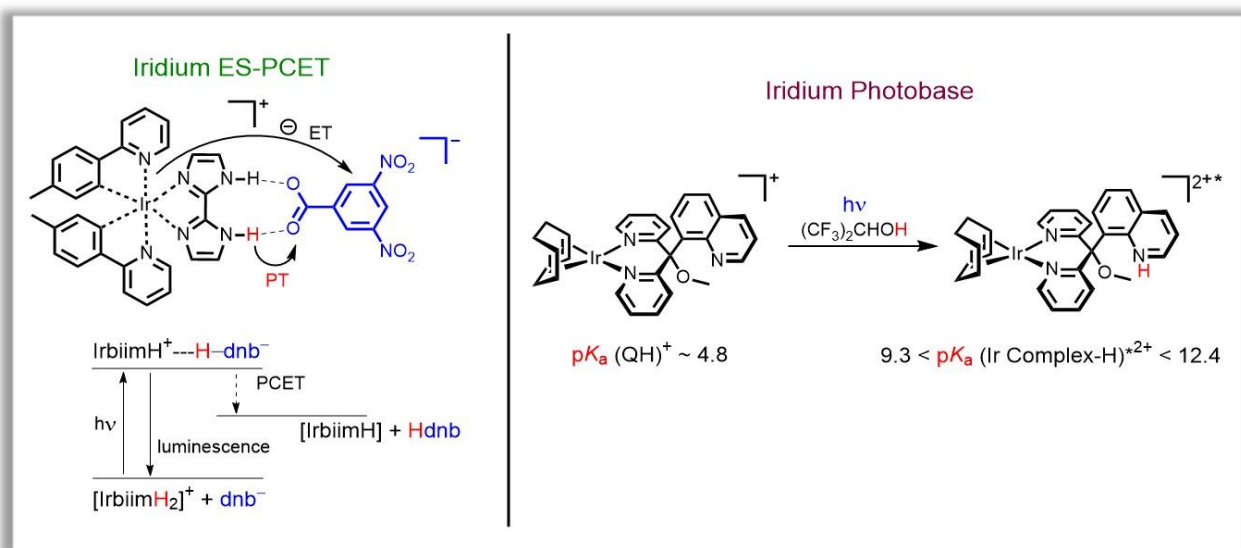
Figure 1.8. (*Left*) Excited-state proton-coupled electron transfer from a heteroleptic iridium complex to the base, 3,5-dinitrobenzoate anion. Figure adapted from reference 63 and 79. (*Right*) Example of an iridium photobase that shows an increase in the pK_a of the amine after photoexcitation. Figure adapted from reference 82.

The aim of the coordination complexes described *Chapter 4* is to use iridium-based MLCT photoacids to trigger the release of protons and generate a protonic circuit for energy production. A current example of such a system was recently reported by Dawlaty and Williams and is shown in Figure 1.9 (*right*).[82] Their report details the synthesis and characterization of an iridium compound with a pendant quinoline, for which the pK_a can be optically controlled. Spectroscopic studies demonstrated that in the ground state the iridium complex has a similar pK_a to that of free quinonline, $pK_a = 4.8$. Upon photoexcitation, the iridium complex deprotonates hexafluoroisopropyl alcohol (HFIPA) ($pK_a = 9.3$); indicating that the pK_a of the coordinated quinoline has increased and is at least greater than 9.3. However, unlike free quinoline, the excited-state complex could not deprotonate 2,2,2-trifluoroethanol (TFE) which has a pK_a of 12.4. This data allowed them to bracket the excited state pK_a (pK_a^*) of the iridium complex: $9.3 < pK_a^* < 12.4$. They also report that these systems are now being investigated to understand the mechanisms, expand the ligand scope, and apply the systems to catalytic conversions.

Contributions of This Work

Central to the application of redox-active ligand complexes as electron reservoirs is the ability to manipulate interligand interactions between two or more redox-active ligands bound to the same metal center (or bridge). The work presented in *Chapter 2* attempts to understand these ligand-ligand interactions through the mixed-valency formalism. A series of mixed-valent square-planar metal complexes containing the redox-active ligand, 3,5-di-*tert*-butyl(2,6-diisopropylphenyl)-*ortho*-iminosemiquinonate ($isq^{\bullet-}$), were characterized to confirm the redox loci and to determine the degree of ligand-ligand communication by calculating the electronic coupling parameter, H_{ab}. An understanding of the influence of metal choice and complex charge

on the electronics of the system allowed the work to progress towards the generation of ligand frameworks that are also proton noninnocent.

Chapter 3 details the synthesis of a family of donor–acceptor Pd/Pt(II) complexes coordinated to a bipyridyl acceptor ligand and an amidophenolate donor ligand, $[^{R}ap]^{2-}$. Protonation of the amidophenolate amine was carried out to generate protonated cationic complexes. Characterization and reactivity studies with galvinoxyl radical confirmed that the $[^{R}apH]^{1-}$ ligand framework can act as a redox, proton, and hydrogen-atom non-innocent ligand. These systems provide a deeper understanding of the factors that influence BDFE values and how they can be modulated to control the thermodynamics of HAT.

Lastly, *Chapter 4* describes previous work that ties together the theory of PCET with the MLCT excited state of metal complexes. Being that excited state proton transfer in inorganic coordination compounds could provide a way to control the instantaneous generation of protons, a series of low-spin d^6 iridium compounds were investigated to probe their viability as photoacids or photobases for intermolecular excited-state proton-transfer. The photoacids were intended for use in an integrated photovoltaic device that would convert photon energy into ionic power to desalinate seawater. The goal was to design an inorganic photoacid that would be the light absorber, deprotonate in the excited-state, and generate the protons/hydroniums ions needed for an ionic photocurrent and photovoltage.

References

(1)   Blondín, G.; Girerd, J.-J. *Chem. Rev.* **1992**, *92*, 365–368.

(2)   Gispert, J. R. *Coordination Chemistry*; Wiley-VCH, 2008.

(3)   Vogler, A.; Kunkely, H. *Comments Inorg. Chem.* **1990**, *9*, 201–220.

(4)   Miessler, G. L.; Fischer, P. J.; Tarr, D. A. *Inorganic Chemistry*; Pearson, 1991.

(5)   Kramer, W. W.; Cameron, L. A.; Zarkesh, R. A.; Ziller, J. W.; Heyduk, A. F. *Inorg. Chem.* **2014**, *53*, 8825–8837.

(6)   Thompson, D. W.; Ito, A.; Meyer, T. J. *Pure Appl. Chem.* **2013**, *85* (7), 1257–1305.

(7)   Song, W.; Chen, Z.; Brennaman, M. K.; Concepcion, J. J.; Otávio, A.; Patrocinio, T.; Murakami Iha, N. Y.; Meyer, T. J. *Pure Appl. Chem.* **2011**, *83* (4), 749–768.

(8)   Meyer, T. J. *Pure Appl. Chem.* **1986**, *58* (9), 1193–1986.

(9)   Meyer, T. J. *Acc. Chem. Res.* **1980**, *22* (5), 163–170.

(10)   Vos, J. G.; Kelly, J. M. *Dalt. Trans.* **2006**, No. 41, 4869–4883.

(11)   Bock, C. R.; Meyer, T. J.; Whitten, D. G. *J. Am. Chem. Soc.* **1974**, *96* (14), 4710–4712.

(12)   Young, R. C.; Meyer, T. J.; Whitten, D. G. *J. Am. Chem. Soc.* **1975**, *97*, 4781–4782.

(13)   Fujishima, A.; Honda, K. *Nature* **1972**, *238*, 37–38.

(14)   Alstrum-Acevedo, J. H.; Brennaman, M. K.; Meyer, T. J. *Inorg. Chem.* **2005**, *44*, 6802–6827.

(15)   Concepcion, J. J.; Jurss, J. W.; Brennaman, M. K.; Hoertz, P. G.; Patrocinio, A. O. T.; Iha, N. Y. M.; Templeton, J. L.; Meyer, T. J. *Acc. Chem. Res.* **1954**, *42* (12), 1954–1965.

(16)   Morris, A. J.; Meyer, G. J.; Fujita, E. *Acc. Chem. Res.* **2009**, *42* (12), 1983–1994.

(17)   Concepcion, J. J.; House, R. L.; Papanikolas, J. M.; Meyer, T. J. *Proc. Natl. Acad. Sci.* **2012**, *109*, 15560–15564.

(18)   Chen, Z.; Concepcion, J. J.; Brennaman, M. K.; Kang, P.; Norris, M. R.; Hoertz, P. G.; Meyer, T. J. *Proc. Natl. Acad. Sci.* **2012**, *109* (39), 15606–15611.

(19)   Kärkäs, M. D.; Verho, O.; Johnston, E. V; Åkermark, B. *Chem. Rev.* **2014**, *114*, 11863–12001.

(20)   Wang, W.-H.; Himeda, Y.; Muckerman, J. T.; Manbeck, G. F.; Fujita, E. *Chem. Rev.* **2015**, *115*, 12936–12973.

(21)   Karkas, M. D.; Li, Y.-Y.; Siegbahn, P. E.; Liao, R.-Z.; Åkermark, B. *Inorg. Chem.* **2018**, *57*, 10881–10895.

(22)   Dalle, K. E.; Warnan, J.; Leung, J. J.; Reuillard, B.; Karmel, I. S.; Reisner, E. *Chem. Rev.* **2019**, *119*, 2752–2875.

(23)   Aghazada, S.; Nazeeruddin, M. *Inorganics* **2018**, *6* (2), 52.

(24)   Cameron, L. A.; Ziller, J. W.; Heyduk, A. F. *Chem. Sci.* **2016**, *7*, 1807–1814.

(25)   Diwan, K.; Chauhan, R.; Singh, S. K.; Singh, B.; Drew, M. G. B.; Bahadur, L.; Singh, N. *New J. Chem.* **2014**, *38*, 97–108.

(26)   Islam, A.; Sugihara, H.; Hara, K.; Singh, L. P.; Katoh, R.; Yanagida, M.; Takahashi, Y.; Murata, S.; Arakawa, H.; Fujihashi, G. *Inorg. Chem.* **2001**, *40*, 5371–5380.

(27)   Geary, E. A. M.; Yellowlees, L. J.; Jack, L. A.; Oswald, I. D. H.; Parsons, S.; Hirata, N.; Durrant, J. R.; Robertson, N. *Inorg. Chem.* **2005**, *44*, 242–250.

(28)   Linfoot, C. L.; Richardson, P.; Mccall, K. L.; Durrant, J. R.; Morandeira, A.; Robertson, N. *Sol. Energy* **2011**, *85*, 1195–1203.

(29)   Kramer, W. W.; Cameron, L. A.; Zarkesh, R. A.; Ziller, J. W.; Heyduk, A. F. *Inorg. Chem.* **2014**, *53*, 8825–8837.

(30)   Achey, D.; Ardo, S.; Xia, H.-L.; Siegler, M. A.; Meyer, G. J. *J. Phys. Chem. Lett.* **2011**, *2*, 305–308.

(31)   Chou, C.-C.; Hu, F.-C.; Wu, K.-L.; Duan, T.; Chi, Y.; Liu, S.-H.; Lee, G.-H.; Chou, P.-T. *Inorg. Chem.* **2014**, *53*, 8593–8599.

(32)   Eisenberg, R.; Gray, H. B. *Inorg. Chem.* **2011**, *50*, 9741–9751.

(33)   Gray, H. B.; Williams, R.; Bernal, I.; Billig, E. *J. Am. Chem. Soc.* **1962**, *84* (18), 3596–3597.

(34)   Schrauzer, G. N.; Mayweg, V. *J. Am. Chem. Soc.* **1962**, *84* (16), 3221–3221.

(35)   Gray, H. B.; Billing, E. *J. Am. Chem. Soc.* **1963**, *85*, 2019–2020.

(36)   Davison, A.; Edelstein, N.; Holm, R. H.; Maki, A. H. *Inorg. Chem.* **1963**, *2* (6), 1227–1232.

(37)   Forbes, C. E.; Gold, A.; Holm, R. H. *Inorg. Chem.* **1971**, *10* (11), 2479–2485.

(38)   Davison, A.; Edelstein, N.; Holm, R. H.; Maki, A. H. *J. Am. Chem. Soc.* **1963**, *85* (13), 2029–2030.

(39)   Bachler, V.; Olbrich, G.; Neese, F.; Wieghardt, K. *Inorg. Chem.* **2002**, *41*, 4179–4193.

(40)   Herebian, D.; Bothe, E.; Neese, F.; Weyhermüller, T.; Wieghardt, K. *J. Am. Chem. Soc.* **2003**, *125* (30), 9116–9128.

(41)   Fox, G. A.; Pierpont, C. G. *Inorg. Chem.* **1992**, *31*, 3718–3723.

(42) Herebian, D.; Bothe, E.; Bill, E.; Weyhermu, T.; Wieghardt, K. *J. Am. Chem. Soc.* **2001**, *123*, 10012–10023.

(43) Xie, L. S.; Sun, L.; Wan, R.; Park, S. S.; Degayner, J. A.; Hendon, C. H.; Dincă, M. *J. Am. Chem. Soc.* **2018**, *140*, 7411–7414.

(44) Clough, A. J.; Skelton, J. M.; Downes, C. A.; de la Rosa, A. A.; Yoo, J. W.; Walsh, A.; Melot, B. C.; Marinescu, S. C. *J. Am. Chem. Soc.* **2017**, *139* (31), 10863–10867.

(45) Downes, C. A.; Marinescu, S. C. *ACS Catal.* **2017**, *7* (12), 8605–8612.

(46) Smith, A. L.; Hardcastle, K. I.; Soper, J. D. *J. Am. Chem. Soc.* **2010**, *132* (41), 14358–14360.

(47) Rajabimoghadam, K.; Darwish, Y.; Bashir, U.; Pitman, D.; Eichelberger, S.; Siegler, M. A.; Swart, M.; Garcia-Bosch, I. *J. Am. Chem. Soc.* **2018**, jacs.8b08748.

(48) Zarkesh, R. A.; Ziller, J. W.; Heyduk, A. F. *Angew. Chemie Int. Ed.* **2008**, *47* (25), 4715–4718.

(49) Creutz, C.; Taube, H. *J. Am. Chem. Soc.* **1969**, *91* (14), 3988–3989.

(50) Robin, M. B.; Day, P. *Advances in Inorganic Chemistry and Radiochemistry*; 1967.

(51) Hush, N. *Progress in Inorganic Chemistry Vol. 8*; 1967.

(52) Demadis, K. D.; Hartshorn, C. M.; Meyer, T. J. *Chem. Rev.* **2001**, *101*, 2655–2685.

(53) Crutchley, R. J. *Adv. Inorg. Chem.* **1994**, *41*, 273–325.

(54) Creutz, C. In *Progress in Inorganic Chemistry*; John Wiley & Sons, Ltd, 2007; pp 1–73.

(55) Lecarme, L.; Kochem, A.; Chiang, L.; Moutet, J.; Berthiol, F.; Philouze, C.; Leconte, N.;

Storr, T.; Thomas, F. *Inorg. Chem.* **2018**, *57*, 9708–9719.

(56) Kennedy, S. R.; Kozar, M. N.; Yennawar, H. P.; Lear, B. J. *Inorg. Chem.* **2016**, *55*, 8459–8467.

(57) Mews, N. M.; Berkefeld, A.; Hörner, G.; Schubert, H. *J. Am. Chem. Soc.* **2017**, *139* (7), 2808–2815.

(58) Shimazaki, Y.; Daniel, T.; Stack, P.; Storr, T. *Inorg. Chem* **2009**, *48*, 8383–8392.

(59) Kennedy, S. R.; Goyal, P.; Kozar, M. N.; Yennawar, H. P.; Hammes-Schiffer, S.; Lear, B. J. *Inorg. Chem.* **2016**, *55*, 1433–1445.

(60) Conner, K. M.; Perugini, A. L.; Malabute, M.; Brown, S. N. *Inorg. Chem.* **2018**, *57*, 3272–3286.

(61) Leconte, N.; Moutet, J.; Constantin, T.; Molton, F.; Philouze, C.; Thomas, F. *Eur. J. Inorg. Chem.* **2018**, *2018* (16), 1752–1761.

(62) Nguyen, M. T.; Jones, R. A.; Holliday, B. J. *Macromolecules* **2017**, *50* (3), 872–883.

(63) Weinberg, D. R.; Gagliardi, C. J.; Hull, J. F.; Murphy, C. F.; Kent, C. A.; Westlake, B. C.; Paul, A.; Ess, D. H.; Mccafferty, D. G.; Meyer, T. J. *Chem. Rev.* **2012**, *112*, 4016–4093.

(64) Mayer, J. M. *Acc. Chem. Res.* **2011**, *44* (1), 36–44.

(65) Warren, J. J.; Tronic, T. A.; Mayer, J. M. *Chem. Rev.* **2010**, *110*, 6961–7001.

(66) Bordwell, F. G.; Cheng, J.-P.; Harrelson, J. A. *J. Am. Chem. Soc* **1988**, *110*, 1229–1231.

(67) Wayner, D. D. M.; Parker, V. D. *Angew. Chem., Int. Ed. Engl* **1993**, *26*, 287–294.

(68) Tilset, M. *Electron Transfer in Chemistry*; Balzani, V., Ed.; Wiley-VCH: Weinheim,

Germany, 2001.

(69)   Tilset, M. *Comprehensive Organometallic Chemistry III, Vol. 1*; Parkin, G., Ed.; Elsevier, 2007.

(70)   Rosenkoetter, K. E.; Wojnar, M. K.; Charette, B. J.; Ziller, J. W.; Heyduk, A. F. *Inorg. Chem.* **2018**, *57*, 9728–9737.

(71)   Mcloughlin, E. A.; Waldie, K. M.; Ramakrishnan, S.; Waymouth, R. M. *J. Am. Chem. Soc.* **2018**, *140*, 13233–13241.

(72)   Britt, R. D.; Sayler, R. I.; Berben, L. A.; Thompson, E. J.; Sherbow, T. J.; Arnold, A. *Chem. - A Eur. J.* **2018**, *25* (2), 454–458.

(73)   Tolbert, L. M.; Haubrich, J. E. *Photoexcited Proton Transfer from Enhanced Photoacids*; 1994; Vol. 116.

(74)   Liao, Y. *Acc. Chem. Res.* **2017**, *50*, 1956–1964.

(75)   Tolbert, L. M.; Solntsev, K. M. *Acc. Chem. Res.* **2002**, *35*, 19–27.

(76)   Rosenberg, J. L.; Brinn, I. *J. Phys. Chem.* **1972**, *76*, 3558–3562.

(77)   Wenger, O. S. *Chem. - A Eur. J.* **2011**, *17* (42), 11692–11702.

(78)   Vos, J. G. *Polyhedron* **1992**, *11* (18), 2285–2299.

(79)   Freys, J. C.; Bernardinelli, G.; Wenger, O. S. *Chem. Commun.* **2008**, No. 36, 4267–4269.

(80)   Irebo, T.; Reece, S. Y.; Sjödin, M.; Nocera, D. G.; Hammarström, L. *J. Am. Chem. Soc.* **2007**, *129* (50), 15462–15464.

(81)   Irebo, T.; Reece, S. Y.; Sjö, M.; Nocera, D. G.; Hammarström, L. *J. Am. Chem. Soc.* **2007**,

129, 15462–15464.

(82)   Demianets, I.; Hunt, J. R.; Dawlaty, J. M.; Williams, T. J.; Loker, K. B. *Organometallics*

       2019, *38*, 200–204.

Chapter 2

Understanding Ligand-Ligand Coupling in Square-Planar Mixed-Valence Complexes Containing Redox-Active Ligands Coordinated to a Group 10 Metal

2.1. Introduction

Redox-active or redox noninnocent ligands have attracted the attention of coordination chemists over several decades for the electronic properties that they engender in transition metal complexes and for the unique challenges that these complexes pose to the simple electronic structure and bonding models commonly used to predict properties and reactivity.[1–6] More recently, coordination complexes of redox-active ligands have been proposed for a variety of applications including as charge-transfer dyes, in conductive metal-organic frameworks (MOFs), and for the development of multi-electron catalysts.[7–15] In particular, simple coordination complexes containing two or more redox-active, catecholate-type ligands are often targeted for study given that a variety of ligand derivatives are readily accessible and the corresponding bis- and tris-ligand metal complexes are prepared readily.[16–25] Central to the application of these redox-active ligand complexes is the ability to manipulate interligand interactions between two or more redox-active ligands bound to the same metal center. The work presented herein attempts to understand these ligand-ligand interactions through the prism of mixed valency.

Square-planar redox-active ligand complexes of the Group 10 metals have received considerable attention since the discovery of non-innocent behavior in nickel(II) bis(dithiolene) complexes.[26–28] Analogous ligand-based redox activity has been observed in nickel, palladium, and platinum derivatives with ligands derived from catechol,[18,29] *ortho*-aminophenol,[16,17,30] and *ortho*-phenylenediamine,[20] among other congeners.[21,31–33] Invariably, these neutral complexes are diamagnetic, with early debate centering on the best description of their ground-state electron configuration: either as ligand-centered, singlet diradicals, $(sq^\bullet)M^{II}(sq^\bullet)$ (where $(sq^\bullet)^{1-}$ is the one-electron oxidized form of the ligand) or as rapidly-equilibrating, zwitterionic, "resonance" structures with closed-shell ligands, $(cat)M^{II}(q) \leftrightarrow (q)M^{II}(cat)$ (where $(cat)^{2-}$ is the reduced form

of the ligand and $(q)^0$ is the two-electron oxidized form of the ligand). Subsequent spectroscopic and computational investigations conclusively support the former, diradical formulation for complexes of the platinum triad.[16,17,20] A more detailed picture of this electronic structure was recently elaborated by Brown and coworkers, who described the strongly-coupled diradicals in terms of one-electron (i.e., "bonding") and two-electron (i.e., exchange) energy contributions.[32,33] This description further highlights the four electronic states derived from the interaction of the two ligand radicals in $M^{II}(sq^\bullet)_2$ complexes: the singlet diradical ground state, a low-lying triplet excited state, and two higher-energy, zwitterionic excited states.

Another way to assess ligand-ligand communication in square-planar metal complexes is to examine them in their mixed-valence forms. Group 10 coordination complexes of catecholate, *ortho*-amidophenolate, and *ortho*-phenylenediamide ligands complexes display rich, ligand-centered redox activity, typically showing five accessible oxidation states. The monoanionic and monocationic derivatives, shown in Scheme 2.1, are both examples of mixed-valence complexes. Whereas traditional mixed-valence complexes comprise metal-based redox sites bridged by an organic ligand,[34–38] in these complexes, ligand-based redox sites are bridged by a metal center.
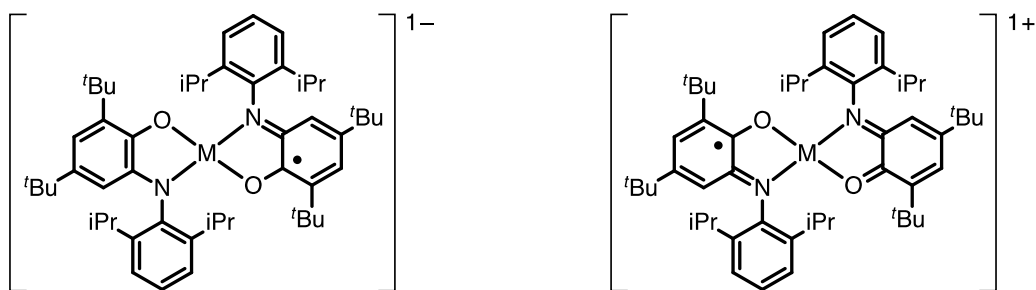
Scheme 2.1. Monoanionic and monocationic ligand-based mixed-valence complexes.

To develop a better understanding of the factors controlling ligand-ligand interactions in coordination complexes with multiple redox-active ligands, a series of square-planar nickel, palladium, and platinum complexes with two sterically-demanding redox-active ligands were

synthesized in both their monoanionic and monocationic mixed-valence forms. Characterization by structural, spectroscopic, and electrochemical techniques allowed for the analysis of these complexes within the Hush formalism to elucidate the factors that influence ligand-ligand communication.[39–41]

2.2. Results

2.2.1. Synthesis of Bis(iminosemiquinone) Complexes

The synthesis of square-planar nickel(II) complexes of bidentate redox-active ligands is well established in the literature. For the purposes of this study, it was critical that the metal complexes retain a four-coordinate geometry across multiple oxidation states and as such an *ortho*-iminobenzoquinone derivative with sterically demanding substituents was chosen. The reaction of 2,6-diisopropylaniline with 3,5-di-*tert*-butyl-1,2-benzoquinone afforded the *ortho*-iminobenzoquinone derivative 2,4-di-*tert*-butyl-6-(diisopropylphenylimino)-2,4-cyclohexadien-1-one (iq) in 83% yield according to the literature procedure.[42] As shown in Figure 2.1, the imine group of this ligand has isopropyl groups that should project above and below the plane of a square-planar coordination complex, helping to prevent coordination of a fifth ligand in an axial position. As with other *ortho*-iminobenzoquinone ligands, sequential one-electron reductions afford mono-anionic *ortho*-iminosemiquinonate, $(isq^{\bullet})^{1-}$, and dianionic *ortho*-amidophenolate, $(ap)^{2-}$, ligand oxidation states.
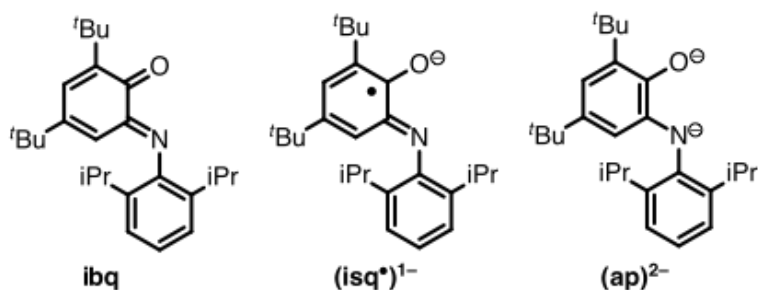
Figure 2.1. The redox active ligand, 2,4-di-*tert*-butyl-6-(diisopropylphenylimino)-2,4-cyclohexadien-1-one, and the sequential one-electron reductions it can undergo to access new oxidation states.

The symmetric bis-iminosemiquinone complexes were prepared by reacting zero-valent organometallic synthons of nickel, palladium, or platinum with two equivalents of the oxidized, *ortho*-iminobenzoquinone form of the ligand, as shown in Scheme 2.2. Attempts to prepare M(isq$^\bullet$)$_2$ complexes of nickel, palladium, and platinum starting from divalent metal halide salts gave poor yields or failed completely. While the nickel and palladium derivatives were prepared in good yields from Ni(cod)$_2$ and Pd$_2$(dba)$_3$, respectively, the corresponding platinum derivative could only be isolated in low yields, despite the implementation of more aggressive reaction conditions.
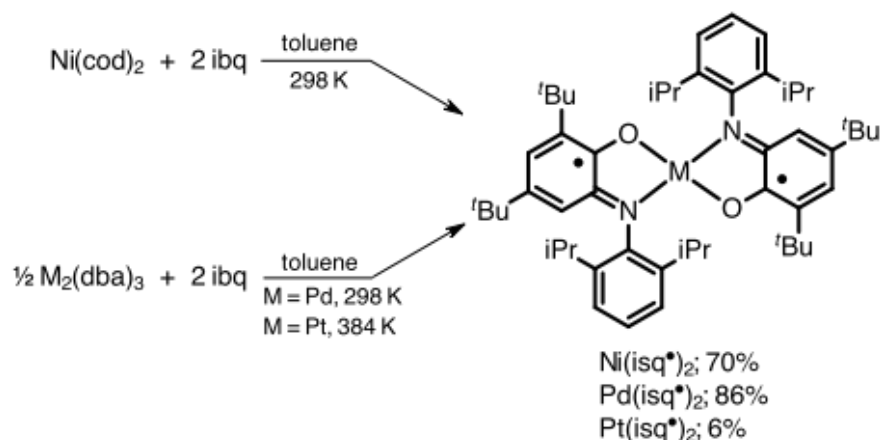
Scheme 2.2. Synthesis of the symmetric bis(iminosemiquinone) complexes.

The neutral bis-iminosemiquinone complexes of all three metals were structurally characterized by NMR spectroscopy in solution and by single-crystal X-ray diffraction in the solid

state. As has been reported previously, all three $M(isq^\bullet)_2$ complexes are diamagnetic in solution thanks to a singlet diradical ground-state electron configuration. Accordingly, the ^{1}H NMR spectra of the three complexes show sharp resonances in the normal diamagnetic region of the spectrum, consistent with C_{2h} symmetry in solution. This nominal symmetry is maintained in the solid state, as all three $M(isq^\bullet)_2$ complexes conform to the previously published metrics for square-planar, d^8 metals coordinated by two $(isq^\bullet)^{1-}$ ligands. The molecular structures of the three metal derivatives, $M(isq^\bullet)_2$ are shown in Figure 2.2 and selected metrical parameters for all three complexes are presented in Table 2.1. Notably, all three derivatives contain square-planar metal centers and two equivalent redox-active ligands. Intraligand C–O, C–N, and C–C bond distances are very similar for the nickel and platinum derivatives and can be used to calculate ligand metrical oxidation states (MOSs) of -1.11 ± 0.05 and -1.26 ± 0.08, respectively.[43] In the case of the palladium derivative, the calculated ligand MOS is -1.06 ± 0.05. These differences in MOS values are indicative of less π backbonding in the palladium derivative relative to the nickel and platinum derivatives.
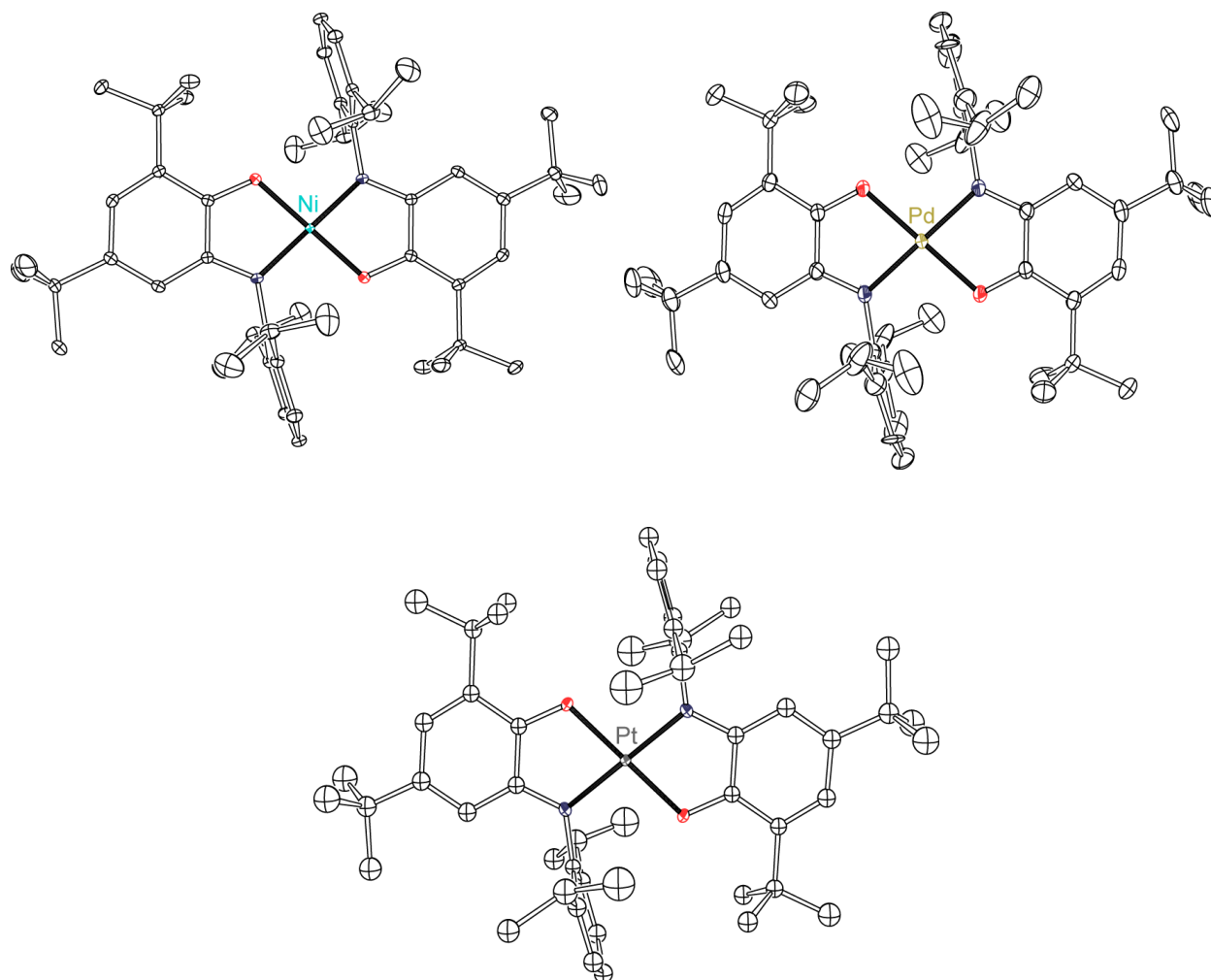
Figure 2.2. ORTEPs of Ni(isq•)₂ (*top left*), Pd(isq•)₂ (*top right*), and Pt(isq•)₂ (*bottom*). Ellipsoids are shown at 50% probability. Hydrogen atoms and solvent molecules have been omitted for clarity.

2.2.2. Synthesis of Mixed-Valence Monoanions

Addition of one electron to M(isq•)₂ complexes resulted in ligand-localized reduction and the generation of mixed-valence species characterized as [M(ap)(isq•)]⁻ monoanions. In a typical reaction, a THF solution of Ni(isq•)₂ was treated with one equivalent of decamethylcobaltocene (CoCp*₂) under an inert N₂ atmosphere resulting in a subtle color change from dark forest green to a dark blue-green. Concentration of the reaction solution and cooling to –35 °C resulted in the precipitation of the product, [CoCp*₂][Ni(ap)(isq•)], as a crystalline solid in 77% yield. The neutral palladium and platinum congeners were treated with CoCp*₂ under the same conditions,

which go from a dark indigo solution of a dark blue-green, affording [CoCp*$_2$][Pd(ap)(isq$^\bullet$)] and

[CoCp*$_2$][Pt(ap)(isq$^\bullet$)], respectively. In all three cases, the one-electron-reduced products were

paramagnetic, $S = \frac{1}{2}$, monoanions.
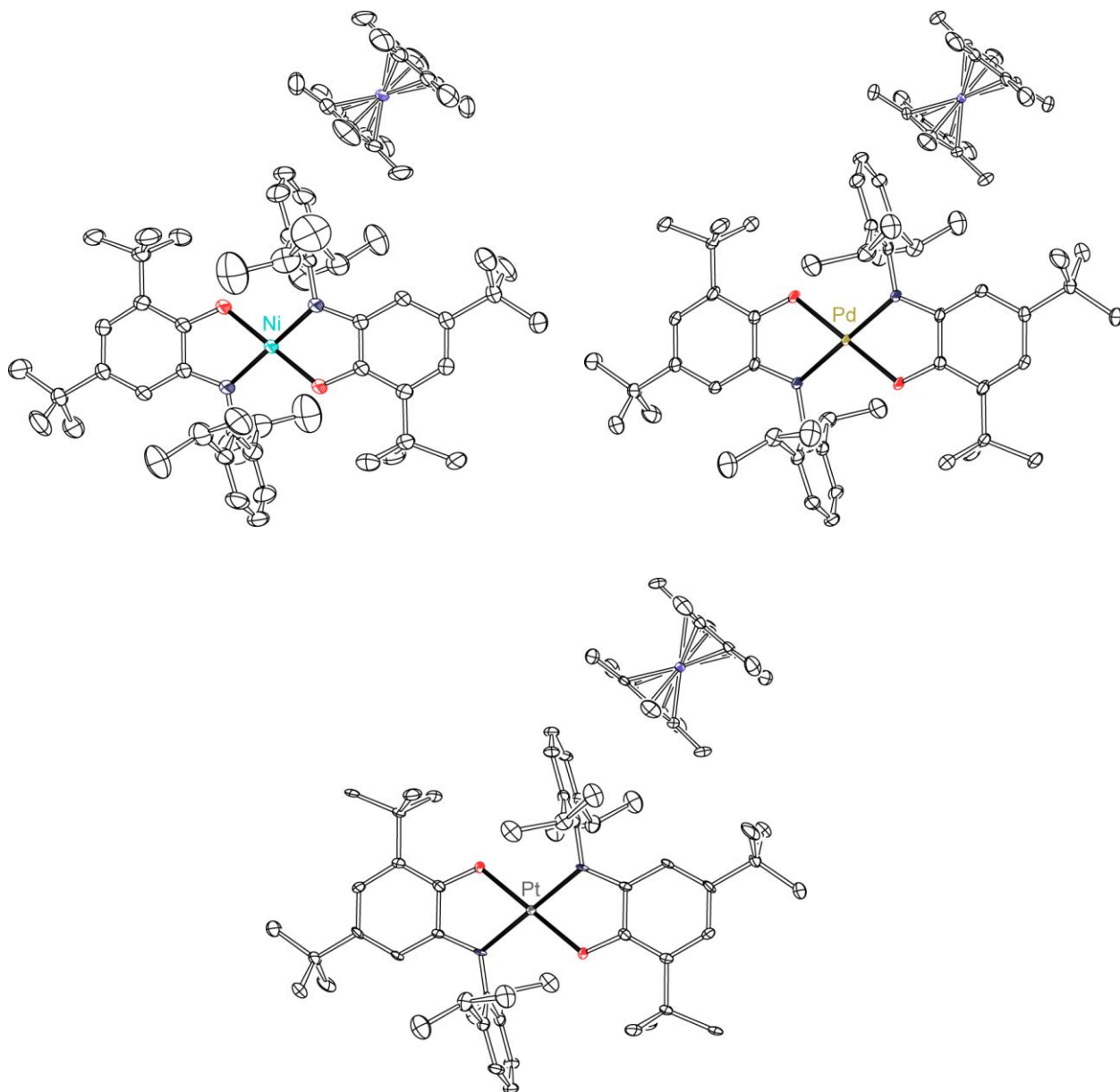
Figure 2.3. ORTEPs of [CoCp*$_2$][Ni(ap)(isq$^\bullet$)] (*top left*), [CoCp*$_2$][Pd(ap)(isq$^\bullet$)] (*top right*), and [CoCp*$_2$][Pt(ap)(isq$^\bullet$)] (*bottom*). Ellipsoids are shown at 50% probability. Hydrogen atoms and solvent molecules have been omitted for clarity.

Single-crystal X-ray diffraction experiments demonstrated that the one-electron-reduced monoanions for all three metals retain a four-coordinate, square-planar geometry about the central metal ion. Figure 2.3 shows an ORTEP of all three congeners. Select metrical data for all three monoanions are provided in Table 2.1. As with the neutral complexes, the bond angles around the nickel, palladium, and platinum metal centers can be used to calculate τ_4 values that range from 0 to 0.02, consistent with square-planar, d^8 metals. Small changes to the M–O and M–N bond lengths are observed for the reduced species relative to the neutral complexes. Again, the two redox-active ligands are crystallographically equivalent in the structures of all three monoanions, and calculated MOS values that fall between –1.55 and –1.60 are consistent with a one-electron reduction of the complex that is delocalized over both redox-active ligands.

2.2.3. Synthesis of Mixed-Valence Monocations

The mixed-valence monocations $[M(isq^\bullet)(ibq)]^+$ (M = Ni, Pd, Pt) were accessed by the removal of one electron from the neutral $M(isq^\bullet)_2$ complexes. Silver hexafluorophosphate proved to be a suitably strong oxidant, capable of generating the monocations for all three metals. Thus, the addition of solid $Ag[PF_6]$ to a CH_2Cl_2 solution of $Ni(isq^\bullet)_2$ resulted in a color change from green (Ni) or blue (Pd/Pt) to a red-purple color in one hour. After filtering to remove the silver byproduct, crystalline $[Ni(isq^\bullet)(ibq)][PF_6]$ was obtained from concentrated CH_2Cl_2 solutions of the product layered with pentane and chilled to –35 °C. Analogous procedures were used to generate the one-electron oxidized cations of the palladium and platinum derivatives. Consistent with a one-electron oxidation of $M(isq^\bullet)_2$, all three $[M(isq^\bullet)(ibq)][PF_6]$ products were characterized as paramagnetic, $S = \frac{1}{2}$ species.

Single-crystal X-ray diffraction experiments conducted on the cations $[Ni(isq^\bullet)(ibq)][PF_6]$ and $[Pd(isq^\bullet)(ibq)][PF_6]$, gave distinctly different results. Single crystals of the nickel derivative

were obtained by the diffusion of pentane into a CH_2Cl_2 solution of the complex at $-35\ ^\circ C$. The nickel complex, $[Ni(isq^\bullet)(ibq)][PF_6]$ (Figure 2.4, *left*), crystallized in the monoclinic space group *C*2/*c*, with a square planar nickel cation ($\tau_4 = 0$). As with the structures of the neutral and anionic derivatives discussed above, only one half of the $[Ni(isq^\bullet)(ibq)]^+$ cation is crystallographically unique. As shown in Table 2.1, the Ni–O bond distance is similar to those measured for the neutral and anionic derivatives; whereas, the Ni–N bond distance is elongated slightly. Intraligand bond distances gave a ligand MOS of 0.65 ± 0.08, which is consistent with averaging of a monoanionic $(isq^\bullet)^{1-}$ ligand and a neutral $(ibq)^0$ ligand.
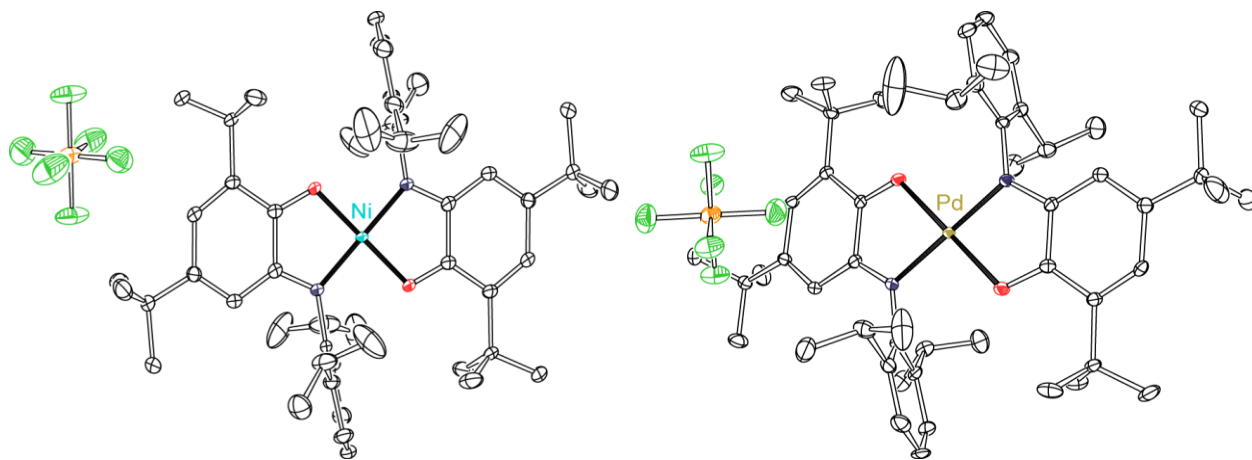
Figure 2.4. ORTEPs of $[Ni(isq^\bullet)(ibq)][PF_6]$ (*left*) and $[Pd(isq^\bullet)(ibq)][PF_6]$ (*right*). Ellipsoids are shown at 50% probability. Hydrogen atoms and solvent molecules have been omitted for clarity.

In the case of the palladium complex, $[Pd(isq^\bullet)(ibq)][PF_6]$ (Figure 2.4, *right*), the single-crystal X-ray structure revealed an unsymmetrical palladium complex cation, with resolved $(isq^\bullet)^{1-}$ and $(ibq)^0$ ligands. Crystals of the oxidized palladium derivative were obtained by diffusing toluene into a CH_2Cl_2 solution of the complex at $-35\ ^\circ C$. The palladium complex crystallized in the monoclinic space group $P2_1$, with a square planar palladium(II) cation ($\tau_4 = 0.04$). Unlike all other structures discussed above, the entire palladium cation is unique, revealing redox-active ligands in distinctly different oxidation states. As shown in Table 2.1, there are long and short Pd–

O and Pd–N bond distances. Intraligand C–O, C–N, and C–C bond distances were used to calculate two different ligand MOSs of -0.79 ± 0.08 and -0.30 ± 0.07, consistent with an $(isq^\bullet)^{1-}$ and an ibq ligand, respectively. The $[PF_6]^-$ anion sits above the plane of the neutral ibq ligand, with a shortest C···F distance of 2.98 Å.

Table 2.1. Metal-heteroatom bond distances (Å), τ_4 values, and ligand metrical oxidation state (MOS) values derived from the solid-state structures of $M(isq^\bullet)_2$, $[M(ap)(isq^\bullet)]^{1-}$, and $[M(isq^\bullet)(ibq)]^{1+}$ (M = Ni, Pd, Pt).

	$M(isq^\bullet)_2$ $[M(ap)(isq^\bullet)]^-$ $[M(isq^\bullet)(ibq)]^+$		
	M = Ni	**M = Pd**	**M = Pt**
M–O[a]	1.8402(11) 1.8491(17) 1.8450(19)	1.982(2) 1.998(2) 2.010(3); 1.984(3)	1.9850(16) 1.989(2) --
M–N[a]	1.8333(12) 1.8328(19) 1.848(2)	1.962(3) 1.954(3) 2.005(3); 1.965(3)	1.9398(19) 1.959(3) --
τ_4	0 0 0	0 0.02 0.04	0 0 --
MOS	-1.11 ± 0.05 -1.55 ± 0.09 -0.65 ± 0.08	-1.06 ± 0.05 -1.60 ± 0.07 -0.79 ± 0.08; -0.30 ± 0.07	-1.26 ± 0.08 -1.56 ± 0.14 --

2.2.4. Electrochemistry of $M(isq^\bullet)_2$ Complexes

Square-planar complexes of group 10 metal with redox-active ligands are known to have a rich manifold of redox processes. The redox processes of the Ni, Pd, Pt complexes reported here were examined using solution-phase voltammetric techniques. Figure 2.5 shows the cyclic voltammograms of $M(isq^\bullet)_2$ complexes dissolved in THF containing 0.1 M $[Bu_4N][PF_6]$ and referenced to $[Cp_2Fe]^{+/0}$ using an internal redox standard. Table 2.2 displays the redox processes observed for each complex between -3.0 V and $+1.0$ V vs $[Cp_2Fe]^{+/0}$. As is evident from Figure

2.5, the $M(isq^\bullet)_2$ complexes of Ni, Pd, and Pt each show four resolved one-electron redox processes: two reversible reductions and two (at least) partially reversible oxidations. Notably, the first reduction shows no dependence on the metal ion with the potentials falling within a narrow range of –1.19 to –1.21 V. The second reduction is more sensitive to the identity of the metal, showing a non-periodic trend. The second reduction of the palladium derivative occurred at –2.11 V while the second reduction of the nickel and platinum derivatives occurred at the more negative potentials of –2.27 V and –2.33 V, respectively. Both the first and second oxidation processes are sensitive to the metal ion, and the redox potentials follow a simple periodic trend with the nickel complex being oxidized at the mildest potentials and the platinum complex being oxidized at the most positive potentials.
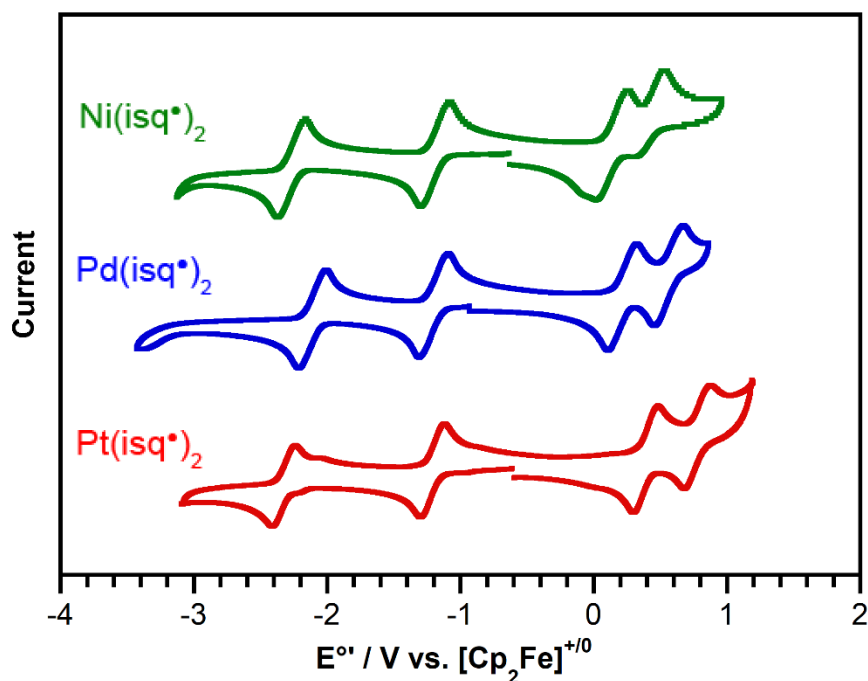
Figure 2.5. Cyclic voltammograms for $M(isq^\bullet)_2$ (M = Ni, Pd, Pt) dissolved in THF containing 0.1 M $[Bu_4N][PF_6]$ at 200 mV sec^{-1}.

Table 2.2. Reduction potentials (V vs $[Cp_2Fe]^{+/0}$) for $M(isq^{\bullet})_2$ (M = Ni, Pd, Pt) dissolved in THF containing 0.1 M $[Bu_4N][PF_6]$.

M	$E_1^{\circ\prime}$ $[M]^{2+/1+}$	$E_2^{\circ\prime}$ $[M]^{1+/0}$	ΔE_{ox} E_1-E_2	$E_3^{\circ\prime}$ $[M]^{0/1-}$	$E_4^{\circ\prime}$ $[M]^{1-/2-}$	ΔE_{red} E_3-E_4
Ni	0.42	0.14	0.28	−1.19	−2.27	1.08
Pd	0.56	0.21	0.35	−1.20	−2.11	0.91
Pt	0.78	0.39	0.39	−1.21	−2.33	1.12

2.2.5. Electronic Spectroscopy

Solution UV-vis-NIR spectra were measured for the neutral, anionic, and cationic complexes of nickel, palladium, and platinum, to elucidate their electronic structures. Of primary interest were the intense low-energy transitions typically associated with the frontier molecular orbitals of the redox-active ligands. The neutral diradical complexes, $M(isq^{\bullet})_2$, are highly colored both in the solid state and in solution, indicative of their strong absorption properties in the UV-vis-NIR regions of the electromagnetic spectrum. Figure 2.6(b) shows the absorption spectra of the nickel, palladium, and platinum derivatives in THF at 298 K and Table 2.3 gives key metrics from these spectra. The $M(isq^{\bullet})_2$ complexes have a characteristic band in the 10,000-15,000 cm^{-1} region with extinction coefficients above 30,000 M^{-1} cm^{-1}. These transitions are typically characterized as having both ligand-to-ligand charge transfer (LLCT) and $\pi \rightarrow \pi^*$ character.[16,17,44]

In the reduced $[M(ap)(isq^{\bullet})]^{1-}$ mixed-valence anions, the lowest-energy electronic absorption bands are shifted into the near-IR portion of the electromagnetic spectrum. As shown in Figure 2.6(a) and summarized in Table 2.3, the absorption spectra of the mixed-valence anions, $[M(ap)(isq^{\bullet})]^-$, are dominated by intense transitions with maxima that appear in the 6,400-9,100 cm^{-1} region. There are two noteworthy features in the absorption bands shown in Figure 2.6(a). Firstly, the bands are highly asymmetric, with sharp low-energy cut-offs and long absorption tails

on the high-energy side. Secondly, the bands show a non-periodic trend in absorption energies with the platinum derivative at the highest energy and the palladium derivative at the lowest energy.

Oxidation of the neutral $M(isq^\bullet)_2$ complexes to the mixed-valence $[M(isq^\bullet)(ibq)]^{1+}$ cations shifts the lowest-energy electronic absorption bands even further into the near-IR portion of the spectrum. As shown in Figure 2.6(c) and tabulated in Table 2.3, the lowest-energy absorption band for the mixed-valence cations, appear in the 5,000-6,400 cm^{-1} region. The low-energy absorptions of Figure 2.6(c) are more symmetric than the corresponding absorptions in the anion spectra (Figure 2.6(a)), only showing a small degree of truncation in the low-energy tail of the band. As with the mixed-valence anions, the low-energy absorption bands for the mixed-valence cations show a non-Periodic trend in energy, trending platinum > nickel > palladium.
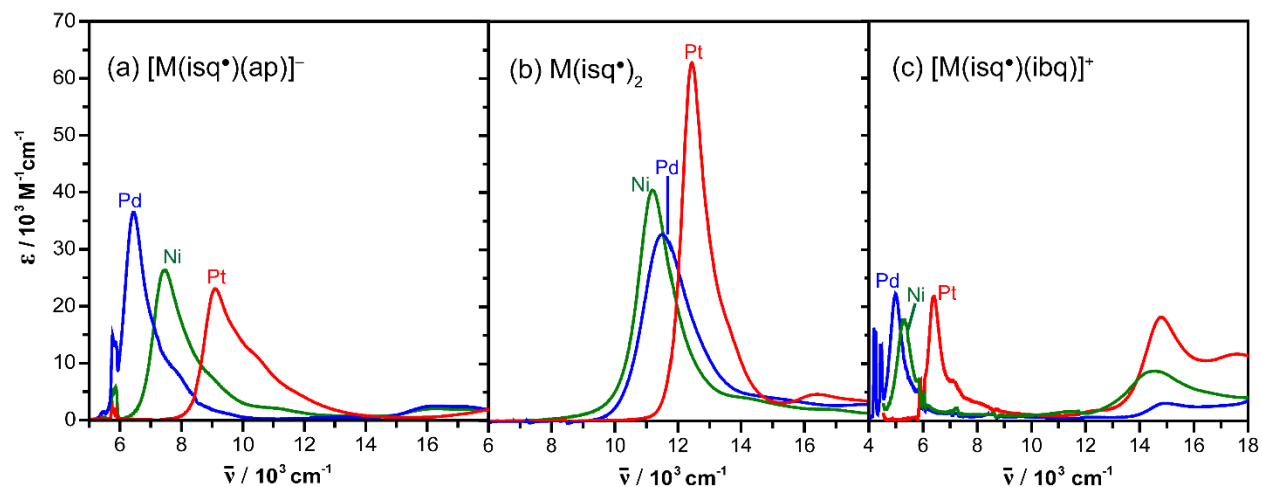
Figure 2.6. UV-vis-NIR absorption spectra for (a) $[Cp*_2Co][M(ap)(isq^\bullet)]$ in THF, (b) $M(isq^\bullet)_2$ in THF, and (c) $[M(isq^\bullet)(ibq)][PF_6]$ in CH_2Cl_2; (M = Ni, Pd, Pt).

Table 2.3. Intervalence charge-transfer (IVCT) absorption band data for $M(isq^{\bullet})_2$, $[M(ap)(isq^{\bullet})]^{1-}$, and $[M(isq^{\bullet})(iq)]^{1+}$ (M = Ni, Pd, Pt).

	$\bar{v}_{max}$ / cm^{-1}	ε_{max} / M^{-1} cm^{-1}
Ni(isq$^{\bullet}$)$_2$ [a]	11,210	40,700
Pd(isq$^{\bullet}$)$_2$ [a]	11,507	32,800
Pt(isq$^{\bullet}$)$_2$ [a]	12,437	62,800
[Ni(ap)(isq$^{\bullet}$)]$^{1-}$ [a]	7,457	25,200
[Pd(ap)(isq$^{\bullet}$)]$^{1-}$ [a]	6,443	36,400
[Pt(ap)(isq$^{\bullet}$)]$^{1-}$ [a]	9,107	23,000
[Ni(isq$^{\bullet}$)(iq)]$^{1+}$ [b]	5,310	17,900
[Pd(isq$^{\bullet}$)(iq)]$^{1+}$ [b]	4,995	22,200
[Pt(isq$^{\bullet}$)(iq)]$^{1+}$ [b]	6,393	21,800

[a]THF [b]CH$_2$Cl$_2$

2.2.6. X-Band EPR Spectroscopy

To further probe the degree of delocalization in the mixed-valence anions and cations, X-band solution EPR spectra were acquired at 77 K. Solutions of the mixed-valence anions, $[M(ap)(isq^{\bullet})]^{1-}$, were prepared by the treatment of the corresponding $M(isq^{\bullet})_2$ complex with one equivalent of Cp*$_2$Co in THF. Solutions of the mixed-valence cations, $[M(isq^{\bullet})(iq)]^{1+}$ were prepared by the treatment of the corresponding $M(isq^{\bullet})_2$ complex with one equivalent of AgPF$_6$ in CH$_2$Cl$_2$ followed by filtration to remove silver metal. Figure 2.7 shows the EPR spectra for each mixed-valence ion, while Table 2.4 presents *g*-tensors and hyperfine coupling constants used to simulate each spectrum using EasySpin with the *pepper* function.[59] As expected for one-electron oxidized and reduced species, all six spectra are consistent with $S = \frac{1}{2}$ complexes. For the anions, all three metal derivatives gave rhombic spectra with three distinct *g* values. In the nickel derivative, hyperfine coupling constants for two different nitrogen atoms were resolved in all three

dimensions. For the heavier palladium and platinum derivatives, significant coupling of the unpaired electron to the metal centers was observed.

The EPR spectra for the mixed-valence cations are strikingly different than the spectra of the anions. For $[Pd(isq^\bullet)(ibq)]^{1+}$, a single broad isotropic signal was observed at $g = 2.00$ with no resolved hyperfine coupling interactions. The spectrum of the nickel derivative, $[Ni(isq^\bullet)(ibq)]^{1+}$, gave an axial signal with g = 1.99 and 2.00 and coupling to one ^{14}N atom. The least symmetric cation spectrum was for the platinum derivative, $[Pt(isq^\bullet)(ibq)]^{1+}$, which was rhombic and showed coupling to both the platinum and to a single ^{14}N atom; however even in this case, the degree of rhombic distortion is significantly smaller than what was observed in the spectra for any of the mixed-valence anions.
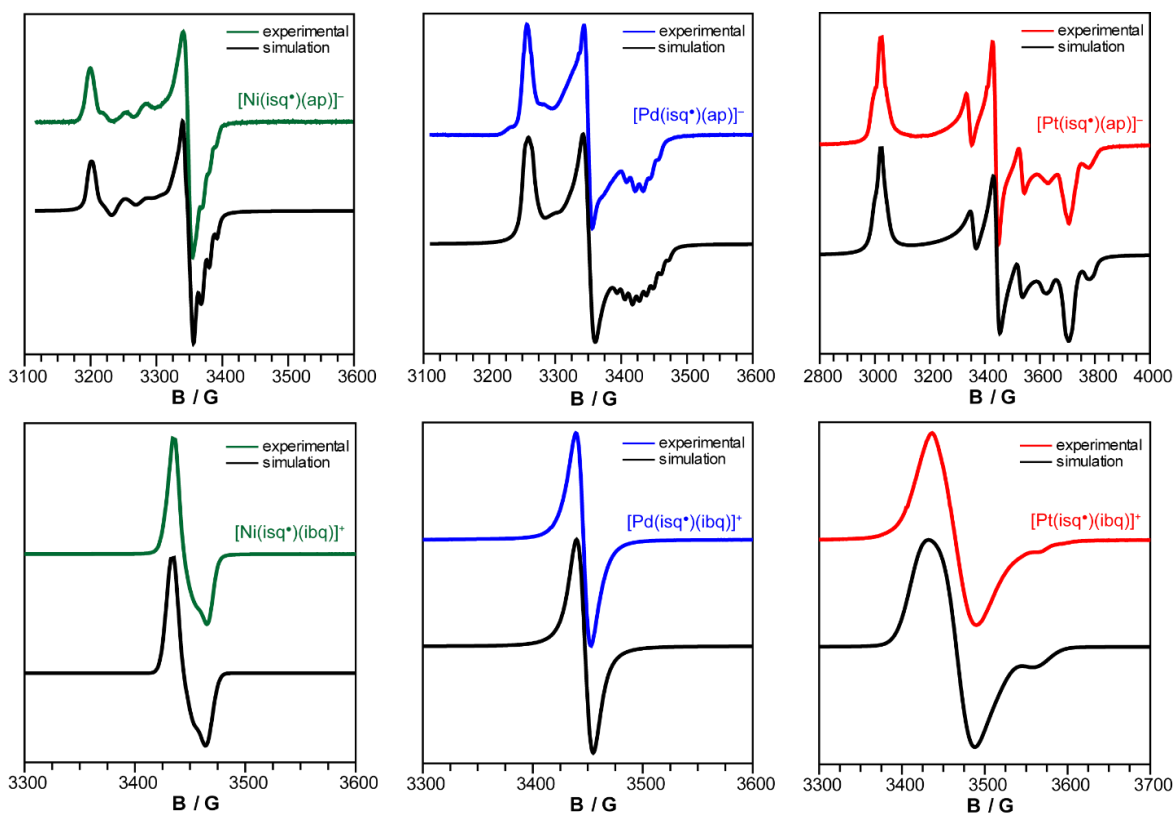
Figure 2.7. X-band EPR spectra of mixed-valence anions, $[M(ap)(isq^\bullet)]^{1-}$, and cations, $[M(isq^\bullet)(iq)]^{1+}$, of nickel (*left*), palladium (*center*), and platinum (*right*). All spectra were recorded at 77 K in THF (anions) or CH_2Cl_2 (cations). Simulated using EasySpin with pepper function and values shown in Table 2.4.

Table 2.4. g-Tensors and hyperfine coupling constants for mixed-valence [Cp*$_2$Co][M(ap)(isq$^\bullet$)] and [M(isq$^\bullet$)(ibq)] [PF$_6$] complexes (M = Ni, Pd, Pt).

	g_1	g_2	g_3	a_1 / MHz (nuclei)	a_2 / MHz (nuclei)	a_3 / MHz (nuclei)
[Ni(ap)(isq$^\bullet$)]$^{1-}$	2.00	2.01	2.11	36 (^{14}N) 29 (^{14}N)	7 (^{14}N) 5 (^{14}N)	6 (^{14}N) 12 (^{14}N)
[Pd(ap)(isq$^\bullet$)]$^{1-}$	1.97	2.01	2.07	29 (^{105}Pd) 35 (^{14}N)	6 (^{105}Pd) 9 (^{14}N)	17 (^{14}N)
[Pt(ap)(isq$^\bullet$)]$^{1-}$	1.86	2.00	2.28	411 (^{195}Pt) 34 (^{14}N)	479 (^{195}Pt)	139 (^{195}Pt) 12 (^{14}N)
[Ni(isq$^\bullet$)(iq)]$^{1+}$	1.99	2.00	--	31 (^{14}N)	10 (^{14}N)	--
[Pd(isq$^\bullet$)(iq)]$^{1+}$	2.00	--	--	--	--	--
[Pt(isq$^\bullet$)(iq)]$^{1+}$	1.96	1.98	2.00	159 (^{195}Pt) 81 (^{14}N)	7 (^{195}Pt) 3 (^{14}N)	-- 57(^{14}N)

2.3. Discussion

A series of bis-semiquinone group 10 metal complexes were investigated in an effort to understand how the bridging metal ion mediates the degree of coupling between two redox-active ligands, and consequently the electronic properties of the complexes. The neutral M(isq$^\bullet$)$_2$ complexes of nickel and palladium were readily synthesized by reacting the metal(0) synthons, either Ni(cod)$_2$ or Pd$_2$(dba)$_3$, with two equivalents of 3,5-di-tert-butyl(2,6-diisopropylphenyl)-orthoiminoquinone. In this reaction, the metal(0) center is presumably oxidized to the +2 state by donating one electron to each ligand which coordinate in the iminosemiquinone (isq$^\bullet$)$^{1-}$ form. This approach was taken instead of the salt approach established in the literature because the ligand was readily synthesized in the iminoquinone form versus the aminophenol form. Furthermore, the reactions could be carried out at ambient temperature and resulted in higher yields.

Structural data for the mixed-valence anions, [M(isq$^\bullet$)(ap)]$^-$, demonstrated that they are symmetric anions with a decamethylcobaltacenium counter cation. The C–N bond distances increased slightly from those in the neutral complexes and border between that expected for an

iminosemiquinone (isq$^{\bullet 1-}$) and an amidophenolate (ap^{2-}) ligand. The C–O bonds also had a small increase but were still within the range expected for a semiquinone. MOS calculations using the pertinent bond distances resulted in MOS values of –1.55, –1.60, and –1.56, for Ni, Pd, and Pt respectively. A MOS value of –1.50 would be the average charge expected for a (1–) and (2–) ligand that are strongly coupled and share a delocalized electron. The structural data suggest the formal oxidation state assignment of metal (II) ion, with one monoanionic iminosemiquinonate ligand and one dianionic amidophenolate ligand for each complex. The fact that the two ligands are crystallographically equivalent and have MOSs around –1.50 suggest that the system is strongly delocalized and potentially in the Class III regime.

In the case of the cationic mixed-valent complexes, [Ni(isq$^{\bullet}$)(ibq)]$^{1+}$ is symmetric but [Pd(isq$^{\bullet}$)(ibq)]$^{1+}$ is not. The nickel complex contained an inversion center resulting in crystallographically equivalent ligands as seen with the anionic complexes. The nickel derivative has an MOS value of –0.64, which is close to the expected value of –0.50 for a fully delocalized electronic structure in the monocation. This data suggest that the cationic nickel complex has a significant amount coupling in the solid state. In contrast, the structure of the [Pd(isq$^{\bullet}$)(ibq)]$^{1+}$ cation did not have an inversion center, and two different sets of ligand metrics were resolved. The pertinent bond distances resulted in MOS values of –0.78 and –0.29, corresponding to isq$^{\bullet -}$ and ibq^{0} ligands, respectively, suggesting that the ligand-ligand coupling in this complex has decreased to localize the unpaired electron on one ligand.

The electrochemical data provides further insight into the electronic character of the anionic mixed-valence systems. The potential of the first reduction (E$^{\circ}$'$_3$, Table 2.2) is approximately –1.20 V for all three compounds, indicating that this is a ligand-based event on which the metal identity has little to no influence. This reduction event is of interest because it

represents the formation of the mixed-valence species $[M(isq^\bullet)(ap)]^{1-}$. Comparatively, the second reduction $(E^{\circ\prime}_4)$ becomes increasingly negative: Pd (–2.11 V) < Ni (–2.27 V) < Pt (–2.33 V). The splitting (ΔE_{red}) between the two single electron reduction waves can be determined and its magnitude reflects the degree of coupling that exists between the two redox-active sites.[35,45] In the absence of any coupling, the two redox events would be expected to occur at approximately the same potential. Thus, as electronic coupling increases, ΔE_{red} should increase accordingly. The values ΔE_{red} follow the non-periodic trend: Pt > Ni > Pd, showing that ligand-ligand coupling is strongest in the Pt complex and weakest in the Pd complex (Table 2.2). As seen in Equation 2.1, the value of ΔE_{red} can be used to determine the comproportionation constant (K_c) for the singly reduced mixed-valent species.

$$K_c = exp\left(\frac{\Delta E_{red}F}{RT}\right) \tag{2.1}$$

$$L^n - L^n + L^{n+1} - L^{n+1} \leftrightharpoons 2L^n - L^{n+1} \tag{2.2}$$
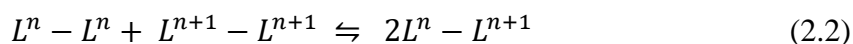
The K_c value is the equilibrium constant for the comproportionation reaction shown in equation 2.2. The value of K_c reflects the degree of stabilization imparted on the anionic mixed-valence species as a result of electron delocalization relative to the neutral, $M(isq^\bullet)_2$, and the dianionic $[M(ap)_2]^{2-}$ species and can be related to the electronic coupling parameter H_{ab}.[46–48] The K_c value can range from 4 for a localized system to 10^{24} for a fully delocalized system. Values greater than 10^{15} are typically observed in strongly delocalized systems.[49] The anionic mixed-valence species all have $K_{c(red)}$ values $\geq 10^{15}$.

In contrast, both oxidation events, also ligand based, show an increase in the redox potential moving down the group. The ΔE_{ox} values obtained for single electron oxidation waves follow the periodic trend: Pt > Pd > Ni, showing that the Pt complex experiences the greatest coupling between the two ligand and Ni the least. Additionally, the ΔE_{ox} values are 560–800 mV smaller

than the ΔE_{red} values, suggesting that a smaller degree of coupling exists for the singly oxidized [M(isq$^{\bullet}$)(ibq)]$^{1+}$ species versus the singly reduced [M(isq$^{\bullet}$)(ap)]$^{1-}$ species. Complexes **1–3** have $K_{c(ox)}$ values up to 10^6, (Table 2.2). These values are an order of magnitude smaller than $K_{c(red)}$, suggesting that the cationic species is not as stable as the anionic species. Arguably, it is the decrease in delocalization that permits the potential for ligand oxidation to be influenced by the metal identity.

Further support for the difference between the anionic and cationic mixed-valence complexes came from the analysis of the radical via EPR spectroscopy. The anionic complexes [M(isq$^{\bullet}$)(ap)]$^{1-}$ were characterized by complex rhombic EPR spectra with hyperfine coupling to ^{14}N nuclei along with ^{105}Pd and ^{195}Pt nuclei in the case of M = Pd and M = Pt , respectively. Each spectrum had three distinct g values with $g_{ave} = 2$, consistent with a ligand-based radical. For the cations, [M(isq$^{\bullet}$)(ibq)]$^{1+}$, the EPR spectra were characterized by axial to isotropic signals with little to no hyperfine interactions. The decrease in complexity and hyperfine coupling in the cationic mixed-valence system substantiates all the previous results indicating that the radical in more strongly delocalized in the anionic systems [M(isq$^{\bullet}$)(ap)]$^{1-}$.

Coordination of two semiquinonate ligands to a metal(II) center generates symmetric square planar complexes with low-energy charge-transfer absorptions in the electronic spectrum. Based on the spectroscopic data obtained for the M(isq$^{\bullet}$)$_2$ series, the low-energy absorption bands have been assigned as LL'CT transitions, corresponding to the transfer of an electron from one semiquinonate ligand to the other. As expected, the LL'CT bands show no solvent dependence due to the non-polar ground state of the symmetric complexes. The energy of the transitions corresponds with the electrochemically determined HOMO-LUMO gaps ($E^{\circ\prime}_3$–$E^{\circ\prime}_2$). The platinum complex has the highest energy, followed palladium, and nickel. The neutral M(isq$^{\bullet}$)$_2$ complexes

were titrated with decamethylcobaltocene to evaluate the electromagnetic spectrum of the anionic $[M(isq^{\bullet})(ap)]^{1-}$ mixed-valence species. Stoichiometric additions of the reductant led to the slow disappearance of the LL'CT band around 12,000 cm^{-1} and growth of an IVCT band at lower energy (<10,000 cm^{-1}). The energy of the transition and band width decreased from Pt > Ni > Pd. Studies of mixed-valence systems have demonstrated that the IVCT bands of fully delocalized Class III systems are typically intense with $\varepsilon_{max} \geq 5000$ M^{-1}cm^{-1}, are solvent independent, exhibit narrow bandwidths ($\Delta v_{1/2} \leq 2000$ cm^{-1}), and are asymmetric with a low-energy cut-off. The IVCT bands of all the anionic $[M(isq^{\bullet})(ap)]^{1-}$ mixed-valence complexes had ε_{max} values above 20,000 M^{-1} cm^{-1}, band widths below 2,000 cm^{-1}, and showed no sensitivity to solvent when compared in CH_2Cl_2, toluene, acetonitrile, and THF; supporting their assignment as Class III systems. Stoichiometric additions tris(p-tolyl)aminium tetrafluoroborate led to the slow disappearance the LL'CT band around 12,000 cm^{-1} and growth of an IVCT band below 8,000 cm^{-1} for all three metal congeners of the cationic $[M(isq^{\bullet})(ibq)]^{1+}$ mixed-valence species. The IVCT bands appeared at lower energies than the anionic complexes but followed the same metal trend with platinum with the highest energy, nickel, then palladium at the lowest energy. The ε_{max} of the $[M(isq^{\bullet})(ibq)]^{1+}$ complexes all decreased, ranging from 17,000–22,000 M^{-1} cm^{-1}, in comparison to the anionic complexes which had a low end of 22,000 M^{-1} cm^{-1}.

The experimental evidence discussed above was used to classify the anionic complexes (**1a–3a**) as Class III systems within the Robin-Day classification scheme. The electronic coupling parameter, H_{ab}, was determined using equation 2.3, where v_{max} is the energy of the IVCT transition, for the anionic complexes (**1a–3a**).[39,40]

$$H_{ab} = \frac{v_{max}}{2} \qquad (2.3)$$

Equation 2.3 can be used to determine the electronic coupling, H_{ab}, of a symmetrical Class III system directly from the energy of the optical transition. Characterization of the cationic complexes (**1b–3b**) suggested weaker coupling and made their assignment within the Robin-Day classification more ambiguous. As a result, equation 2.4 which can be applied to mixed-valence systems spanning Robin-Day Class II to Class III, was used to analyze the cations.

$$H_{ab} = \frac{|\mu|}{er_{ab}} \nu_{max} \qquad (2.4)$$

In equation 2.4, μ is the transition dipole moment (C cm), e is the elementary charge of an electron, ν_{max} is the energy of the IVCT band in cm^{-1}, and r_{ab} is the electron transfer distance (cm). The transition dipole moment was calculated from the numerical integration of the IVCT band using equations 2.5 and 2.6 below.

$$f = 4.319 \ x \ 10^{-9} \int_{band} dv \ \varepsilon(v) \qquad (2.5)$$

$$f = \frac{8\pi M_e \bar{v}}{3he^2} \mu^2 \qquad (2.6)$$

In equation 2.5 the integration of the IVCT band is used to determine the oscillator strength, f. The oscillator strength is used in equation 2.6 to solve for the transition dipole, μ. In equation 2.5, M_e is the mass of an electron in kilograms, $\bar{v}$ is the energy of the transition in Hertz, h is the Planck constant, and e is the charge of an electron in Coulombs. In traditional metal-based mixed-valence systems, the electron transfer distance is measured from metal center to metal center. This value is typically obtained from solid-state structural data and has a small degree of error associated with it. However, in ligand-based mixed-valency the electron transfer distance is difficult to define explicitly. On the grounds that the exact electron transfer distance is not known, the r_{ab} values were calculated for the Class III anions by setting Equations 2.3 and 2.4 equal to one another and

solving for r_{ab}. This r_{ab} value was then used to determine H_{ab} for the cations using equation 2.4. This is done under the assumption that the molecular structure, and therefore electron transfer distance, does not change significantly between the anions and cations. This assumption is supported by the structural data obtained. The results of the r_{ab}, μ, and H_{ab} calculations are compiled in Table 2.5. The H_{ab} values for the anions $[M(isq^\bullet)(ap)]^{1-}$ (**1a–3a**) were as follows: (Pt) $= 4600$ cm^{-1} > (Ni) $= 3200$ cm^{-1} > (Pd) $= 4600$ cm^{-1}. These results suggest that the platinum bridge promotes the greatest amount of coupling between the two redox-active ligands while the palladium bridge results in the least amount of coupling. This observation is in agreement with previous reports that investigate the same metal series with redox-active ligands.[50–52] The H_{ab} values for the cationic species $[M(isq^\bullet)(ibq)]^{1+}$ (**1b–3b**), followed the same non-periodic trend: (Pt) $= 2200$ cm^{-1} > (Ni) $= 1800$ cm^{-1} > (Pd) $= 1700$ cm^{-1}. Even though the trend in H_{ab} values (Pt > Ni > Pd) agrees with that observed in the anionic species, the magnitudes of H_{ab} decreased significantly for the cations. This further supports the finding that coupling is decreased in the cationic mixed-valence species versus the anionic mixed-valence species. The metal trend observed in both systems is consistent with other reports and best explained by the energy ordering of the metal orbitals. A better energetic match between the metal (bridge) orbitals and ligand (redox site) orbitals results in stronger electronic coupling. The orbital energy is expected to follow the trend: Ni (3d) < Pd (4d) < Pt (5d). However, the orbital energy is influenced by effective nuclear charge (Z_{eff}) and relativistic effects and leads to Pd (4d) < Ni (3d) < Pt (5d). A higher orbital energy for platinum and nickel is consistent with the energy of the IVCT transitions observed. In both the anionic and cationic systems, the platinum complex had the largest IVCT energy and the palladium congener had the smallest.

Table 2.5. H_{ab} Values and Electronic Absorption Parameters for the IVCT bands of the Mixed Valence Complexes $[M(isq^{\bullet})(ap)]^{1-}$ and $[M(isq^{\bullet})(ibq)]^{1+}$.

	$\bar{v}_{max}$ / cm^{-1}	ε_{max} / M^{-1} cm^{-1}	H_{ab} / cm^{-1}	$r_{ab}{}^{c}$ / cm	μ / C cm
$[\text{Ni(ap)(isq}^{\bullet})]^{1-\,a}$	7460	25,200	3700^{d}	5.54 x 10^{-8}	4.4 x 10^{-27}
$[\text{Pd(ap)(isq}^{\bullet})]^{1-\,a}$	6440	36,400	3200^{d}	6.05 x 10^{-8}	4.8 x 10^{-27}
$[\text{Pt(ap)(isq}^{\bullet})]^{1-\,a}$	9110	23,000	4600^{d}	5.03 x 10^{-8}	4.0 x 10^{-27}
$[\text{Ni(isq}^{\bullet})(\text{ibq})]^{1+\,b}$	5310	17,900	1800^{e}	5.54 x 10^{-8}	3.0 x 10^{-27}
$[\text{Pd(isq}^{\bullet})(\text{ibq})]^{1+\,b}$	5000	22,200	1700^{e}	6.05 x 10^{-8}	3.2 x 10^{-27}
$[\text{Pt(isq}^{\bullet})(\text{ibq})]^{1+\,b}$	6390	21,800	2200^{e}	5.03 x 10^{-8}	2.8 x 10^{-27}

^{a}THF ^{b}CH$_2$Cl$_2$; ^{c}calculated; ^{d} $H_{ab} = v_{max}/2$; ^{e} $H_{ab} = \mu_{12}(v_{max})/er_{ab}$

Density functional theory (DFT) computations were used to model the electronic structures of the neutral M(isq$^{\bullet}$)$_2$ complexes (M = Ni, Pd, Pt). The single-crystal structures were used as the starting point for geometry optimizations, and the calculations were carried out using the B3LYP functional set at the TZVP level of theory. All complexes refined with broken symmetry, singlet occupation for the ground-state species. The computational analysis of the molecular orbitals shows that the donor (HOMO) and acceptor (LUMO) orbitals are largely ligand localized with an alpha (α) and beta (β) component for each and only 6–8% metal character for Ni and Pd (Figure 2.8). Upon excitation, a charge transfer occurs from an α/β-HOMO orbital to an α/β-LUMO orbital, corresponding to a ligand-to-ligand charge transfer transition depicted in Figure 2.8 as λ_{max}. In the case of platinum, the HOMO and LUMO are equally developed on both ligands, and the LUMO contains 17% metal character. This result supports the notion that the platinum orbitals are higher in energy which allows for greater orbital mixing between the metal and ligands, and results in a transition that is higher in energy and has a $\varepsilon_{max} > 60,000$ M^{-1} cm^{-1} (double that observed for palladium).
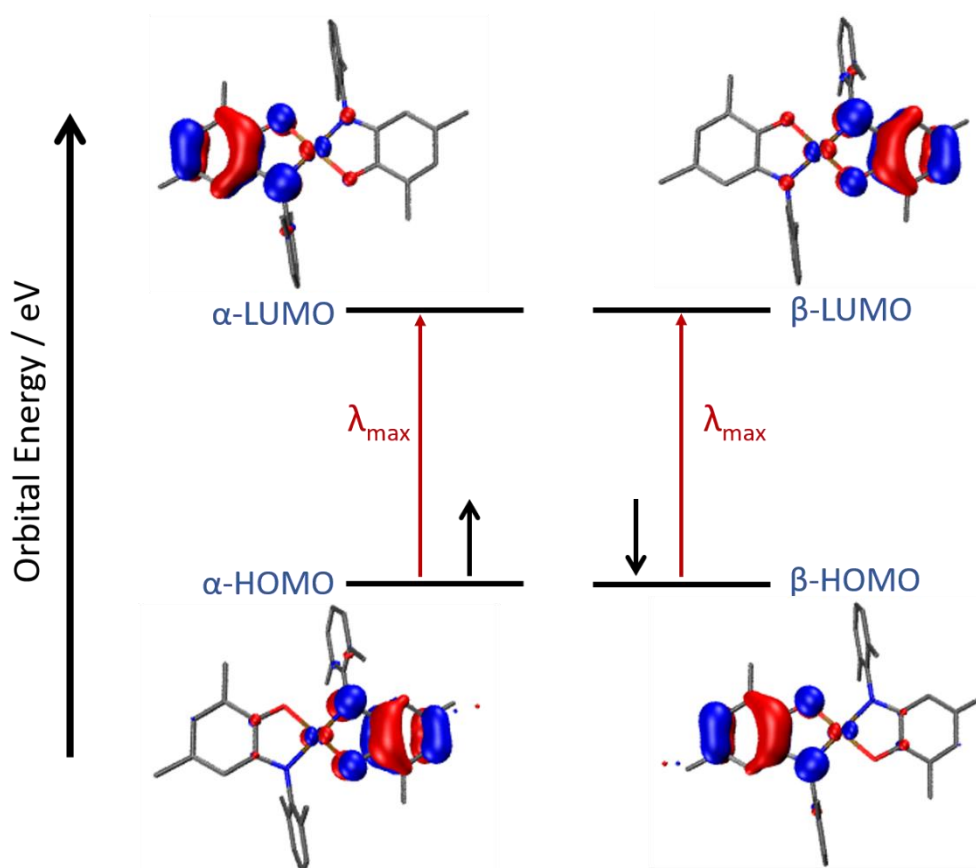
Figure 2.8. Frontier molecular orbital picture of Ni(isq$^\bullet$)$_2$ as determined by DFT computations using a singlet, broken symmetry ground-state.

Figure 2.9 shows the electronic structure of the neutral complexes (**1–3**) calculated using a closed-shell S = 0 ground state. This orbital diagram provides an explanation for the differences observed between the anions (**1a–3a**) and the cations (**1b–3b**). The HOMO orbital which is the SOMO of the monocations has minimal metal contributions (< 5%). The node at the metal bridge reduces ligand-ligand coupling and decreases radical delocalization. The LUMO orbitals, or SOMOs of the anions, have 13–19% metal character due to the interaction of the d_{xz} metal orbital. The increased bridge interaction allows the radical to become strongly delocalized. Similar computational studies have been reported for the mixed-valent species of related complexes of group 10 metals. Specifically, Thomas and coworkers reported mixed-valence complexes using the pincer ligand, bis(2-amino-3,5-di-tert-butylphenyl)amine in 2018.
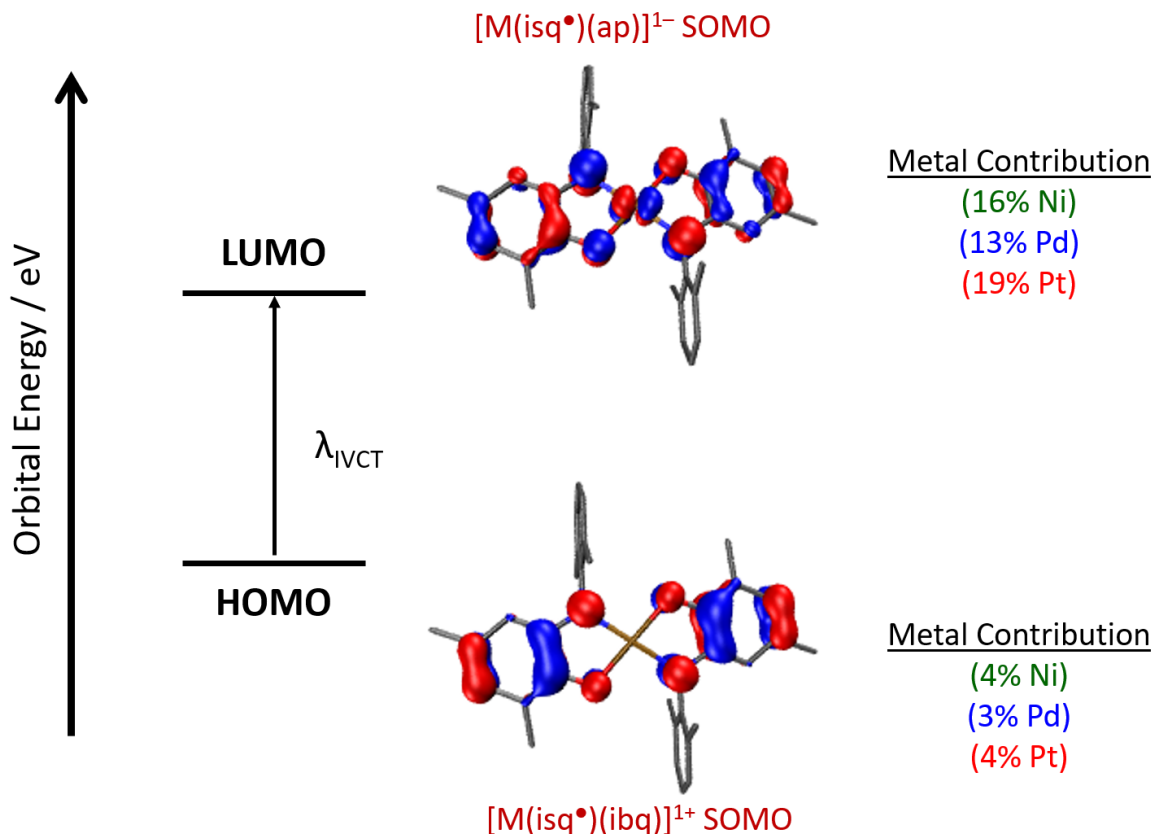
Figure 2.9. Frontier molecular orbital picture of Ni(isq•)$_2$ as determined by DFT computations using a S = 0, closed-shell ground-state. FMO diagram is representative of Ni, Pd, and Pt congeners.

Computational analyses of their one-electron oxidized species resulted in symmetric structures that contained a SOMO with equally developed ligand halves and a NIR transition from α-HOMO → α-LUMO consistent with an intervalence charge-transfer (IVCT). The HOMO orbital was b$_2$ symmetric and did not interact with the metal d orbitals. The LUMO, however, had a$_2$ symmetry and could mix with the metal d orbital, resulting in a more significant metal contribution to the LUMO.[31] Ultimately, these recent reports and the work described herein are in agreement with the electronic structure outlined by Wieghardt and coworkers based on the two redox-active molecular orbitals of bis(o-diiminobenzosemiquinonate) and bis(o-iminobenzosemiquinonate) complexes.[30] His electronic structure summary for a [Pd(^{1}L)$_2$]^n transfer series is shown in Figure 2.10. When

applied to the mixed-valence complexes of this work, shows that the degree of delocalization for the mixed-valent cation can be modulated by metal choice.
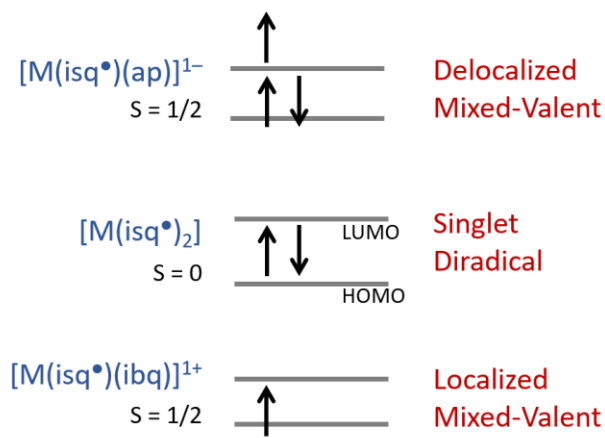
Figure 2.10. Summary of Electronic Structure of M(isq$^\bullet$)$_2$ and the one-electron reduced and one-electron oxidized congeners as outlined by Wieghardt et. al. Figure adapted from reference 30.

2.4. Conclusions

The mixed-valent anionic [M(isq$^\bullet$)(ap)]$^{1-}$ and cationic [M(isq$^\bullet$)(ibq)]$^{1+}$ complexes reported herein were prepared and characterized to confirm the redox loci and subsequently evaluate the influence of the metal ion on the electronic delocalization of the mixed-valence complexes. These systems provide an avenue to apply current methods to study and understand ligand-based mixed-valency. Electrochemical data was used to determine the comproportionation constant (K_c), which reflects the stability of the singly reduced/oxidized mixed-valent complex. The K_c values obtained suggests the systems are largely delocalized. The K_c values of the [M(isq$^\bullet$)(ibq)]$^{1+}$ species were an order of magnitude smaller implying that the coupling between the two redox sites is weaker in monocations. Analysis of the IVCT bands of the [M(isq$^\bullet$)(ap)]$^{1-}$ complexes demonstrated a subtle change in the amount of coupling based on the identity of the metal center. The degree of coupling, measured by the electronic coupling parameter, H$_{ab}$, increases in the order Pd < Ni < Pt. Concurrent, analysis of the [M(isq$^\bullet$)(ibq)]$^{1+}$ series resulted in

53

the same trend for the degree of coupling, however, the H_{ab} values, were smaller than those calculated for the anionic species. The difference between the anions and cations was corroborated by analysis of the radical species via EPR. The anionic complexes were characterized by complex rhombic spectra with significant hyperfine interactions; meanwhile, the cationic complexes had isotropic signals with little to no hyperfine, indicative of a more localized radical.

The differences observed between the anionic and cationic complexes are a result of the electronic structure. The ligand-based SOMO in $[M(isq^\bullet)(ap)]^{1-}$ interacts with the metal bridge orbital which increases the metal contribution and increases delocalization. In the $[M(isq^\bullet)(ibq)]^{1+}$ complexes, the SOMO has minor metal contributions which decreases electronic delocalization. The degree of delocalization increased based on metal identity as follows: Pt > Ni > Pd. The properties of the mixed-valent species investigated demonstrate that both the metal ion identity and the charge on the complex have a measurable influence on the delocalization of the unpaired electron.

2.5. Experimental

General Procedures. All compounds and reactions reported below show various levels of air and moisture sensitivity, so all manipulations were carried out using standard vacuum-line, Schlenk-line, and glovebox techniques. Solvents were sparged with argon before being deoxygenated and dried by passage through Q5 and activated alumina columns. $Ni(cod)_2$ and $PtCl_2$ were purchased from commercial sources and used as received. The iminoquinone, 3,5-di-*tert*-butyl-2-(2,6-diisopropylphenylimino)quinone,[42] and tris(dibenzylideneacetone)diplatinum(0)[53,54] were prepared according to literature procedures.

Physical Methods. Solution NMR spectra were collected using Bruker DRX400 or Bruker Avance 500 spectrometers at 298 K in either $CDCl_3$ or C_6D_6. Chemical shifts are reported in parts

per million relative to TMS using the residual proteo impurities of the solvent for ^{1}H NMR spectra signal of the solvent. Solution electronic absorption spectra were recorded using a Jasco V-670 UV-vis-NIR spectrometer using 1 cm path-length cells at ambient temperature (20-24 °C).

Electrochemical Methods. Electrochemical experiments were performed on a Gamry Series G300 potentiostat/galvanostat/ZRA (Gamry Instruments, Warminster, PA) using a 3.0 mm glassy carbon working electrode, a platinum wire auxiliary electrode, and a silver wire pseudo-reference electrode at ambient temperature (20−24 °C) in a nitrogen-filled glovebox. THF solutions for electrochemical experiments typically contained 1.0 mM analyte and 100 mM [Bu$_4$N][PF$_6$] as the supporting electrolyte. All potentials are referenced to [Cp$_2$Fe]$^{+/0}$ using ferrocene as an internal standard added at the end of a sample run. Ferrocene was purified by sublimation under reduced pressure, and tetrabutylammonium hexafluorophosphate (Acros) was recrystallized from ethanol three times and dried under a vacuum.[55]

Redox Titrations. The generation of the mixed-valence anions, [M(isq$^\bullet$)(ap)]$^{1-}$, and cations, [M(isq$^\bullet$)(ibq)]$^{1+}$, from the neutral M(isq$^\bullet$)$_2$ (M = Ni, Pd, Pt) was investigated by spectrophotometric titration. In a typical experiment, a THF stock solutions of M(isq$^\bullet$)$_2$ (15–20 μM) and [Cp*$_2$Co] (3 mM) were prepared inside a nitrogen-filled glovebox. or tris(p-tolyl)aminium tetrafluoroborate Aliquots (5 mL) of the metal complex were removed from the stock solution, the appropriate equivalents of reductant (from base stock solution) were added using a volumetric syringe. The sample solution was transferred to a quartz cuvette and sealed to maintain an air-free environment. Spectral changes for each sample (equivalent of reductant added) were recorded with a Jasco 670 UV–vis spectrometer. Due to solubility restrictions, the oxidation titrations were carried out in CH$_2$Cl$_2$. Stock solutions of M(isq$^\bullet$)$_2$ (15–20 μM) and tris(p-tolyl)aminium tetrafluoroborate (2 mM) were prepared and used as described above.

Crystallographic Methods. X-ray diffraction data were collected at low temperature on a single crystal covered in Paratone and mounted on a glass fiber. Data were acquired using a Bruker SMART APEX II diffractometer equipped with a CCD detector using Mo Kα radiation (λ = 0.71073 Å), which was wavelength-selected with a single-crystal graphite monochromator. The *SMART* program package was used for determination of the unit-cell parameters and for data collection. The raw frame data were processed using *SAINT* and *SADABS* to yield the reflection data file. Subsequent calculations were carried out with *SHELXTL*. The structures were solved by direct methods and refined on F^2 by full-matrix least-squares techniques. Analytical scattering factors for neutral atoms were used throughout the analyses. Hydrogen atoms were generated in calculated positions and refined using a riding model. ORTEP diagrams were generated using *ORTEP-3 for Windows*.

Computational Methods. All calculations were performed employing the non-empirical B3LYP density functional theory using the quantum chemistry program package TURBOMOLE 7.2.[56] For computational efficiency, initial geometry optimizations were performed using moderate split-valence plus polarization basis sets (def2-SVP).[57] Structures were refined using basis sets of triple zeta valence plus polarization (def2-TZVP) quality.[58] Crystal structures obtained from X-ray diffraction experiments were used as starting points for the geometry optimization; no molecular symmetry was imposed. Energies and minimum energy structures were evaluated self-consistently to tight convergence criteria (energy converged to 0.1 μHartree, maximum norm of the Cartesian gradient $\leq 10^{-4}$ a.u.).

Synthesis of Ni(isq•)₂. 110 mg of Ni(cod)₂ (0.410 mmol, 1 equiv) was weighed out into a 20-mL glass vial and dissolved in approximately 5 mL of toluene. In a separate vial, 303 mg of 2,4-di-tert-butyl-6-((2,6-diisopropylphenyl)imino)benzoquinone (0.800 mmol, 2 equiv) were dissolved

56

in toluene. The ligand solution was added dropwise to the solution of nickel. The reaction mixture began to turn a dark deep-green color after 5 minutes. It was left stirring in the glovebox at room temperature overnight. The solvent volume was reduced under vacuum and then chilled to -35 °C overnight. The solution was filtered and the solid collected was washed with a small amount of toluene. The solid was brought out of the box and washed with methanol to remove any unreacted ligand. The final product was a deep-green powder in 86% yield. Anal. Calc for $C_{52}H_{74}N_2O_2Ni$: C, 76.37% ; H, 9.12%; N, 3.43%. Found: C, 76.25%; H, 9.59%; N, 3.26%. ^{1}H NMR (400 MHz, C_6D_6) δ 7.31 (t, J = 7.7 Hz, 3H), 7.19 (d, J = 7.7 Hz, 4H), 6.45 (d, J = 1.8 Hz, 2H), 3.61 (p, J = 6.9 Hz, 4H), 1.47 (d, J = 6.9 Hz, 12H), 1.15 (s, 18H), 1.08 – 1.05 (m, 12H), 0.99 (s, 18H). MS (ES+ TOF) m/z = 817.5 Ni(isq)$_2$, 840.5 Ni(isq)$_2$ + Na$^+$.

Synthesis of Pd(isq$^•$)$_2$. 230 mg of Pd(dba)$_2$ was weighed out into a 20-mL glass vial and dissolved in approximately 5 mL of toluene. In a separate vial, 303 mg of 2,4-di-tert-butyl-6-((2,6-diisopropylphenyl)imino)benzoquinone (0.800 mmol, 2 equiv) were dissolved in toluene. The ligand solution was added dropwise to the solution of palladium. The reaction mixture began to turn a dark deep-blue color after 30 minutes. It was left stirring in the glovebox at room temperature overnight. The solvent volume was reduced under vacuum and then chilled to -35 °C overnight. The solution was filtered and the solid collected was washed with a small amount of toluene. The solid was brought out of the box and washed with methanol to remove any unreacted ligand. The final product was a deep-blue powder in 70% yield. Anal. Calc for $C_{52}H_{74}N_2O_2Pd$: C, 72.15%; H, 8.62%; N, 3.24%. Found: C, 72.05%; H, 8.86%; N, 3.15%. ^{1}H NMR (400 MHz, C_6D_6) δ 7.36 (s, 1H), 7.29 (dd, J = 8.7, 6.5 Hz, 2H), 7.24 – 7.20 (m, 4H), 6.96 (s, 1H), 6.46 (s, 2H), 3.55 (p, J = 6.9 Hz, 4H), 1.51 (d, J = 6.8 Hz, 12H), 1.22 (s, 18H), 1.11 (d, J = 6.8 Hz, 12H), 1.08 (s, 18H). MS (ES+ TOF) m/z = 864.5 Pd(isq)$_2$, 887.5 Pd(isq)$_2$ + Na$^+$.

Synthesis of Pt(isq•)₂. 118 mg of Pt₂(dba)₃ (0.178 mmol, 1 equiv) was added into a 25-mL 3-neck round bottom flask with 10 mL of dichloromethane (DCM), sealed, and degassed for 5 minutes. In a 10-mL round bottom flask 135 mg of 2,4-di-tert-butyl-6-((2,6-diisopropylphenyl)imino)benzoquinone (0.356 mmol, 2 equiv) was dissolved in 5 mL of DCM and then sealed and degassed for 5 minutes. The ligand solution was transferred to the round bottom with the platinum using a syringe. The reaction was heated to reflux under N_2 for 2 hours. The dark blue reaction mixture was cooled to room temperature and then exposed to air. The solvent was removed using a rotary evaporator. The blue-green residue was dissolved in a small amount of DCM and run through a silica column. The fraction containing the product eluded last and was a dark blue-green color. The solvent was removed using a rotary evaporator and the dark blue powder was dried on the Shlenk-line overnight. ¹H NMR (400 MHz, CDCl₃) δ 7.41 (dd, J = 8.4, 7.0 Hz, 2H), 7.31 (d, J = 7.6 Hz, 4H), 6.91 (d, J = 2.1 Hz, 2H), 6.28 (d, J = 2.0 Hz, 2H), 3.04 (p, J = 6.8 Hz, 4H), 1.20 (d, J = 6.8 Hz, 12H), 1.13 (d, J = 9.0 Hz, 36H), 1.07 (d, J = 6.9 Hz, 12H). MS (ES+ TOF) m/z = 954.5 Pt(isq)₂ + H⁺, 976.5 Pt(isq)₂ + Na⁺.

Synthesis of [CoCp*₂][M(ap)(isq•)] (M = Ni, Pd, Pt). Decamethylcobaltacene (CoCp*₂) (1 equiv) in THF was added drop-wise to solutions of the neutral complexes (**1–3**) in THF and stirred at ambient temperature for 10 minutes. This generated the singly reduced monoanionic complexes of the form, [CoCp*₂][M(isq)(ap)]. The solution was concentrated down to 1–2 mL under reduced pressure and stored at -35 °C to afford x-ray quality crystals of **1a–3a**.

Synthesis of [M(isq•)(ibq)][PF₆] (M = Ni, Pd, Pt). Solid AgPF₆ (1 equiv) was added to solutions of the neutral complexes (**1–3**) in DCM and stirred at ambient temperature overnight. The reaction solution was filtered to remove Ag(0). This generated the singly oxidized monocationic complexes of the form, [M(isq)(ibq)][PF₆]. The solution was concentrated down to 1–2 mL under reduced

pressure and layered with pentane (**1b**) or toluene (**2b**) and stored at -35 °C to afford x-ray quality crystals of **1b** and **2b**.

2.6 References

(1)   Chirik, P. J. *Inorg. Chem.* **2011**, *50* (20), 9737–9740.

(2)   Kaim, W. *Inorg. Chem.* **2011**, *50* (20), 9752–9765.

(3)   Jørgensen, C. K. *Coord. Chem. Rev.* **1966**, *1* (1–2), 164–178.

(4)   Scarborough, C. C.; Wieghardt, K. *Inorg. Chem.* **2011**, *50* (20), 9773–9793.

(5)   Eisenberg, R.; Gray, H. B. *Inorg. Chem.* **2011**, *50*, 9741–9751.

(6)   Heyduk, A. F.; Zarkesh, R. A.; Nguyen, A. I. *Inorg. Chem.* **2011**, *50* (20), 9849–9863.

(7)   Kramer, W. W.; Cameron, L. A.; Zarkesh, R. A.; Ziller, J. W.; Heyduk, A. F. *Inorg. Chem.* **2014**, *53* (16), 8825–8837.

(8)   Cameron, L. A.; Ziller, J. W.; Heyduk, A. F. *Chem. Sci.* **2016**, *7* (3), 1807–1814.

(9)   Xie, L. S.; Sun, L.; Wan, R.; Park, S. S.; Degayner, J. A.; Hendon, C. H.; Dincă, M. *J. Am. Chem. Soc.* **2018**, *140*, 7411–7414.

(10)   Downes, C. A.; Marinescu, S. C. *ACS Catal.* **2017**, *7* (12), 8605–8612.

(11)   Miner, E. M.; Gul, S.; Ricke, N. D.; Pastor, E.; Yano, J.; Yachandra, V. K.; Van Voorhis, T.; Dincă, M. *ACS Catal.* **2017**, *7* (11), 7726–7731.

(12)   Clough, A. J.; Skelton, J. M.; Downes, C. A.; de la Rosa, A. A.; Yoo, J. W.; Walsh, A.; Melot, B. C.; Marinescu, S. C. *J. Am. Chem. Soc.* **2017**, *139* (31), 10863–10867.

(13)   Zarkesh, R. A.; Ziller, J. W.; Heyduk, A. F. *Angew. Chemie Int. Ed.* **2008**, *47* (25), 4715–

4718.

(14)   Smith, A. L.; Hardcastle, K. I.; Soper, J. D. *J. Am. Chem. Soc.* **2010**, *132* (41), 14358–14360.

(15)   Rajabimoghadam, K.; Darwish, Y.; Bashir, U.; Pitman, D.; Eichelberger, S.; Siegler, M. A.; Swart, M.; Garcia-Bosch, I. *J. Am. Chem. Soc.* **2018**, *140* (48), 16625–16634.

(16)   Sun, X.; Chun, H.; Hildenbrand, K.; Bothe, E.; Weyhermu, T.; Neese, F.; Wieghardt, K. *Inorg. Chem.* **2002**, *41* (16), 4295–4303.

(17)   Chaudhuri, P.; Verani, C. N.; Bill, E.; Bothe, E.; Wieghardt, K. *J. Am. Chem. Soc.* **2001**, *123* (3), 2213–2223.

(18)   Abakumov, G. A.; Cherkasov, V. K.; Bubnov, M. P.; Zakharov, L. N.; Struchkov, Y. T.; N, S. Y. *Izv. Akad. Nauk* **1992**, No. 10, 2315–2323.

(19)   Fox, G. A.; Pierpont, C. G. *Inorg. Chem.* **1992**, *31*, 3718–3723.

(20)   Herebian, D.; Bothe, E.; Neese, F.; Weyhermüller, T.; Wieghardt, K. *J. Am. Chem. Soc.* **2003**, *125* (30), 9116–9128.

(21)   Herebian, D.; Bothe, E.; Bill, E.; Weyhermu, T.; Wieghardt, K. *J. Am. Chem. Soc.* **2001**, *123*, 10012–10023.

(22)   Girgis, A. Y.; Balch, A. L. *Inorg. Chem.* **1975**, *14* (11), 2724–2727.

(23)   Pierpont, C. G.; Buchanan, R. M. *Coord. Chem. Rev.* **1981**, *38*, 45–87.

(24)   Davison, A.; Edelstein, N.; Holm, R. H.; Maki, A. H. *J. Am. Chem. Soc.* **1963**, *85* (13), 2029–2030.

(25)   Hollas, A. M.; Ziller, J. W.; Heyduk, A. F. *Polyhedron* **2018**, *143*, 111–117.

(26)   Gray, H. B.; Billing, E. *J. Am. Chem. Soc.* **1963**, *85*, 2019–2020.

(27)   Schrauzer, G. N.; Mayweg, V. *J. Am. Chem. Soc.* **1962**, *84* (16), 3221–3221.

(28)   Gray, H. B.; Williams, R.; Bernal, I.; Billig, E. *J. Am. Chem. Soc.* **1962**, *84* (18), 3596–3597.

(29)   Bubnov, M. P.; Skorodumova, N. A.; Baranov, E. V; Bogomyakov, A. S.; Cherkasov, V. K.; Abakumov, G. A.; Razuvaev, G. A. *Inorganica Chim. Acta* **2013**, *406*, 153–159.

(30)   Kokatam, S.; Weyhermüller, T.; Bothe, E.; Chaudhuri, P.; Wieghardt, K. *Inorg. Chem.* **2005**, *44* (10), 3709–3717.

(31)   Leconte, N.; Moutet, J.; Constantin, T.; Molton, F.; Philouze, C.; Thomas, F. *Eur. J. Inorg. Chem.* **2018**, *2018* (16), 1752–1761.

(32)   Conner, K. M.; Perugini, A. L.; Malabute, M.; Brown, S. N. *Inorg. Chem.* **2018**, *57*, 3272–3286.

(33)   Conner, K. M.; Arostegui, A. C.; Swanson, D. D.; Brown, S. N. *Inorg. Chem.* **2018**, *57*, 9696–9707.

(34)   Demadis, K. D.; Hartshorn, C. M.; Meyer, T. J. *Chem. Rev.* **2001**, *101*, 2655–2685.

(35)   Ito, T.; Hamaguchi, T.; Nagino, H.; Yamaguchi, T.; Kido, H.; Zavarine, I. S.; Richmond, T.; Washington, J.; Kubiak, C. P. *J. Am. Chem. Soc.* **1999**, *121* (19), 4625–4632.

(36)   Canzi, G.; Goeltz, J. C.; Henderson, J. S.; Park, R. E.; Maruggi, C.; Kubiak, C. P. *J. Am. Chem. Soc.* **2014**, *136* (5), 1710–1713.

(37) Londergan, C. H.; Salsman, J. C.; Lear, B. J.; Kubiak, C. P. *Chem. Phys.* **2006**, *324*, 57–62.

(38) Gaudette, A. I.; Jeon, I. R.; Anderson, J. S.; Grandjean, F.; Long, G. J.; Harris, T. D. *J. Am. Chem. Soc.* **2015**, *137* (39), 12617–12626.

(39) Brunschwig, B. S.; Creutz, C.; Sutin, N. *Chem. Soc. Rev.* **2002**, *31* (3), 168–184.

(40) D'Alessandro, D. M.; Keene, F. R. *Chem. Soc. Rev.* **2006**, *35*, 424–440.

(41) Hush, N. *Progress in Inorganic Chemistry Vol. 8*; 1967.

(42) Abakumov, G. A.; Druzhkov, N. O.; Kurskii, Y. A.; Shavyrin, A. S. *Russ. Chem. Bull.* **2003**, *52* (3), 712–717.

(43) Brown, S. N. *Inorg. Chem.* **2012**, *51*, 1251–1260.

(44) Vogler, A.; Kunkely, H. *Comments Inorg. Chem.* **1990**, *9*, 201–220.

(45) Ito, T.; Ito, T.; Hamaguchi, T.; Nagino, H.; Yamaguchi, T.; Washington, J.; Kubiak, C. P. *Science.* **1997**, *277*, 660–663.

(46) Sutton, J. E.; Taube, H. *Inorg. Chem.* **1981**, *20*, 3125–3134.

(47) Sutton, S.; Taube. *Inorg. Chem.* **1979**, *18* (4), 1017–1021.

(48) Richardson, D. E.; Taube, H. *Coord. Chem. Rev.* **1984**, *60* (C), 107–129.

(49) Gispert, J. R. *Coordination Chemistry*; Wiley-VCH, 2008.

(50) Shimazaki, Y.; Daniel, T.; Stack, P.; Storr, T. *Inorg. Chem* **2009**, *48*, 8383–8392.

(51) Kennedy, S. R.; Kozar, M. N.; Yennawar, H. P.; Lear, B. J. *Inorg. Chem.* **2016**, *55*, 8459–

8467.

(52)   Leconte, N.; Moutet, J.; Constantin, T.; Molton, F.; Philouze, C.; Thomas, F. *Eur. J. Inorg. Chem.* **2018**, *2018* (16), 1752–1761.

(53)   Moseley, K.; Maitlis, P. M. *Chem. Commun.* **1971**, No. 982–983, 3–4.

(54)   Cherwinski, W. J.; Johnson, B. F. G.; Lewis, J. *J. Chem. Soc. Dalt. Trans.* **1974**, No. 13, 1405–1409.

(55)   Armarego, W. L. F.; Chai, C. L. L. *Purification of Laboratory Chemicals (5th Edition)*, 5th ed.; Butterworth-Heinemann, 2003.

(56)   Furche, F.; Ahlrichs, R.; Hättig, C.; Klopper, W.; Sierka, M.; Weigend, F. *Wiley Interdiscip. Rev. Comput. Mol. Sci.* **2014**, *4* (2), 91–100.

(57)   Schäfer, A.; Horn, H.; Ahlrichs, R. *J. Chem. Phys* **1992**, *97*, 2571.

(58)   Schäfer, A.; Huber, C.; Ahlrichs, R. *J. Chem. Phys* **1994**, *100*, 5829.

(59)   Stoll, S.; Schweiger, A. *J. Magn. Reson.* **2006**, *178*, 42–55.

Chapter 3

Square-Planar Platinum Complexes Containing Redox-Active

Ligands for Ligand-Based Hydrogen Atom Transfer Reactions

3.1 Introduction

The ability to manage proton and electron equivalents is a crucial component in the activation of small molecules such as N_2, O_2, CO, and CO_2. Therefore, the development of molecular systems that can readily mediate these transformations is of crucial importance for sectors such as renewable energy storage. The electrochemical reduction of CO_2 to methanol is a great target reaction for recycling carbon dioxide into fuel; however, as shown in equation 3.1, this reaction requires the coordinated delivery of six electrons and six protons, resulting in formidable mechanistic complications.

$$CO_2 + 6H^+ + 6e^- \rightarrow CH_3OH + H_2O \quad E^\circ(V \; vs. SHE \; at \; pH = 7) = -0.380 \quad (3.1)$$
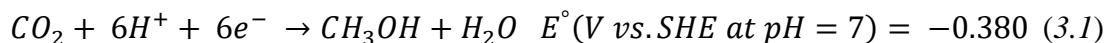
Reactions like the one described above can occur via proton (H^+), hydrogen atom ($H^\bullet$), or hydride transfer ($H\mathbf{:}^-$) and can be mediated by organic molecules,[1–5] transition metal hydrides,[6–9] or redox-active ligands coordination to transition metals (Figure 3.1).[10–19] Hydrogen atom transfer (HAT) describes reactions where the electron and proton are transferred in single kinetic step from a donor to an acceptor as $H^\bullet$. Transition metal complexes that can act as H-atom donors or abstractors constitute an active area of research. The two main types of inorganic HAT coordination complexes are: (1) metal hydrides in which HAT results in the formation or cleavage of the M–H bond, resulting in the transfer of $H^\bullet$, into or out of, respectively, the primary coordination sphere of metal, and (2) coordination complexes in which the metal serves as the electron source and a ligand serves as the proton source. A less common system, and the one described herein, is a coordination complex were both the electron and proton source is a redox-active ligand.[20,21]

65
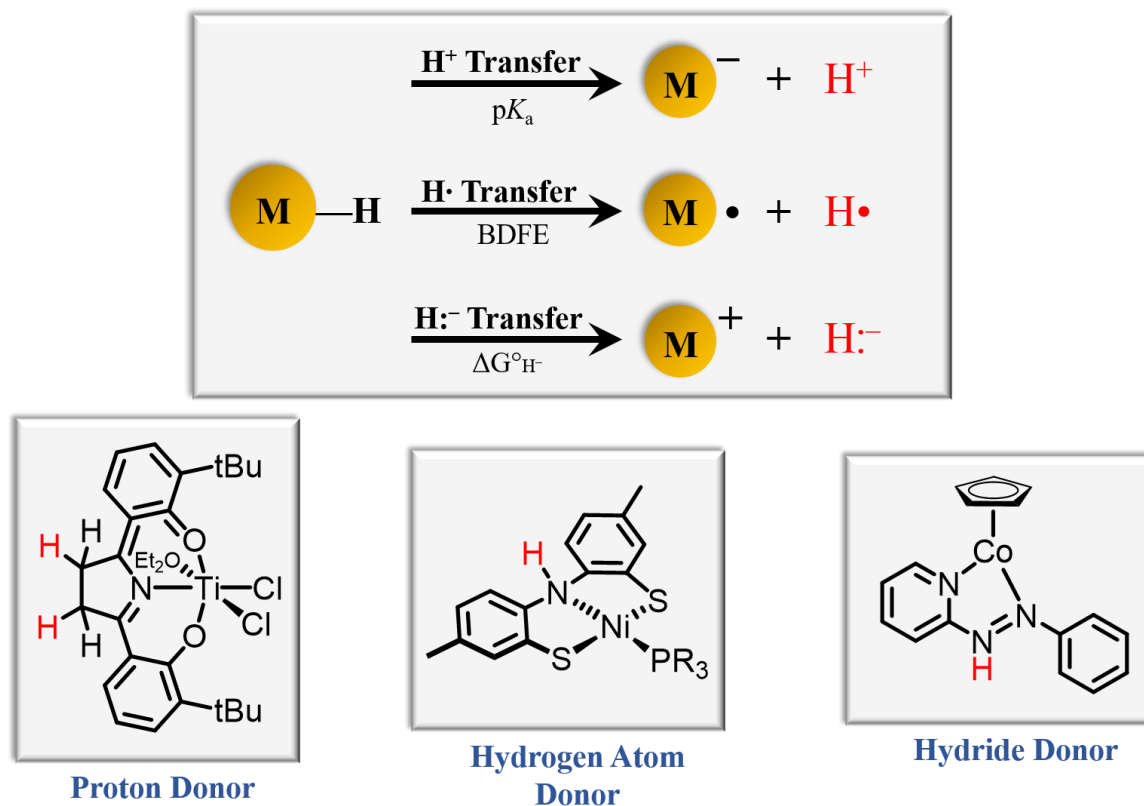
Figure 3.1. (*Top*) Types of hydrogen-based reactivity where M = transition-metal coordination complex. (*Bottom*) Examples of reported transition-metal complexes that function as proton,[22] H-atom,[23] or hydride donors,[19] respectively.

The use of transition metal complexes as HAT reagents gained attention largely because substrate oxidation via HAT was observed in metalloenzyme active sites. At present, the scope of transition metal mediated HAT is incredibly extensive. Figure 3.2 contains three examples that demonstrate the breadth of the field. The example in Figure 3.2(a) highlights a ruthenium metal-oxo that abstracts H• from a C–H bond in cumene to generate the carbon radical species.[24] In Figure 3.2(b) a H• is abstracted from a C–H bond in 9,10-dihydroanthracene, but in this case, the metal abstractor is a ferric bi-imidazole complex.[25] Both reactions occur by net transfer of H•, with the transfer of the e^- to the metal and H^+ to a ligand. In the case of $[Ru^{IV}O(bpy)_2py]^{2+}$, the Ru-oxo is unequivocally determined to be the abstracting agent. However, in $[Fe^{III}(Hbim)]^{2+}$ the identity of the abstracting agent is ambiguous. Despite the differences, both metal complexes have similar

rate constants (k) of 10^{-3}–10^{-2} M^{-1} s^{-1} and correlate on the same Evans-Polanyi line of log(k) vs.

reaction energy for the abstraction from dihydroanthracene.[26] This correlation was known for one

abstractor (X•) with a series of substrates (R–H) or one substrate with one class of abstractors (i.e.

oxyl radicals, halogen radicals). However, it was not expected for a series of disparate transition-

metal abstractors. These types of findings provided an incentive to investigate what factors caused

different abstractors to correlate on the same Evans-Polanyi line.
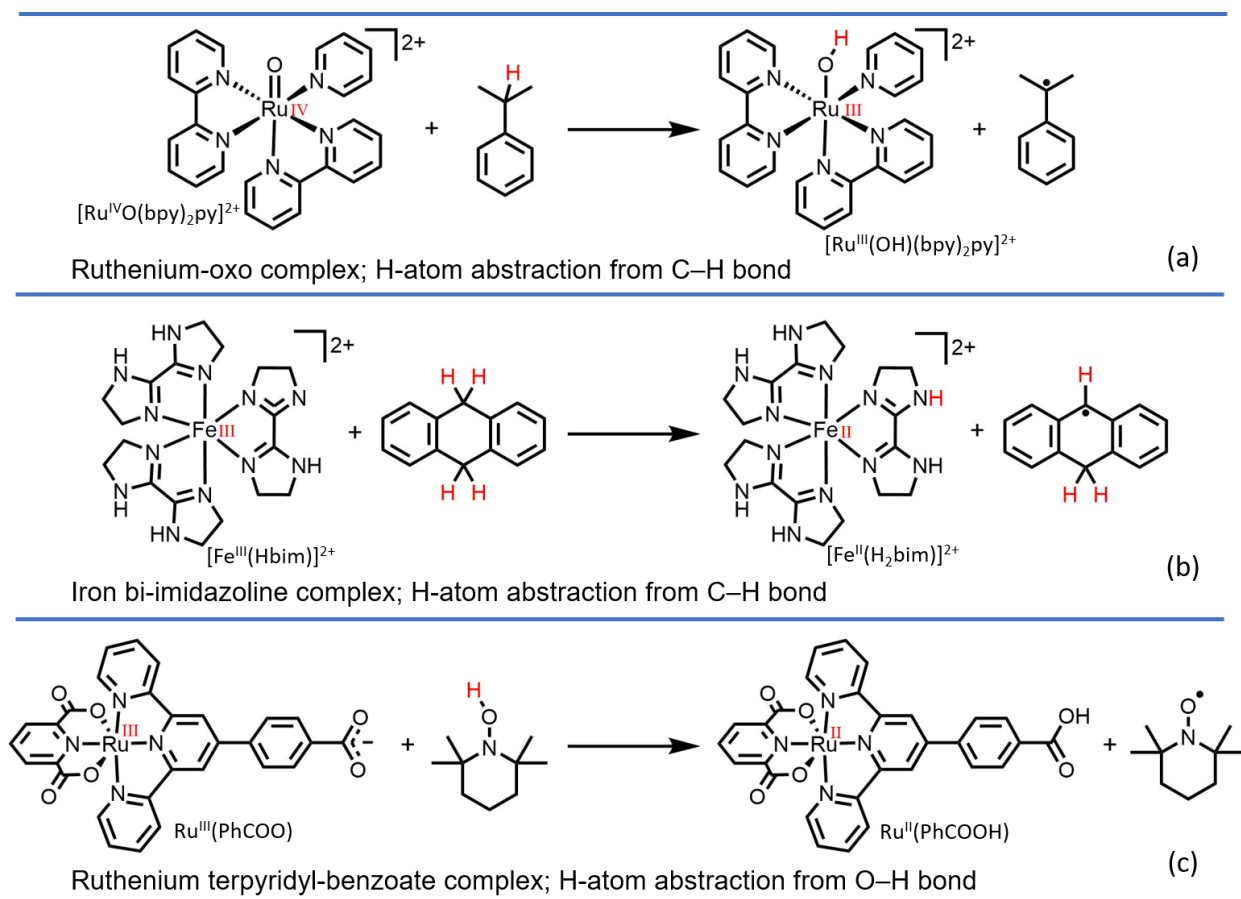
Figure 3.2. Examples of transition-metal mediated HAT reactions. (a) A ruthenium-oxo complex that abstracts H• from cumene in the first step of a multistep reaction.[24] (b) A ferric bi-imidazoline complex that abstracts H• from dihydroanthracene in the first step of a multistep reaction.[25] (c) A ruthenium terpyridyl-benzoate complex that abstracts H• via long-range CPET.[27]

Mayer et al. used the Marcus Cross Relation (Equation 3.2)[26] to examine and compare the HAT

reactivity of different systems.

$$k_{AH/B} = \sqrt{k_{AH/A}k_{BH/B}k_{eq}f} \qquad (3.2)$$

$$A - H + B \rightarrow A + H - B \qquad (3.3)$$

In HAT reactions, the cross relation predicts the rate constant, $k_{AH/B}$ for the cross reaction shown in Equation 3.3. As seen in equation 3.2, the kinetic information for $k_{AH/B}$ is predominately based on the rate constants for the respective hydrogen atom self-exchange reactions. They found that $[Ru^{IV}O(bpy)_2py]^{2+}$, $[Fe^{III}(Hbim)]^{2+}$, and other oxyl radicals had similar self-exchange rate constants (Ru = 8 x 10^4; Fe = 5.8 x 10^3 M^{-1} s^{-1}) which engender a linear correlation between the different species. Furthermore, they demonstrated that the cross relation could be used to explain and predict how different factors such as driving force, reorganization energy, spin character, solvent effects, and temperature influence HAT reactivity.[28]

Lastly, the example in Figure 3.2(c) demonstrates a ruthenium terpyridyl-benzoate complex that can abstract H$^\bullet$ from an O–H bond in TEMPOH. This is an interesting system because the transferred H$^\bullet$ is separated into the proton (H$^+$) that is added to the carboxylate and the electron (e$^-$) that reduces the Ru metal center 11 Å away.[27] Despite having net H$^\bullet$ transfer, some argue that it is more accurately defined as concerted proton-electron transfer (CPET) because of the separation between the acceptor sites. This exemplifies the gray area that begins to arise when considering the reaction mechanism of HAT. In this case, the rate constant for the reaction (1.1 x 10^5 M^{-1} s^{-1}) was similar to that observed in a similar system without the phenyl spacer. This was an interesting discovering considering that hydrogen (H$^+$) transfer from a substrate was three orders of magnitude slower for Ru^{III}(PhCOO) vs. Ru^{III}(COO). These examples are a small fraction of the extensive studies carried out to understand the thermodynamic and kinetic properties of

transition-metal mediated HAT. However, much less is known about the properties of noninnocent ligand platforms that can generate both the electron and proton equivalent for HAT.

Redox-active ligands are a particular class of ligands that can access multiple oxidation states and change oxidation states while coordinated to a metal ion. The term noninnocent was first used to describe a coordination complex, containing redox-active ligands, where the oxidation state of the metal remained ambiguous.[29] Catechol, which can exist in three different oxidation states is the prototypical example of a redox-active ligand (Figure 3.3).[30,31] In a coordination complex containing one or more redox-active ligands, redox reactions often lead to ligand-localized oxidation state changes that occur in conjunction with or in place of metal-based oxidation state changes.[32] Another form of noninnocence is one in which the ligand imparts significant interactions in the secondary coordination sphere. These typically include hydrogen-bonding, dipole, and van der Waals interactions which can stabilize reactive species or lower the activation barrier for a reaction.[33–35] A ligand that can store and transfer electrons and protons is hydrogen-atom noninnocent. The development of such platforms coordinated to a metal center is the focus of the work described herein.
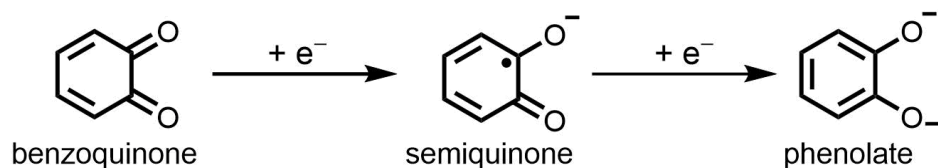
Figure 3.3. The prototypical redox-active ligand, catechol, in the three possible oxidation states.

The development of HAT ligands can provide novel approaches for stoichiometric and catalytic PCET like the one discussed in equation 3.1, but a detailed understanding of the thermodynamics and kinetics is required. This work reports on donor–acceptor platinum(II) complexes in which the redox-active, donor ligand [^{H}apH]$^{1-}$ ([^{H}apH] = 2,4-di-tert-butyl-6-(phenylamino)phenol) is proton

and hydrogen atom noninnocent. Moreover, [^{H}apH] was modified with various functional groups to determine if electronic modifications to the ligand could be used to tune HAT reactivity. Lastly, preliminary data on the synthesis and characterization of a palladium analog prepared to evaluate metal ion influence on ligand-based HAT reactivity, is presented.

3.2 Results

3.2.1 Synthesis of Donor–Acceptor M(^{R}ap)(^{X}bpy) Complexes and Protonated [M(^{R}apH)(^{X}bpy)]$^+$ Complexes.

The synthesis of square-planar group 10 metal complexes containing a redox-active donor ligand and diimine acceptor ligand are well established in the literature.[36–39] The goal of this study was to generate complexes that contained a redox-active ligand that could also become proton-active. The platinum and palladium starting materials, M(^{X}bpy)Cl$_2$ (X = H, tBu), were prepared according to literature procedures.[40,41] The ligand 2,4-di-tert-butyl-6-(phenylamino)phenol ([^{H}apH$_2$]) and all its derivatives, [^{R}apH$_2$] (R = CF$_3$, OMe, Me$_2$), were also prepared according to literature procedures.[42,43] The neutral donor–acceptor complexes were prepared by deprotonating the aminophenol ligand with two equivalents of potassium hydride and then adding the solution, dropwise, to a suspension M(^{X}bpy)Cl$_2$. From this reaction, M(^{R}ap)(^{X}bpy) (**1–6**) were isolated as dark blue-green solids in 50–60% yield (Scheme 3.1). Addition of one equivalent of triflic acid to the M(^{R}ap)(^{X}bpy) complexes resulted in protonation of the amidophenolate nitrogen to generate a cationic species characterized as [M(^{R}ap**H**)(^{X}bpy)]$^{1+}$ with triflate (CF$_3$SO$_3^-$) as the counter ion (Scheme 3.1, step 2). In a typical reaction, a THF solution of M(^{R}ap)(^{X}bpy) and an ether solution of triflic acid were frozen in a liquid N$_2$ cold-well. Upon thawing, the metal complex was treated with one equivalent of 0.5 M triflic acid under an inert N$_2$ atmosphere. As the triflic acid was added dropwise to the metal complex, there was an immediate color change from dark green-blue to a

bright orange-red. Concentration of the reaction solution and trituration with 2:1 pentane/ether solution resulted in the isolation of the products, [M(^{R}ap**H**)(^{X}bpy)][CF$_3$SO$_3$] (**1a–6a**), as a yellow-orange solids in approximately 90% yield with exception of the methoxy-functionalized complex which was isolated in a 58% yield.
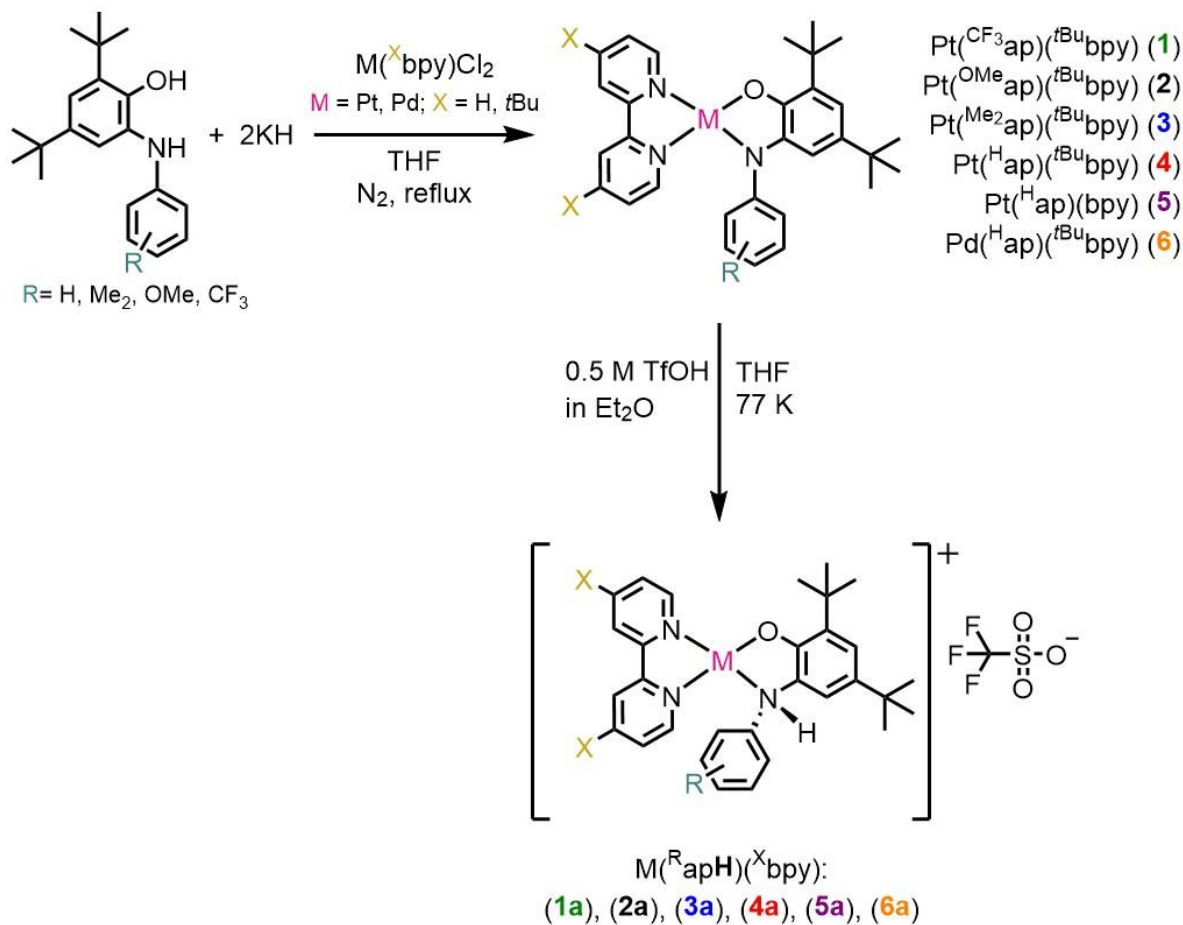
Scheme 3.1. Synthesis of M(^{R}ap)(^{X}bpy) Complexes and Protonated [M(^{R}ap**H**)(^{X}bpy)]$^+$ Analogs.

The neutral donor–acceptor complexes (**1–6**) were characterized by NMR spectroscopy. The ^{1}H NMR spectra of the six compounds showed sharp resonances in the normal diamagnetic region of the spectrum. The aromatic region contained resonances between 6 ppm and 10.5 ppm corresponding to the aromatic protons of the amidophenolate backbone, the aryl group of [^{R}ap]$^{2-}$, and the bipyridine backbone. A singlet at 3.23 ppm integrated to 6 protons for the methyl groups

of $[^{Me_2}ap]^{2-}$ and a singlet at 3.37 ppm integrated to 3 protons for the methoxy group in $[^{OMe}ap]^{2-}$.

The alkyl region contained 4 singlets corresponding to the methyl protons of the *tert*-butyl groups

on the amidophenolate ligand (~1.55 ppm and ~2.15 ppm) and the *tert*-butyl bipyridine ligand

(~0.78 ppm and ~0.94 ppm).

As expected, the protonated species were diamagnetic and displayed clearly resolved

resonances in the ^{1}H NMR spectrum. The aromatic signals shifted slightly downfield but remain

unchanged compared to the neutral unprotonated complexes. The four tert-butyl resonances have

shifted closer together as a result of the two lower frequency signals shifting downfield to ~1.14

ppm and ~1.07 ppm, and the two higher frequency signals shifting upfield to ~1.88 ppm and ~1.30

ppm. Lastly, a weak broad singlet appears at 11 ppm assigned to the N–H proton.

3.2.2 Structural Characterization of [M(^HapH)(^Xbpy)]⁺

Solid state structures have been reported for Pt(^{H}ap)(bpy) (complex **5** for this work) and

Pd(^{H}ap)(bpy) by Wieghardt and coworkers.[38] The previously published metrics for the d^8 metals

coordinated by 2,4-di-tert-butyl-6-(phenylamido)phenolate and bipyridine confirm the square-

planar geometry with a fully reduced amidophenolate ligand. The molecular structures of

$[Pt(^HapH)(^{tBu}bpy)]^{1+}$ (**4a**), $[Pt(^HapH)(bpy)]^{1+}$ (**5a**), and $[Pd(^HapH)(^{tBu}bpy)]^{1+}$ (**6a**) obtained from

single-crystal X-ray diffraction experiments are shown in Figure 3.4. The structural data

demonstrated that all three derivatives contain two bidentate ligands coordinated to the metal in a

square-planar geometry as denoted by τ_4 values of 0.06 for $[Pt(^HapH)(^{tBu}bpy)]^{1+}$ (**4a**), 0.07 for

$[Pt(^HapH)(bpy)]^{1+}$ (**5a**), and 0.07 for $[Pd(^HapH)(^{tBu}bpy)]^{1+}$ (**6a**). Selected metrical parameters

derived from the structural data for these complexes are presented in Table 3.1. The metal-

heteroatom distances are nearly identical for the three derivatives. In all three structures, the

intraligand C–O, C–N, and C–C bond distances bond were used to calculate ligand metrical oxidation states (MOSs) of –2.10, –2.20, and –2.21 for **4a**, **5a**, and **6a**, respectively.
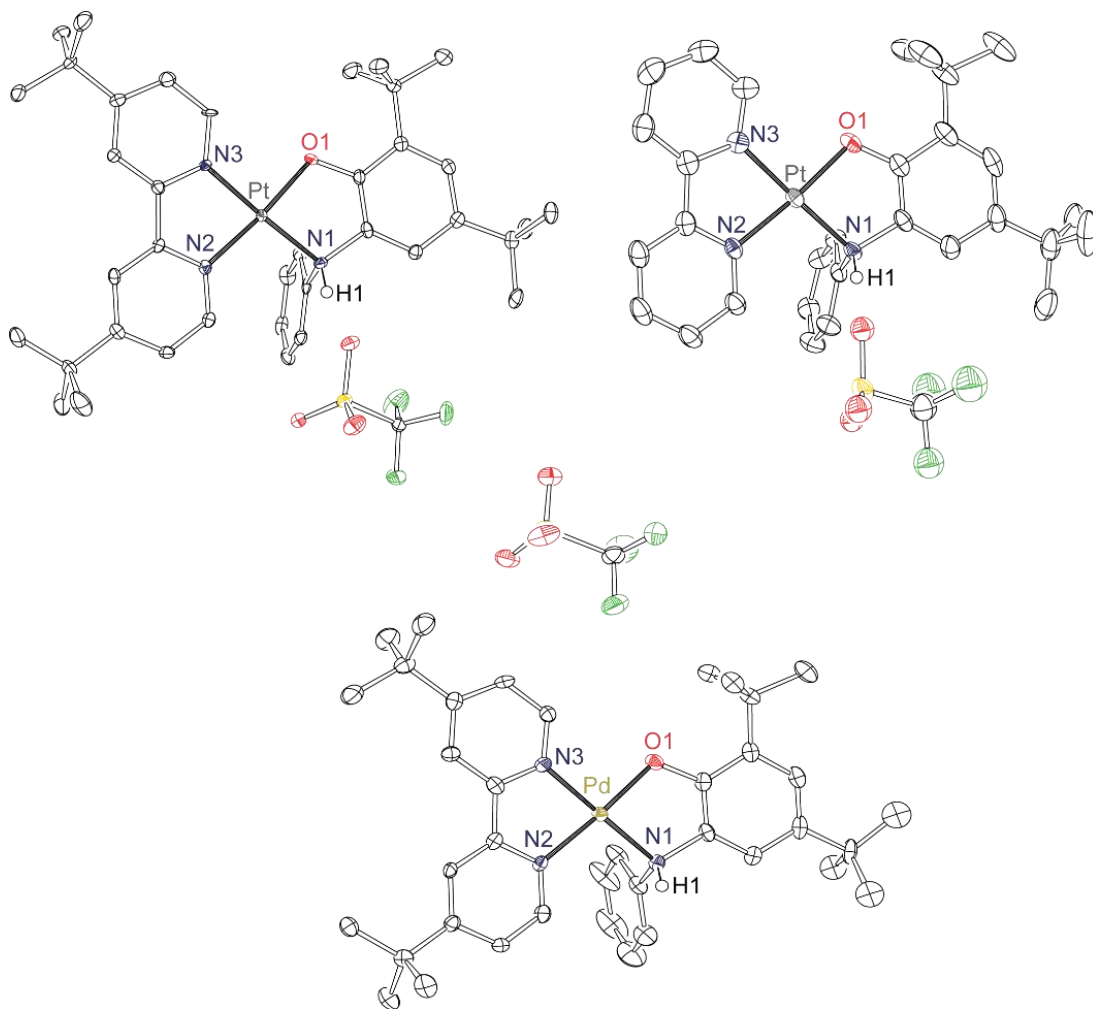
Figure 3.4. ORTEPs of [Pt(^{H}ap**H**)(^{tBu}bpy)]$^{1+}$ (*top left*), [Pt(^{H}ap**H**)(bpy)]$^{1+}$ (*top right*), and [Pt(^{H}ap**H**)(^{tBu}bpy)]$^{1+}$ (*bottom*). Ellipsoids are shown at 50% probability. Hydrogen atoms and solvent molecules have been omitted for clarity.

Table 3.1. Selected Bond Distances for [Pt(^{H}ap**H**)(^{tBu}bpy)]$^{1+}$, [Pt(^{H}ap**H**)(bpy)]$^{1+}$, and [Pt(^{H}ap**H**)(^{tBu}bpy)]$^{1+}$.

	[Pt(^{H}ap**H**)(L$_2$)]$^{1+}$	[Pt(^{H}ap**H**)(L$_2$)]$^{1+}$	[Pd(^{H}ap**H**)(L$_2$)]$^{1+}$
	L$_2$ = ^{tBu}bpy	L$_2$ = bpy	L$_2$ = ^{tBu}bpy
M–O$_1$	1.995(4)	1.989(2)	1.967(5)
M–N$_1$	2.047(4)	2.057(2)	2.061(6)
M–N$_2$	2.010(4)	2.008(2)	2.022(6)
M–N$_3$	2.002(5)	2.001(3)	2.000(7)
N$_1$–C$_1$	1.480(7)	1.487(3)	1.478(9)
O$_1$–C$_2$	1.344(7)	1.354(4)	1.343(10)
C$_1$–C$_2$	1.389(7)	1.382(4)	1.397(11)
C$_2$–C$_3$	1.432(7)	1.423(4)	1.422(11)
C$_3$–C$_4$	1.395(8)	1.389(5)	1.408(12)
C$_4$–C$_5$	1.404(8)	1.405(5)	1.391(13)
C$_5$–C$_6$	1.391(8)	1.386(4)	1.407(11)
C$_6$–C$_1$	1.383(8)	1.377(4)	1.387(10)
MOS	−2.10 ± 0.40	−2.20 ± 0.40	−2.21 ± 0.35

3.2.3 Electrochemistry

The redox processes of the square-planar complexes containing a Pt (or Pd) metal center coordinated to a redox-active amidophenolate and bipyridine ligand were examined using solution-phase voltammetric techniques. Figure 3.5 shows the cyclic voltammograms of the M(^{R}ap)(^{X}bpy) (**1–6**) complexes dissolved in acetonitrile containing 0.1 M [Bu$_4$N][PF$_6$] as the supporting electrolyte. The data was collected using a standard three-electrode configuration with a glassy carbon working electrode, a platinum wire counter electrode, and a silver wire pseudo-reference electrode. All reported potentials were referenced to [Cp$_2$Fe]$^{+/0}$, which was used as an internal standard. Table 3.2 reports the redox processes observed for each complex between –3.0 V and +1.5 V vs [Cp$_2$Fe]$^{+/0}$. As seen in Figure 3.5, complexes **1–6** each show four resolved redox processes: one reversible oxidation and one reversible reduction, as well as an irreversible oxidation and reduction. The donor amidophenolate ligand is in the fully reduced form, [^{H}ap]$^{2–}$

and therefore can undergo two, one electron oxidations which have been observed in complexes containing a related ligand framework.[38,39] The acceptor bipyridine ligand can be reduced by one electron to generate [bpy•]−; this redox event has been observed in related group 10 complexes containing a 2,2'-bipyridine or 4,4'-di-*tert*-butyl-2,2'- bipyridine ligand.[38,44]
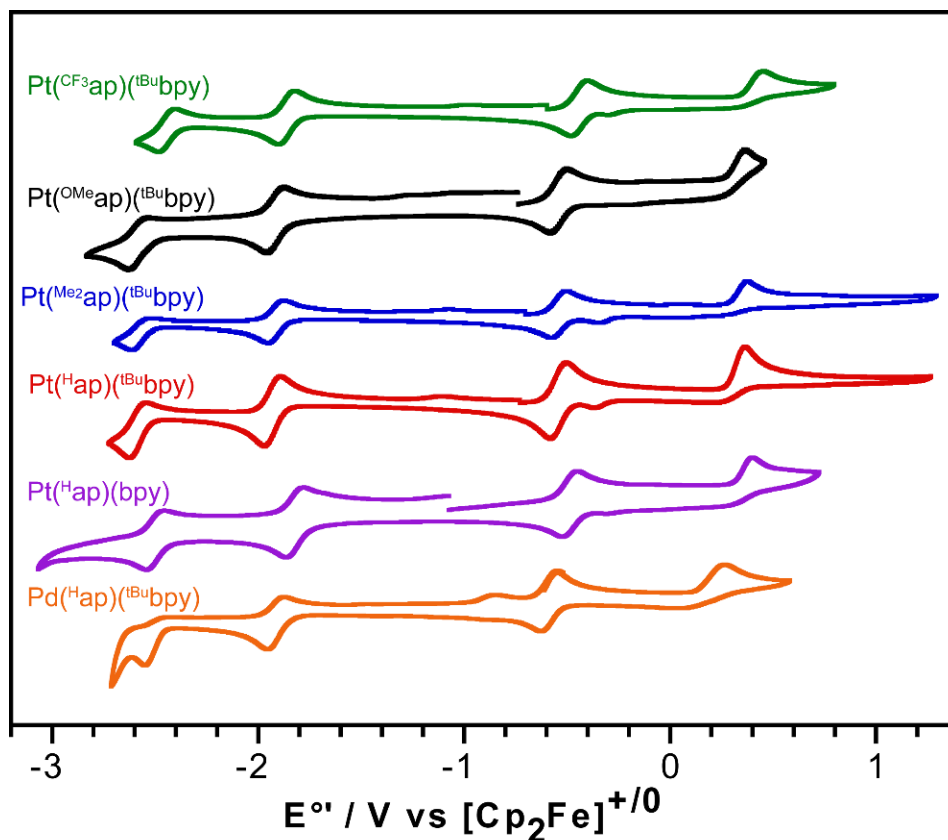
Figure 3.5. Cyclic voltammograms for M(^{R}ap)(^{X}bpy) dissolved in CH_3CN containing 0.1 M [Bu_4N][PF_6] at 200 mV sec^{-1}.

The redox events of most interest are the two oxidations that occur on the amidophenolate ligand. This ligand would be the source of the appropriate electron equivalents for hydrogen-atom (1st oxidation) and hydride transfer reactions (2nd oxidation). Notably, the first oxidation showed minor to no dependence on the functionalization of the amidophenolate ligand, [^{R}ap]$^{2-}$ (R = H, Me2, OMe, CF3). In the case of Pt(^{OMe}ap)(^{tBu}bpy) (**2**), Pt(^{Me2}ap)(^{tBu}bpy) (**3**), and Pt(^{H}ap)(^{tBu}bpy) (**4**) the potentials were all within error of one another at –0.52 to –0.54 V. Only Pt(^{CF3}ap)(^{tBu}bpy) (**1**)

75

showed a minor anodic shift to –0.44 V for the first oxidation. When the metal was changed from Pt to Pd in Pd(^{H}ap)(^{tBu}bpy) (**6**) the potential shifted cathodically to –0.59 V from –0.52 V observed in the platinum analog. The second oxidation had similar trends but was irreversible for all the complexes. As expected, the complexes showed similar potentials for the first reversible reduction of the bipyridine acceptor ligand except for Pt(^{CF_3}ap)(^{tBu}bpy) (**1**) and Pt(^{H}ap)(bpy) (**5**) which had a minor anodic shift from –1.93 V.

Table 3.2. Reduction potentials (V vs [Cp$_2$Fe]$^{+/0}$) for M(^{R}ap)(^{X}bpy) (**1–6**) dissolved in CH$_3$CN containing 0.1 M [Bu$_4$N][PF$_6$].

Complex	$E°'_1[M]^{2+/1+\ a}$	$E°'_2[M]^{1+/0}$	$E°'_3[M]^{0/1-}$	$E°'_4[M]^{1-/2-\ b}$
Pt(^{CF_3}ap)(^{tBu}bpy) (**1**)	0.45	–0.44	–1.86	–2.45
Pt(^{OMe}ap)(^{tBu}bpy) (**2**)	0.37	–0.54	–1.91	–2.58
Pt(^{Me_2}ap)(^{tBu}bpy) (**3**)	0.37	–0.54	–1.92	–2.61
Pt(^{H}ap) (^{tBu}bpy) (**4**)	0.37	–0.52	–1.93	–2.58
Pt(^{H}ap) (bpy) (**5**)	0.40	–0.48	–1.82	–2.50
Pd(^{H}ap)(^{tBu}bpy) (**6**)	0.27	–0.59	–1.91	–2.55

^{a,b} irreversible redox event

3.2.4 Electronic Spectroscopy

Solution UV-vis-NIR spectra were measured for the neutral and protonated cationic complexes to elucidate their electronic structures. The neutral donor–acceptor complexes, M(^{R}ap)(^{X}bpy) (**1–6**), are deeply colored both in the solid state and in solution, indicative of their strong absorption properties in the UV-vis-NIR regions of the electromagnetic spectrum. Figure 3.6 shows the absorption spectrum of complexes (**1–6**) (*top left*) in acetonitrile at 298 K. Table 3.3 summarizes the key metrics for the various functionalized derivatives which have similar spectroscopic features. Complexes (**1–6**) have a characteristic band in the 680–750 nm region, with molar absorptivity values of 4,300–8,500 M^{-1} cm^{-1} for the platinum complexes and 3,200 M^{-1} cm^{-1} for the palladium complex (**6**), along with a less intense transition (~2,500 M^{-1} cm^{-1}) around 400 nm. These transitions are typically characterized as intense $\pi \rightarrow \pi^*$, ligand-to-ligand charge

76

transfer (LL'CT) and have been observed in complexes of this type and considered to be highly independent of metal identity.[39] In the protonated $[M(^RapH)(bpy)]^{1+}$ cations, the electronic absorption bands >500 nm are no longer present, and only the moderate transition around 400 nm remains, as seen in Figure 3.6 (*top right*), with molar absorptivity values of 2,000–3,000 M^{-1} cm^{-1} for platinum and 1,100 M^{-1} cm^{-1} for the palladium analogue.
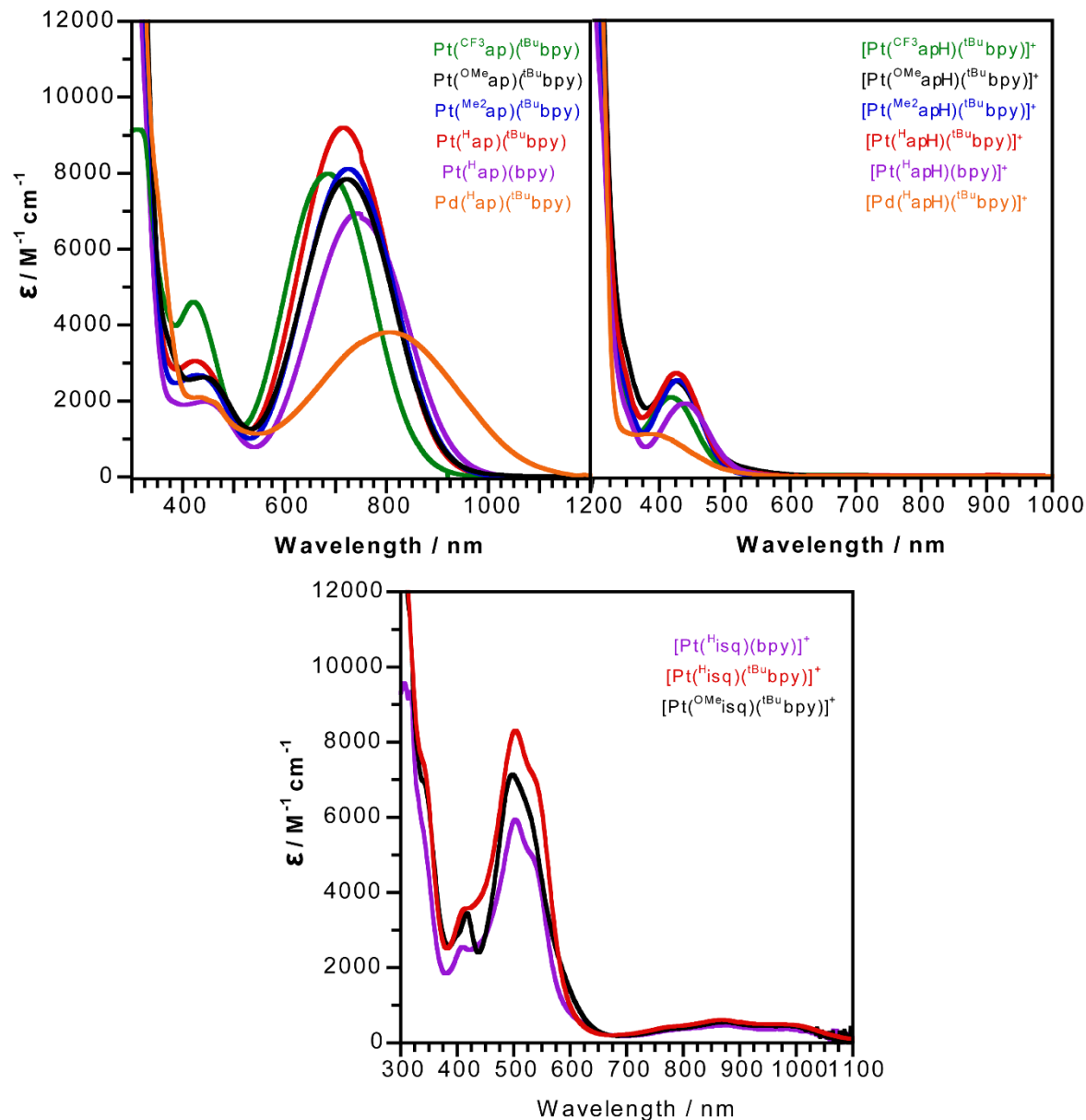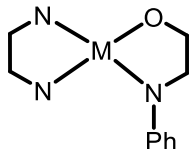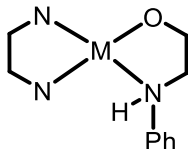
Figure 3.6. Electronic absorption spectra for $M(^Rap)(^Xbpy)$ (**1–6**) (*top left*), $[M(^RapH)(^Xbpy)]^{1+}$ (**1a–6a**) (*top right*), and $[Pt(^Risq^•)(^Xbpy)]^{1+}$ (*bottom center*) in CH_3CN at 298K.

Successful H• transfer from one of the protonated cations, $[M(^RapH)(^Xbpy)]^{1+}$ should result in the formation of a cationic radical complex of the form: $[M(^Risq^\bullet)(^Xbpy)]^{1+}$. In order to characterize products of HAT reactivity studies, iminosemiquinonate complexes were directly generated by chemical oxidation of $Pt(^{OMe}ap)(^{tBu}bpy)$ (**2**), $Pt(^Hap)(^{tBu}bpy)$ (**4**), and $Pt(^Hap)(^Hbpy)$ (**5**) using silver hexafluorophosphate and characterized by absorption spectroscopy. Each complex generated the respective species, $[Pt(^Risq^\bullet)(^Xbpy)]^+$ (**2b**, **4b**, **5b**), with a single radical O,N-coordinated ligand. As shown by Wieghardt and coworkers for $[Pt(^Hisq^\bullet)(bpy)]^{1+}$,[38] this π-radical ligand displays multiple bands in the visible region at: 410 (2100 M^{-1} cm^{-1}), 502 (4800 M^{-1} cm^{-1}), 540 (3900 M^{-1} cm^{-1}), and a broad band ranging from 700−1050 nm (500 M^{-1} cm^{-1}) (Figure 3.6, *bottom center*).

Table 3.3. Electronic Absorption Data for the neutral $M(^Rap)(^Xbpy)$, protonated $[M(^RapH)(^Xbpy)]^{1+}$, and cationic radical $[Pt(^Risq^\bullet)(^Xbpy)]^{1+}$ complexes. All spectra were collected in CH_3CN at 298 K.

Metal	L₁(ON)	L₂(NN)	$\bar{v}_{max}$ / nm (ε_{max} / M^{-1} cm^{-1})	$\bar{v}_{max}$ / nm (ε_{max} / M^{-1} cm^{-1})
Pt	^{CF_3}Ph-ap	^{tBu}bpy	415 (2900), 686 (4300)	418 (2100)
Pt	^{OMe}Ph-ap	^{tBu}bpy	441 (2600), 722 (7700)	425 (2500)
Pt	^{OMe}Ph-isq•	^{tBu}bpy	417 (3500), 497 (7000), 700–1050 (550)	--
Pt	^{Me_2}Ph-ap	^{tBu}bpy	428 (2700), 725 (8000)	428 (2500)
Pt	^{H}Ph-ap	^{tBu}bpy	425 (3100), 712 (8400)	427 (2700)
Pt	^{H}Ph-isq•	^{tBu}bpy	406 (3500), 504(8200), 544 (7000), 700–1050 (600)	--
Pt	^{H}Ph-ap	bpy	443 (2000), 742 (7000)	439 (1900)
Pt	^{H}Ph-isq•	bpy	410 (2500), 502 (5900), 537 (4900), 700–1050 (470)	--
Pd	^{H}Ph-ap	^{tBu}bpy	433 (2100), 684 (3200)	387(1100)

3.2.5 EPR Spectroscopy

HAT reaction products could also be analyzed using EPR spectroscopy. Therefore, the electronic structures of the one-electron oxidized complexes $[Pt(^Hisq^•)(^{tBu}bpy)]^{1+}$, $[Pt(^Hap)(^Hisq^•)]^{1+}$, and $[Pt(^{OMe}isq^•)(^{tBu}bpy)]^{1+}$ were characterized by X-band solution EPR acquired at 77 K. As previously stated, solutions of the iminosemiquinonate cations were prepared by treating the corresponding $Pt(^Rap)(^Xbpy)$ complex with one equivalent of $AgPF_6$ in acetonitrile followed by filtration to remove silver metal. Figure 3.7 shows the EPR spectra for iminosemiquinonate complexes, while Table 3.4 presents the g-tensors and hyperfine coupling constants used to simulate each spectrum. As expected for the one-electron oxidized species, the three spectra are consistent with $S = \frac{1}{2}$ system. A single broad isotropic signal was observed at g = 2.00 for $[Pt(^Hisq^•)(^{tBu}bpy)]^{1+}$ and $[Pt(^{OMe}isq^•)(^{tBu}bpy)]^{1+}$, with coupling to the heavy platinum metal center and a single ^{14}N nuclei. As expected, the previously reported $[Pt(^Hisq^•)(bpy)]^{1+}$ gave a rhombic spectra with three distinct g values; hyperfine coupling constants for two different nitrogen atoms were resolved along with coupling of the unpaired electron to the platinum metal center.[38] The signals observed substantiate that the complexes contain an O,N-coordinated iminosemiquinonate radical.
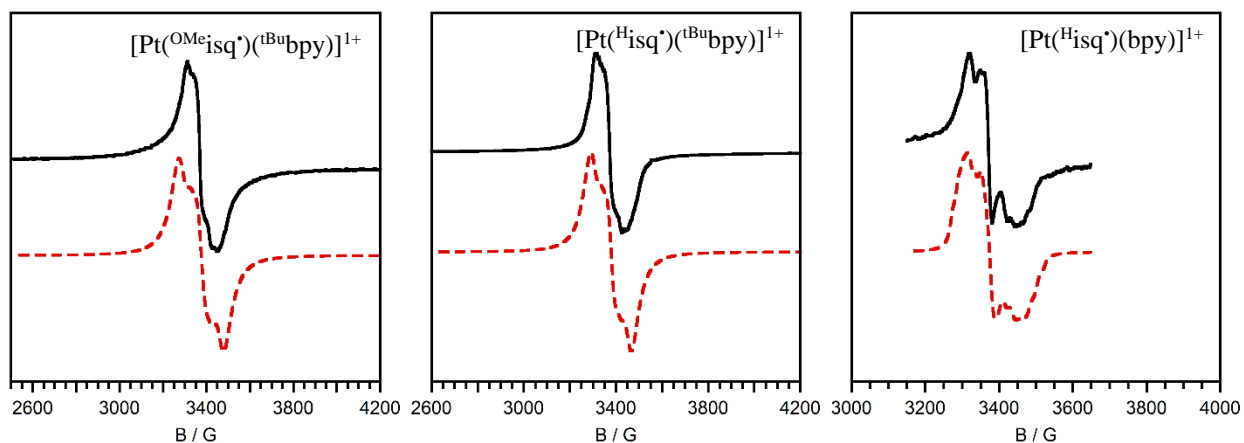
Figure 3.7. X-band EPR spectra of one-electron oxidized cations: $[Pt(^{OMe}isq^•)(^{tBu}bpy)]^{1+}$ (*left*), $[Pt(^Hisq^•)(^{tBu}bpy)]^{1+}$ (*center*), and $[Pt(^Hisq^•)(bpy)]^{1+}$ (*right*). All spectra were recorded at 77 K in CH_3CN

Table 3.4. g-Tensors and hyperfine coupling constants for one-electron oxidized [Pt(^{R}isq$^\bullet$)(^{X}bpy)][PF$_6$] (**2b, 4b, 5b**) iminosemiquinonate complexes.

	g_1	g_2	g_3	a_1 / MHz (nuclei)	a_2 / MHz (nuclei)	a_3 / MHz (nuclei)
[Pt(^{OMe}isq$^\bullet$)(^{tBu}bpy)]$^{1+}$	2.00	--	--	120 (^{14}N) 230 (^{195}Pt)	--	--
[Pt(^{H}isq$^\bullet$)(^{tBu}bpy)]$^{1+}$	1.99	--	--	100 (^{14}N) 203 (^{195}Pt)	--	--
[Pt(^{H}isq$^\bullet$)(bpy)]$^{1+}$	1.94	1.99	2.04	59 (^{14}N) 41 (^{14}N) 69 (^{195}Pt)	20 (^{14}N) 31 (^{14}N)	34 (^{14}N) 51 (^{14}N)

3.2.6 Determination of pK_a and Bond Strength

Determination of the pK_a is important because it characterizes the acid strength of the ligand N–H bond, and more importantly, can be used with the redox potential to calculate the bond dissociation free energy (BDFE). Given that the neutral complexes and protonated cationic complexes have very different spectroscopic features in the UV-Vis region of the electromagnetic spectrum, the pK_a values of [^{R}ap**H**]$^{1-}$ could be readily determined by spectrophotometric titrations using a previously reported method.[45] Accordingly, the portion-wise addition of 2,4,6-trimethylpyridine (pK_a (CH$_3$CN) = 14.98) or 4-aminopyridine (pK_a (CH$_3$CN) = 17.62) to an acetonitrile solution of the selected [Pt(^{R}ap**H**)(^{X}bpy)]$^{1+}$ complex (**1a–5a**), resulted in the growth of a charge-transfer band around 700 nm, characteristic of the neutral deprotonated complexes (**1–5**). From the spectrophotometric titration data, a pK_a of 18.5 ± 0.2 was determined for the unfunctionalized [Pt(^{H}ap**H**)(^{tBu}bpy)]$^{1+}$ (**4a**), Figure 3.8(*top*). For [Pt(^{H}ap**H**)(bpy)]$^{1+}$ (**5a**), in which the *tert*-butyl groups have been removed from bipyridine, a slightly more acidic pK_a of 17.8 ± 0.3 was determined, Figure 3.8(*bottom*). The analogous spectrophotometric titrations performed on the other complexes in the series, [Pt(^{CF_3}ap**H**)(^{tBu}bpy)]$^{1+}$ (**1a**), Pt(^{OMe}ap**H**)(^{tBu}bpy)]$^{1+}$ (**2a**), and Pt(^{Me_2}ap**H**)(^{tBu}bpy)]$^{1+}$ (**3a**) are shown in Figure 3.9. Using the pK_a values determined by spectrophotometric titration and the redox potential for the first oxidation (Table 3.2, E$^{o'}_2$) the

BDFE was determined using equation 3.4, where C_G is the solvent constant defined as 54.9 kcal mol^{-1} in CH$_3$CN.

$$BDFE = 1.37\big(pK_a(MH)\big) + 23.06(E'^{\circ}) + C_G \tag{3.4}$$

All the pK_a values and bond dissociation free energy (BDFE) values calculated from the Bordwell equation are summarized in Table 3.5.
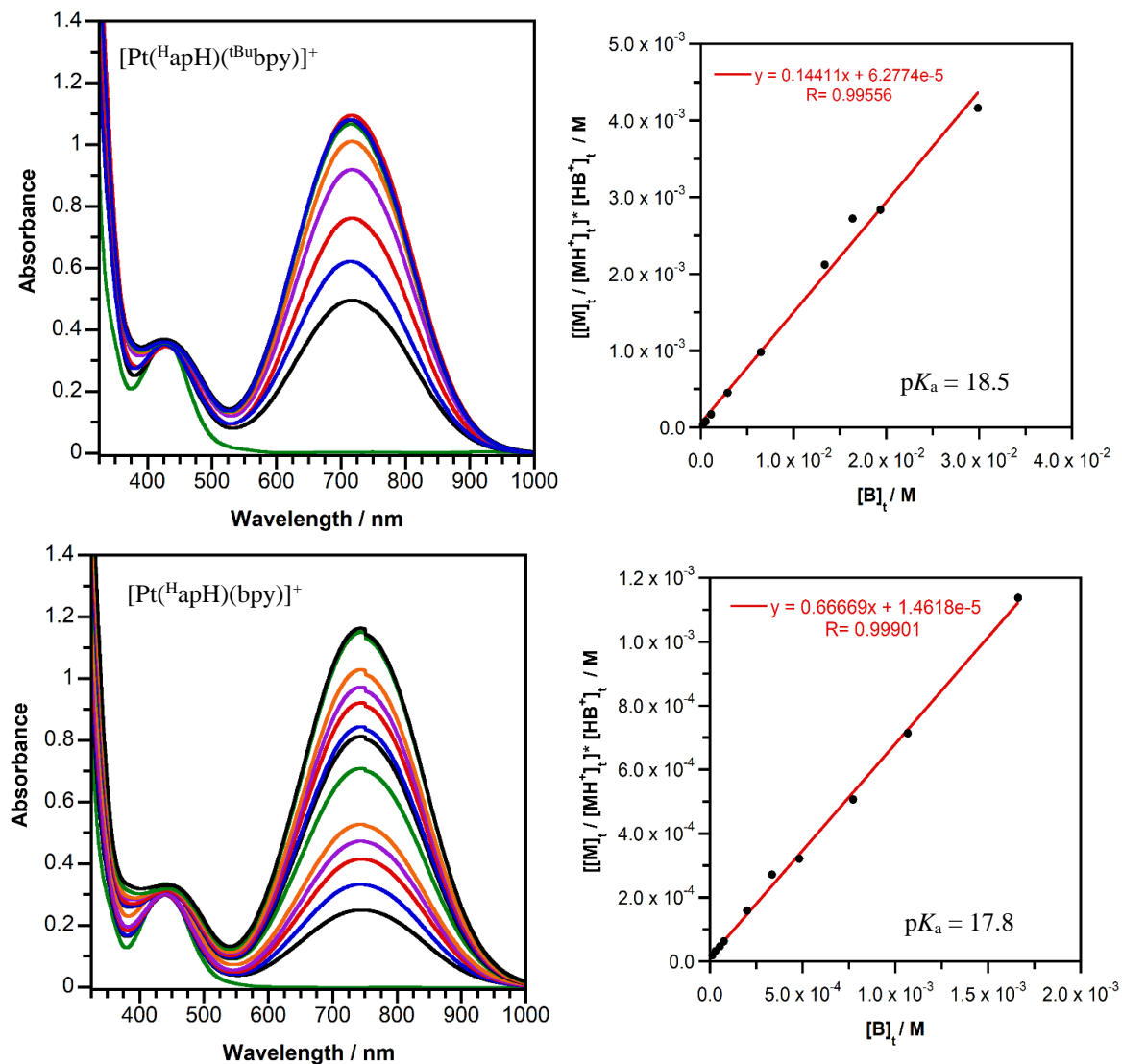
Figure 3.8. Electronic absorption titrations of [Pt(^{H}ap**H**)(^{tBu}bpy)]$^{1+}$ (*top left*) and [Pt(^{H}ap**H**)(bpy)]$^{1+}$ (*bottom left*) in the presence of 4-aminopyridine. (*Right*) Plots of base concentration ([B]$_t$) vs. concentration of deprotonated metal complex ([M]$_t$) used to calculate K_{eq} and pK_a.
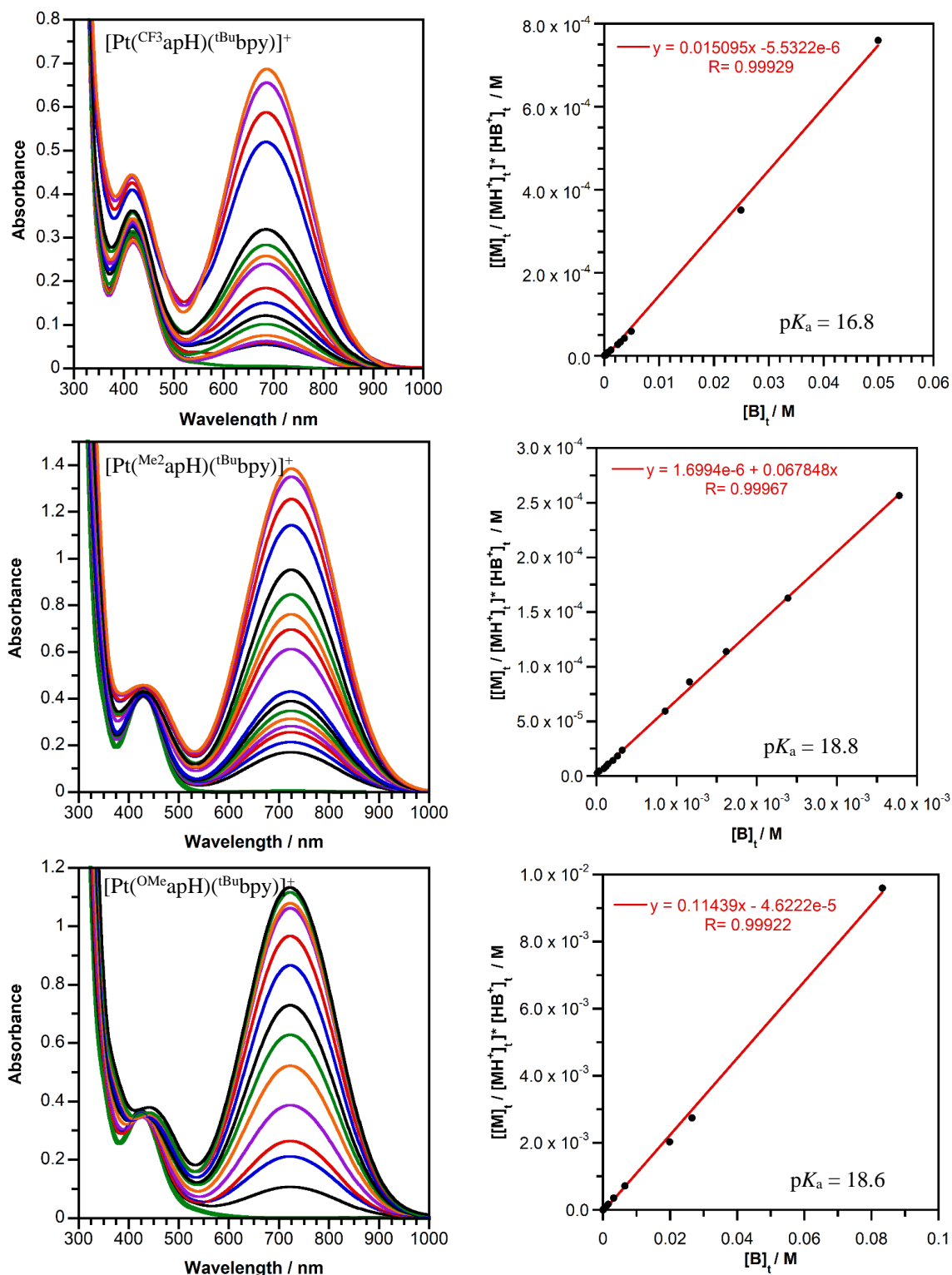
Figure 3.9. Electronic absorption titrations of $[Pt(^{R}ap\mathbf{H})(^{tBu}bpy)]^{1+}$ R = CF$_3$ (*top left*), Me$_2$ (*left center*), and OMe (*left bottom*) in the presence of the appropriate base. (*Right*) Plots of base concentration ([B]$_t$) vs. concentration of deprotonated metal complex ([M]$_t$) used to calculate K_{eq} and pK_a.

Table 3.5. Experimentally determined pK_a values of [M(^{R}ap**H**)(^{X}bpy)]$^{1+}$ cations in CH$_3$CN at 298 K using the indicated base for spectrophotometric titrations. BDFE values calculated using pK_a and redox potential (E°'$_2$).

Complex	pK_a	Base	BDFE (kcal mol^{-1})
Pt(^{CF_3}ap**H**)(^{tBu}bpy) (**1a**)	16.8 ± 0.3	2,4,6-trimethylpyridine	67.7 ± 0.9
Pt(^{OMe}ap**H**)(^{tBu}bpy) (**2a**)	18.6 ± 0.02	4-aminopyridine	67.9 ± 0.5
Pt(^{Me_2}ap**H**)(^{tBu}bpy) (**3a**)	18.8 ± 0.3	4-aminopyridine	68.0 ± 0.9
Pt(^{H}ap**H**)(^{tBu}bpy) (**4a**)	18.5 ± 0.2	4-aminopyridine	68.2 ± 0.7
Pt(^{H}ap**H**)(bpy) (**5a**)	17.8 ± 0.3	4-aminopyridine	68.2 ± 0.9

Titrations of the palladium derivative [Pt(^{H}ap**H**)(^{tBu}bpy)]$^{1+}$(**6a**) were attempted with 2,4,6-trimethylpyridine and 4-aminopyridine but pK_a values could not be extrapolated from the data. The solutions of **6a** and base had greater air sensitivity than any of the platinum derivatives and were not stable for > 2 hours, evident by a color change to dark red. Furthermore, inconsistencies in the absorption features suggest compound degradation.

3.2.7. Hydrogen Atom Transfer Reactivity

To test the viability of the protonated aminophenolate complexes [Pt(^{R}ap**H**)(^{X}bpy)]$^{1+}$ (**1a–5a**) as HAT reagents, reactions of [Pt(^{H}ap**H**)(^{tBu}bpy)]$^{1+}$ (**4a**), [Pt(^{H}ap**H**)(^{H}bpy)]$^{1+}$ (**5a**), and [Pt(^{OMe}ap**H**)(^{tBu}bpy)]$^{1+}$ (**2a**) with galvinoxyl radical (BDFE = 74.1 kcal/mol for galvinol in C$_6$H$_6$)[46] were investigated by UV-vis and EPR spectroscopy. The reaction of **2a**, **4a**, and **5a** with one equivalent of galvinoxyl radical resulted in a progressive color change from dark yellow-green to a deep dark red. Figure 3.10(*left*) shows the electronic absorption spectra for the starting materials, [Pt(^{H}ap**H**)(bpy)]$^{1+}$ (**5a**) (orange trace) and galvinoxyl radical (blue trace), and the product mixture (black trace) after 24 hours. The reaction mixture was taken to dryness under reduced pressure to obtain an orange-red solid. From this solid, a yellow product was extracted into pentane leaving behind a paramagnetic magenta-colored solid. This was consistent in the reactions of Pt(^{H}ap**H**)(^{tBu}bpy)]$^{1+}$ (**4a**) and [Pt(^{OMe}ap**H**)(^{tBu}bpy)]$^{1+}$ (**2a**) with galvinoxyl. The yellow product was

diamagnetic, and the ^{1}H NMR spectrum displayed 4 signals in the aromatic region from 6.88–7.80 ppm integrating to the total of 5 protons, a small broad singlet at 5.19 ppm, and 3 singlets in the alkyl region at 1.55 (9H), 1.48 (9H), and 1.35 (18H) ppm. Figure 3.10 (*right*) superimposes the reaction mixture (black trace) with the two isolated products: the yellow oil (green trace) and the paramagnetic magenta-colored solids (pink trace). The isolated products generate the reaction mixture spectrum and do not resemble the spectra of starting materials in Figure 3.10 (*left*).
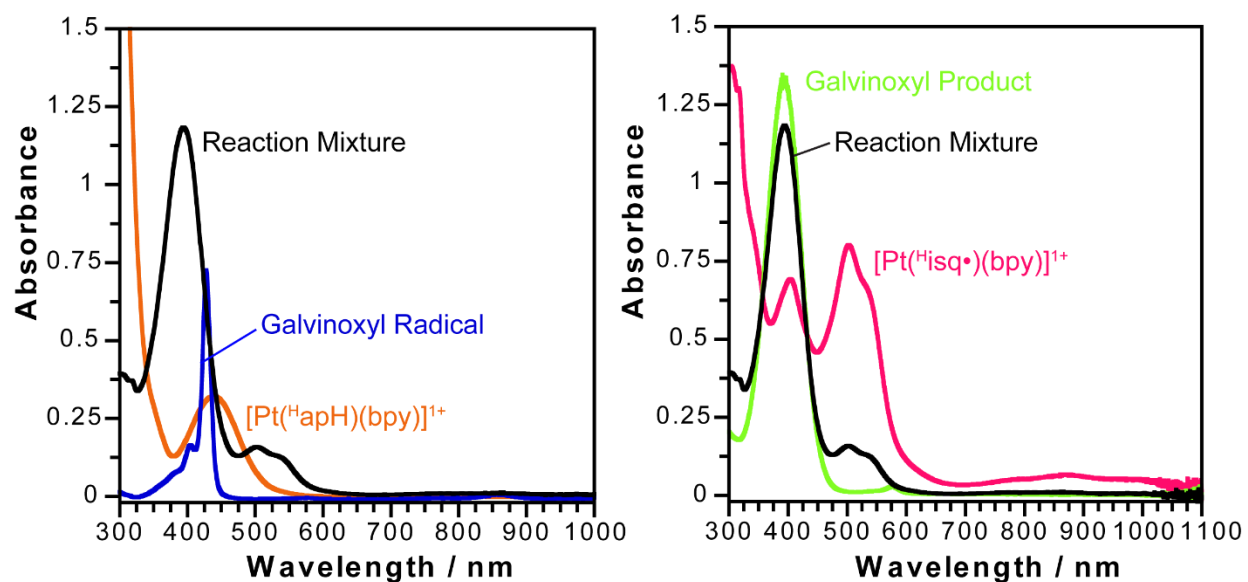
Figure 3.10. (*Left*) Electronic absorption spectra of HAT starting materials and reaction mixture after 24 hours. (*Right*) Electronic absorption spectra of HAT reaction mixture and the isolated reaction products. All spectra were collected in CH$_3$CN at 298 K.

The paramagnetic HAT reaction products were also characterized by EPR spectroscopy. All three products were consistent with a $S = \frac{1}{2}$ system. A single broad isotropic signal was observed at g = 2.00 for the HAT reaction product of [Pt(^{H}ap**H**)(^{tBu}bpy)]$^{1+}$ and [Pt(^{OMe}ap**H**)(^{tBu}bpy)]$^{1+}$, with hyperfine interactions. The [Pt(^{H}ap**H**)(bpy)]$^{1+}$ reaction product gave a rhombic spectrum with three distinct *g* values and significant hyperfine interactions. Figure 3.11 shows the EPR spectrum of the reaction products (*gray trace*) stacked below the EPR spectrum of the analogous, chemically generated [Pt(^{R}isq$^•$)(^{X}bpy)]$^{1+}$ complex (*pink traces*).
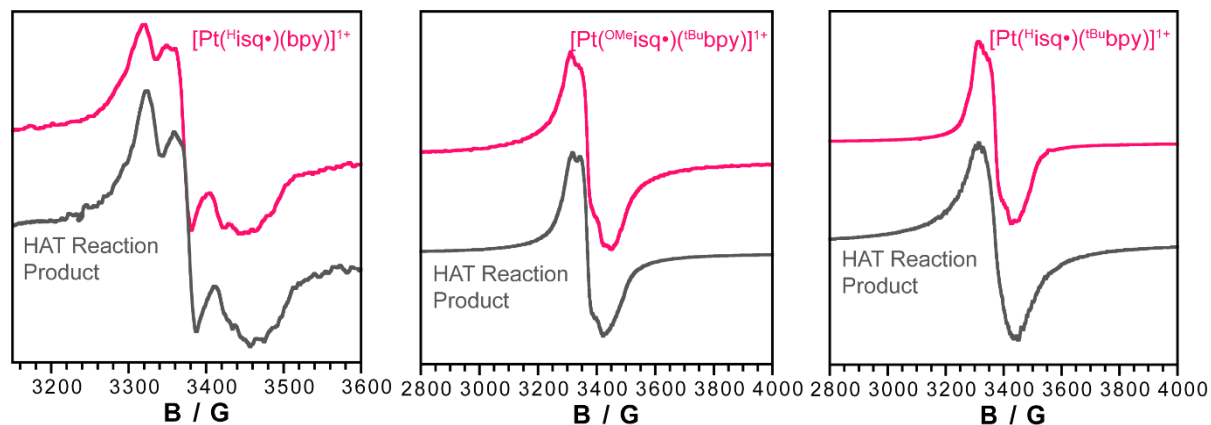
Figure 3.11. X-band EPR spectra of the chemically oxidized [Pt(^{H}isq$^•$)(bpy)]$^{1+}$ (*left*), [Pt(^{OMe}isq$^•$)(^{tBu}bpy)]$^{1+}$ (*center*), and [Pt(^{H}isq$^•$)(^{tBu}bpy)]$^{1+}$ (*right*) shown as pink traces, and the analogous HAT reaction products (*gray traces*). All spectra were recorded at 77 K in CH$_3$CN.

3.3 Discussion

The synthesis of a series of neutral donor–acceptor complexes that could be successfully protonated at the ligand amine group, to produce an air-stable complex, provided a promising platform for hydrogen-atom transfer reactivity. The cationic protonated derivatives (**1a–6a**) were synthesized by treating the neutral complexes with one equivalent of triflic acid. All the protonated species had consistent ^{1}H NMR spectra that displayed a downfield shift of all the resonances in comparison to their deprotonated analogs. Crystallographic analysis of [Pt(^{H}ap**H**)(^{tBu}bpy)]$^{1+}$ (**4a**), [Pt(^{H}ap**H**)(bpy)]$^{1+}$ (**5a**), and [Pd(^{H}ap**H**)(^{tBu}bpy)]$^{1+}$ (**6a**) established the structural features of the square-planar metal(II) protonated species. In previously reported structures of M(^{R}ap)(^{X}bpy), the amidophenolate nitrogen to phenyl ring bond is closely aligned to the metal-heteroatom plane (C(7)-N(1)-Pd(1) = 123.0°). The structures reported herein, demonstrate that upon protonation the phenyl ring is pushed behind the metal-heteroatom plane (C(15)-N(1)-Pt(1) = 113.1(3)°).

Coordination of the redox-active amidophenolate ligand and a bipyridine ligand to a Pt(II)/Pd(II) center generates complexes with low-energy charge-transfer absorptions in the electronic spectrum. Based on the spectroscopic data obtained, the intense absorption bands around 700 nm have been assigned as LL′CT transitions, corresponding to the transfer of an electron from

the amidophenolate ligand to the bipyridine. These transitions are typically observed in complexes of this type and tend to be highly independent of metal and donor atom identity.[39,47] Upon protonation, the $[M(^RapH)(^Xbpy)]^{1+}$ cations lost the low-energy transition around 700 nm and only had one moderate transition around 400 nm corresponding to a metal-to-ligand charge transfer. The band at 700 nm is a result of a LL'CT transition from the amidophenolate localized HOMO to the bipyridine localized LUMO. Upon protonation, the amidophenolate localized orbital interacts with the H^+ ion to generate the N–H sigma bond. This new bond significantly lowers the energy of the orbital, leading to the loss of the 700 nm transition.

The redox properties of the neutral $M(^Rap)(^Xbpy)$ complexes (**1–6**) were probed by cyclic voltammetry. The redox properties of the two oxidations are of interest because they are the source of electron equivalents for hydrogen atom (H•) and hydride transfer (H:⁻). The potential of the first oxidation ($E°'_2$, Table 3.2) ranges from −0.44 to −0.54 V for all of the platinum complexes. The nearly identical oxidation potentials for $Pt(^Hap)(^{tBu}bpy)$ (**4**), $Pt(^{Me2}ap)(^{tBu}bpy)$ (**3**), and $Pt(^{OMe}ap)(^{tBu}bpy)$ (**2**) suggest that there is not significant electron-donation from the methyl and methoxy substituents to influence the oxidation potential. The largest difference was observed for $Pt(^{CF3}ap)(^{tBu}bpy)$ (**1**) which was shifted in the anodic direction by 80 mV; as expected the electron withdrawing nature of the CF_3 makes it more difficult to oxidize the ligand. Figure 3.12 shows a plot of the $E°'_2$ values for **1–4** plotted against the substituent Hammett constant (σ), which is used to describe the relationship between reaction rates and reaction equilibrium in systems were the only variable is the nature and position of the substituent. The redox potentials ($E°'_2$) do not have a strong linear correlation with the Hammett substituent constant, which indicates that the electrochemical potential of these systems cannot be directly tuned based on the choice of the ligand substituent.
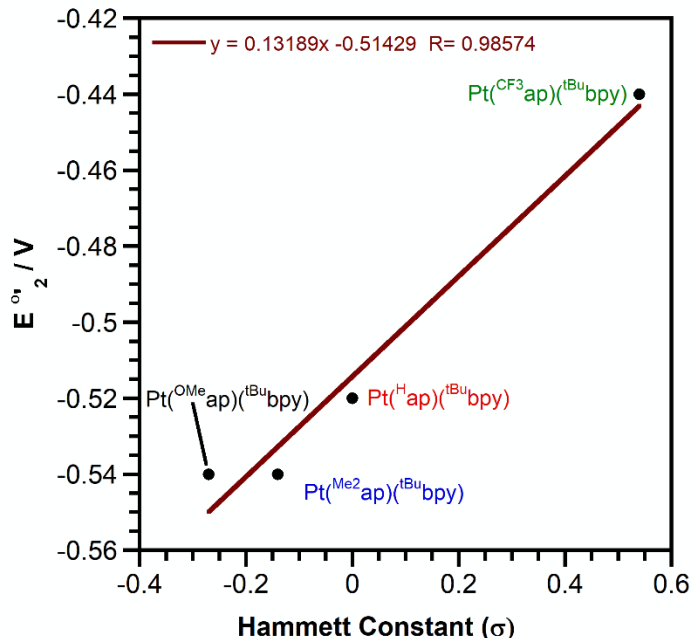
Figure 3.12. Potential of the first oxidation ($E°'_2$) versus the Hammett constant for **1–4**.

One possible explanation is that complex **2**, Pt(^{OMe}ap)(^{tBu}bpy), is an outlier because the strong inductive effects of *p*-OCH$_3$ (F = 0.29) cause the withdrawal of σ-bond electrons which counters the expected cathodic shift in redox potential. Not considering the methoxy group, the Hammett plot suggests that a change in σ of at least 0.5 is required to observe significant changes in the redox potential. Interestingly, a 60 mV positive shift was observed when the *tert*-butyl groups were removed from the bipyridine in Pt(^{H}ap)(bpy) (**5**). This result is significant because it suggests that the electron-donating character of the *tert*-butyl groups (σ_p = –0.20) is strong enough to be felt across the metal bridge at the amidophenolate ligand (where the oxidation takes place), and when removed, it becomes more difficult to oxidize the amidophenolate ligand. Although reversible, the potential of the first oxidation is only mildly influenced by ligand functionalization, if at all. This limits the ability to tune the thermodynamic properties of HAT by ligand functional group modification. Comparatively, in the palladium derivative, Pd(^{H}ap)(^{tBu}bpy), the first and second oxidation are shifted negatively by 70 and 100 mV, respectively, compared to the platinum analog.

The amidophenolate ligand is easier to oxidize when bound to the palladium metal center which could be a result of increased electron density at the amidophenolate ligand in this system.

Given the aim of designing viable HAT reagents, it was necessary to investigate the acid-base properties of the complexes. As illustrated in the synthesis, the original neutral complexes, $M(^Rap)(^Xbpy)$ (**1–6**), could be treated with stoichiometric quantities of triflic acid under air-free conditions to generate the air-stable protonated species: $[M(^RapH)(^Xbpy)]^{1+}$ (**1a–6a**). Similarly, the addition of the strong base 1,8-diazabicyclo[5.4.0]undec-7-ene (DBU; $pK_a(CH_3CN) = 24.34$)[48] to an CH_3CN solution of $[M(^RapH)(^Xbpy)]^{1+}$ resulted in an immediate color change from yellow-orange to dark green, signaling the formation of the neutral complex. The unique spectroscopic features of each complex made it possible to monitor the acid/base equilibrium titration (Equation 3.5) of the protonated complexes, $[M(^RapH)(^Xbpy)]^{1+}$, with the appropriate base using electronic absorption spectroscopy.

$$[M(^RapH)(^Xbpy)]^+ + B \rightleftharpoons M(^Rap)(^Xbpy) + HB^+ \qquad (3.5)$$
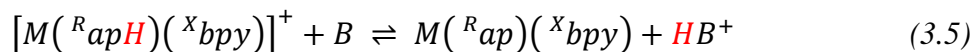
From the absorption data, mass balance was used to determine the equilibrium concentrations of $[M(^RapH)(^Xbpy)]^{1+}$, $M(^Rap)(^Xbpy)$, base (B), and conjugate acid (BH^+). These concentrations were then used to determine the equilibrium constant, K_{eq}, using equations previously reported by our group and originally outlined by Meyer and coworkers.[23,45] The equilibrium constant, K_{eq}, is the slope of the observed trendline from the plot of $[B]_t$ vs. $([M]t/[MH^+]_t)[BH^+]_t$ (Figures 3.8 and 3.9). The K_{eq} and pK_a for the conjugate acid of the base were used in Equation 3.6 to determine the pK_a of the N–H bond in $[M(^RapH)(^Xbpy)]^{1+}$.

$$pK_a\left([M(^RapH)(^Ybpy)]^+\right) = pK_a(BH^+) - log(K_{eq}) \qquad (3.6)$$

It was expected that modification of the amine phenyl ring with functional groups of different electronic properties, would lead to changes in the pK_a value of each complex. However,

$[Pt(^Hap\mathbf{H})(^{tBu}bpy)]^+$, $[Pt(^{Me_2}ap\mathbf{H})(^{tBu}bpy)]^+$, $[Pt(^{OMe}ap\mathbf{H})(^{tBu}bpy)]^+$ had nearly identical pK_a values around 18.6. Table 3.6 shows measured pKa values for **1a–5a** and the Hammett substituent constants for the various substituents investigated. [49,50]

Table 3.6. pK_a values of $[M(^Rap\mathbf{H})(^Xbpy)]^{1+}$ cations and Hammett constants for the amidophenolate substituents investigated.

Complex	Substituent	pK_a	Hammett Constant (σ)
$Pt(^{CF_3}ap\mathbf{H})(^{tBu}bpy)$	para-CF_3	16.8	0.54
$Pt(^{OMe}ap\mathbf{H})(^{tBu}bpy)$	para-OCH_3	18.6	−0.27
$Pt(^{Me_2}ap\mathbf{H})(^{tBu}bpy)$	meta(3,5)-CH_3	18.8	−0.14
$Pt(^Hap\mathbf{H})(^{tBu}bpy)$	para-H	18.5	0
$Pt(^Hap\mathbf{H})(bpy)$	para-H	17.8	0
--	para-*tert*-butyl	--	−0.20

A classic example of the Hammett constant theory in practice is the study of substituted benzoic acid and the impact of the substituting groups on its molecular acidity. The results from those studies show that the change in activation free energy is proportional to the total Gibbs free energy change in the equilibrium and that a linear relationship exists between the pK_a value measured and the substituent constant (σ).[51] Based on existing Hammett constant data, electron-withdrawing groups, which have larger (more positive) σ values, increase acid strength and result in decreased (more acidic) pK_a values. Conversely, electron-donating groups, which have smaller (more negative) σ values, decrease acid strength and result in higher (more basic) pK_a values.[52] For the 3,5-dimethyl substituent (R = Me_2), $\sigma_m = -0.14$ compared to a value of 0 for R = H. This suggest that $[Pt(^{Me_2}ap\mathbf{H})(^{tBu}bpy)]^{1+}$ should be mildly more basic than the unfunctionalized complex, $[Pt(^Hap\mathbf{H})(^{tBu}bpy)]^{1+}$. The difference in pK_a values may be within error of each other and therefore not observed experimentally. On the other hand, a methoxy functional groups is known to be more electron donating than a methyl, with $\sigma_p = -0.27$. This should increase the electron density in the

phenyl ring, near the N–H bond, and increase basicity, but a significant difference was not observed between $[Pt(^{OMe}apH)(^{tBu}bpy)]^{1+}$ and $[Pt(^{H}apH)(^{tBu}bpy)]^{1+}$. This result is reasonable considering the ΔpK_a for benzoic acid vs. 4-methoxybenzoic acid is equal to –0.28 which lies close to the experimental error of the values reported herein.[51] As suggested for the electrochemical data, the strong inductive effects of p-OCH$_3$ could counter the expected increase in basicity. The –CF$_3$ derivative was the only system that showed a change in pK_a. The CF$_3$ functional group is electron-withdrawing, with $\sigma_p = 0.54$, and should decrease the electron density near the protic bond making it more acidic (decrease pK_a). As expected, the pK_a value measured for $[Pt(^{CF_3}apH)(^{tBu}bpy)]^{1+}$ was 16.6. Despite the changed observed for $[Pt(^{CF_3}apH)(^{tBu}bpy)]^{1+}$, the functional groups investigated in this series do not significantly influence the thermodynamic properties of the protic bond in this particular metal complex, which can be observed in the pK_a versus Hammett constant plot (Figure 3.13).
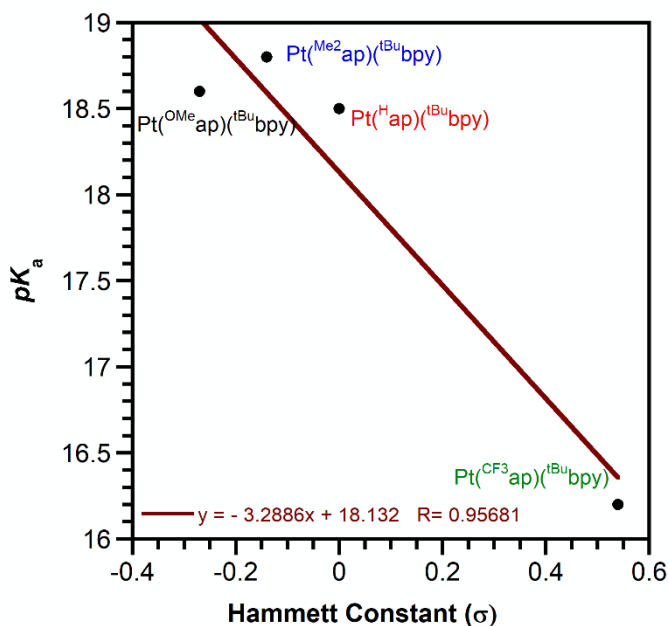
Figure 3.13. pK_a versus the Hammett constant for complexes **1–4**.

However, the electrochemical data had shown that removal of the tert-butyl groups on the bipyridine could affect the redox properties of the amidophenolate ligand. For that reason, the pK_a

of [Pt(^{H}ap**H**)(bpy)]$^+$ was measured to investigate similar effects on the N–H bond pK_a. [Pt(^{H}ap**H**)(bpy)]$^{1+}$ had a pK_a of 17.8 and while the difference from [Pt(^{H}ap**H**)(^{tBu}bpy)]$^+$ is still small (ΔpK_a = 1.7) it was more significant than anything observed by changing the amidophenolate functional groups. This result brought attention to the role of the bipyridine ligand and its substituents. It may be necessary to consider the Hammett constants of a tert-butyl group (σ_p = – 0.20 and R = –0.18) and investigate how these properties can be used to subtly tune the properties of the neighboring ligand.

The measured pK_a value and redox potential (E°′) required to oxidize the ligand were used with Hess's Law to determine the bond dissociation free energy (BDFE). The N–H BDFE values (Table 3.5) were similar for all the complexes reported on account of the similar redox potentials (E°′$_2$) and pK_a values. The N–H BDFE values range from 67.7–69.2 kcal/mol and are slightly higher than the BDFE of TEMPO-H which is 66.5 kcal mol^{-1} in acetonitrile.[53] Treatment of [Pt(^{H}ap**H**)(^{tBu}bpy)]$^{1+}$ (**4a**) with one equivalent of TEMPO$^•$ resulted in no reaction, confirming that the BDFE of the Pt complexes is higher than 66.5 kcal mol^{-1} (TEMPO-H). To test for HAT reactivity, reactions with galvinoxyl$^•$ (galvinol BDFE (C$_6$H$_6$) = 74.0 kcal mol^{-1}) were carried out. Based on the calculated N–H BDFE values, the [Pt(^{R}ap**H**)(^{X}bpy)]$^{1+}$ complexes (**1a–5a**) should react with galvinoxyl$^•$ to generate the one-electron oxidized species [Pt(^{R}ap)(^{X}isq$^•$)]$^{1+}$ and galvinol. The addition of 1 equivalent of galvinoxyl$^•$ to a solution of [Pt(^{H}ap**H**)(^{H}bpy)]$^{1+}$, [Pt(^{H}ap**H**)(^{tBu}bpy)]$^{1+}$, or [Pt(^{OMe}ap**H**)(^{tBu}bpy)]$^{1+}$ resulted on a progressive color change from yellow-green to dark red. After 24 hours, a magenta-colored solid and yellow oil were isolated from the reaction. The yellow oil, putative galvinol, was diamagnetic and the ^{1}H NMR spectrum displayed 4 signals in the aromatic region from 6.88–7.80 ppm integrating to the total of 5 protons expected, a small broad singlet at 5.19 ppm corresponding to the –OH, and 3 singlets in the alkyl

region at 1.55 (9H), 1.48 (9H), and 1.35 (18H) ppm, corresponding to the galvinol *tert*-butyl groups. The magenta solids were similar in color to the radical iminosemiquinonate complex generated by chemical oxidation and predicted to be the $[Pt(^Risq^\bullet)(^Xbpy)]^{1+}$ complexes. The absorption spectra of the putative $[Pt(^Hisq^\bullet)(bpy)]^{1+}$ complexes (Figure 3.10) matched the spectra of the iminosemiquinone complexes made by chemical oxidation (Figure 3.6, *bottom center*), supporting the notion that $[Pt(^Hisq^\bullet)(bpy)]^{1+}$ is one of the HAT reaction products. The EPR spectra of each HAT reaction product also matched the spectra of the iminosemiquinonate complex (Figure 3.11), corroborating the identity of the reaction products as $[Pt(^Risq^\bullet)(^Xbpy)]^{1+}$.

Hydrogen-atom transfer to galvinoxyl is consistent with a BDFE < 74.0 kcal mol^{-1} for the complexes reported herein. The BDFE values determined fall in the middle range of what has been typically observed for transition metal HAT reagents but higher than the nickel-based tridentate [SN(H)S] pincer ligand complexes ([SN(H)S]Ni(PR$_3$) (R = Cy, Ph) previously reported by our group.[20,53] These results indicate that control over BDFE values and subsequent thermodynamics of HAT can be modulated by the calculated selection of the redox-active ligands. However, functional groups must be meticulously selected, and Hammett constants considered to promote significant changes in electrochemical and acid-base properties. It is also crucial to note that investigations currently underway in our lab suggest that the thermodynamics of a ligand-based HAT reaction can also be tuned by the identity of the metal ion in the complex.

3.4 Conclusions

The work described herein presents a synthetic approach to generate donor-acceptor complexes with a protonated, redox-active aminophenolate ligand. The protonated cationic complexes $[Pt(^RapH)(^Xbpy)]^{1+}$ (**1a–5a**) were characterized, and reactivity studies were carried out to confirm that the $[^RapH]^{1-}$ ligand framework can act as a redox, proton, and hydrogen atom

noninnocent ligand. The electrochemical data elucidated the mild influence the different functional groups had on the redox potential for ligand oxidation. The pK_a of the N–H bond was measured by spectrophotometric titration for all of the platinum derivatives and found to range from 16–18 with the largest difference observed for [Pt(^{H}ap**H**)(bpy)]$^{1+}$ and [Pt(^{CF_3}ap**H**)(^{tBu}bpy)]$^{1+}$. The N–H BDFE values determined using Hess's Law were similar for all the complexes reported on account of the similar redox potentials and pK_a values. The calculated N–H BDFE agreed with preliminary HAT reactivity studies which exhibited no reaction with TEMPO$^\bullet$ and successful HAT to galvinoxyl$^\bullet$, providing a bracket of 74.0 kcal mol^{-1} > N–H BDFE > 66.5 kcal mol^{-1}. In summary, these results support previous studies in indicating that control over BDFE values and the thermodynamics of ligand-based HAT can be modulated through strategic selection of the redox-active ligands and metal center. Most importantly, they also demonstrate that subsequent functionalization of the H$^\bullet$ noninnocent ligand may not significantly impact the electronics properties that directly influence the HAT thermodynamics.

3.5 Experimental

General Considerations

All manipulations were carried out using standard vacuum-line, Schlenk-line, and glovebox techniques unless otherwise noted. Hydrocarbon and ethereal solvents were sparged with argon before being deoxygenated and dried by serial passage through Q5 and activated alumina columns. Halogenated solvents were sparged with argon and dried by passage through two activated alumina columns. Acetonitrile-d_3(CD$_3$CN) and benzene-d_6(C$_6$D$_6$) were dried over calcium hydride, filtered, degassed by freeze-pump-thaw method, and stored over molecular sieves prior to use. 4-aminopyridine and bipyridine were used as received. 2,4,6-trimethylpyridine was degassed by freeze-pump-thaw method prior to use. The ligand, 2,4-di-tert-butyl-6-(phenylamino)phenol, its

substituted derivatives,[42,43] and the metal starting materials $MCl_2(^Xbpy)_2$ (M = Pt, Pd; X = H, tBu)[40,41] were prepared as previously described in the literature. Ferrocene (Acros) was purified by sublimation, and tetrabutylammonium hexafluorophosphate (Acros) was recrystallized from ethanol and dried under vacuum.[54]

Spectroscopic Methods

Elemental analyses were conducted on a PerkinElmer 2400 Series II CHNS elemental analyzer. NMR spectra were collected on a Bruker DRX 400 MHz spectrometer in dry, degassed CD_3CN or C_6D_6. ^{1}H NMR spectra were referenced to tetramethylsilane using the residual proteo impurities of the solvent (1.94 ppm for CD_3CN, 7.16 ppm for C_6D_6). Chemical shifts are reported using the standard δ notation in parts per million. Electronic absorption spectra were recorded with a Jasco V-670 absorption spectrometer or a Cary 60 UV–vis spectrometer equipped with fiber-optic cables. UV–vis spectra were recorded for samples dissolved in dry, degassed acetonitrile (CH_3CN) and contained in 10 mm quartz cells. Electrospray ionization mass spectrometry (ESI-MS) data were collected on samples dissolved in methanol using a Waters LCT Premier mass spectrometer. Electron paramagnetic resonance (EPR) spectra were collected on a Bruker EMX X-band spectrometer equipped with an ER041XG microwave bridge.

Electrochemical Methods

Electrochemical data were collected on a Gamry Series G 300 potentiostat/galvanostat/ZRA (Gamry Instruments, Warminster, PA) using a standard three-electrode configuration comprising a 3.0 mm glassy carbon working electrode, a platinum wire auxiliary electrode, and a silver wire pseudoreference electrode. Electrochemical experiments were performed at 25 °C in a glovebox under an atmosphere of N_2. Electrochemical samples were 1.0 mM analyte solutions in CH_3CN

containing 0.1 M [Bu$_4$N][PF$_6$] as the supporting electrolyte. All potentials were referenced to the [Cp$_2$Fe]$^{+/0}$ couple using ferrocene ($E°' = -0.59$ V) as an internal standard.[55]

pK_a Determinations

The pK_a values were determined by spectrophotometric titration following published methods.[45] In a typical experiment, an CH$_3$CN stock solutions of the [Pt(^{R}apH)(^{X}bpy)]$^{1+}$ complex (~ 0.35–0.50 mM) and either 0.15 M 4-aminopyrdine or 0.4 M 2,4,6-collidine were prepared inside a nitrogen-filled glovebox. Aliquots (2 mL) of the metal complex were removed from the stock solution, the appropriate equivalents of base (from base stock solution) were added using a volumetric syringe, and solution was diluted to a final volume of 5.0 mL using CH$_3$CN to give concentrations around 0.15 mM. The sample solution was transferred to a quartz cuvette and sealed to maintain an air-free environment. Spectral changes for each sample (equivalent of base added) were recorded with a Jasco 670 UV–vis spectrometer.

Crystallographic Methods

X-ray diffraction data were collected at low temperature on a single crystal covered in Paratone and mounted on a glass fiber. Data were acquired using a Bruker SMART APEX II diffractometer equipped with a CCD detector using Mo Kα radiation ($\lambda = 0.71073$ Å), which was wavelength-selected with a single-crystal graphite monochromator. The *SMART* program package was used for determination of the unit-cell parameters and for data collection. The raw frame data were processed using *SAINT* and *SADABS* to yield the reflection data file. Subsequent calculations were carried out with *SHELXTL*. The structures were solved by direct methods and refined on F^2 by full-matrix least-squares techniques. Analytical scattering factors for neutral atoms were used throughout the analyses. Hydrogen atoms were generated in calculated positions and refined using a riding model. ORTEP diagrams were generated using *ORTEP-3 for Windows*.

Pt(^{H}ap)(^{tBu}bpy). A suspension of 14 mg of KH (0.34 mmol, 2 equiv) in THF was added dropwise to a solution containing 51 mg of 2,4-di-tert-butyl-6-(phenylamino)phenol (0.170 mmol, 1 equiv) in THF and stirred for one hour to deprotonate the ligand. The deprotonated ligand solution was added slowly to a suspension of Pt(^{tBu}bpy)Cl$_2$ (91 mg, 0.170 mmol, 1 equiv) in THF and was refluxed for 10 hours under N$_2$. The solution was cooled to ambient temperature and taken to dryness under reduced pressure. The green-blue residue was dissolved in diethyl ether and filtered to collect insoluble byproducts. The ethyl ether filtrate was taken to dryness, washed with cold pentane, and dried to obtain the product as dark green solid (58%). ^{1}H NMR (400 MHz, Benzene-d_6) δ 10.17 (d, J = 6.3 Hz, 1H), 7.84 – 7.77 (m, 2H), 7.64 (d, J = 6.5 Hz, 1H), 7.39 (t, J = 7.7 Hz, 2H), 7.19 (d, J = 5.1 Hz, 1H), 7.04 (d, J = 2.2 Hz, 1H), 6.97 (d, J = 2.1 Hz, 1H), 6.67 (dd, J = 6.4, 2.1 Hz, 1H), 6.41 (dd, J = 6.5, 2.2 Hz, 1H), 2.15 (s, 9H), 1.54 (s, 9H), 0.94 (s, 9H), 0.78 (s, 9H).

Pt(^{H}ap)(bpy). This compound was prepared as described above for Pt(^{H}ap)(^{tBu}bpy) except that 110 mg of Pt(bpy)Cl$_2$ (0.260 mmol, 1 equiv) was used at the metal starting material with 78 mg of 2,4-di-tert-butyl-6-(phenylamino)phenol (0.260 mmol, 1 equiv). A dark forest-green solid was obtained in 55% yield. ^{1}H NMR (400 MHz, Benzene-d_6) δ 10.12 (d, J = 5.9 Hz, 1H), 7.71 – 7.64 (m, 2H), 7.50 – 7.40 (m, 1H), 7.33 (t, J = 7.7 Hz, 2H), 7.00 (d, J = 2.2 Hz, 1H), 6.95 (d, J = 2.3 Hz, 1H), 6.80 – 6.70 (m, 1H), 6.61 (t, J = 7.7 Hz, 1H), 6.51 (d, J = 6.3 Hz, 2H), 6.34 (t, J = 6.4 Hz, 1H), 5.97 (t, J = 6.7 Hz, 1H), 2.07 (s, 9H), 1.51 (s, 9H).

Pt(^{CF_3}ap)(^{tBu}bpy). This compound was prepared as described above for Pt(^{H}ap)(^{tBu}bpy) except that 214 mg of 2,4-di-tert-butyl-6-((4-(trifluoromethyl)phenyl)amino)phenol (0.586 mmol, 1 equiv) was treated with 47 mg of KH (1.17 mmol, 2 equiv), and subsequently reacted with 586 mg of Pt(^{tBu}bpy)Cl$_2$ (0.586 mmol, 1 equiv). A dark forest-green solid was obtained in 27% yield. ^{1}H

NMR (400 MHz, Benzene-d_6) δ 10.06 (d, J = 6.2 Hz, 1H), 7.75 (d, J = 8.1 Hz, 2H), 7.53 (dd, J = 13.3, 7.2 Hz, 3H), 7.12 (d, J = 2.2 Hz, 1H), 7.06 (s, 2H), 6.68 (dd, J = 6.3, 2.0 Hz, 1H), 6.38 (dd, J = 6.4, 2.2 Hz, 1H), 2.12 (s, 9H), 1.54 (s, 9H), 0.92 (s, 9H), 0.78 (s, 9H).

Pt(^{Me2}ap)(^{tBu}bpy). To a suspension of 218 mg of Pt(^{tBu}bpy)Cl$_2$ (0.408 mmol, 1 equiv) in acetonitrile was added a CH$_3$CN solution of 133 mg of 2,4-di-tert-butyl-6-((3,5-dimethylphenyl)amino)phenol (0.408 mmol, 1 equiv). The reaction vessel was sealed, brought out of the glovebox, and placed under N$_2$ on a Schlenk line. A methanol solution of 0.5 M Na[OCH$_3$] (1.6 mL, 0.816 mmol, 2 equiv) was added with a syringe and the reaction mixture was refluxed overnight. The solution was cooled to ambient temperature and the solvent was removed under reduced pressure leaving a green-blue residue. The vessel was opened to air and the green-blue residue was taken into ether and filtered to remove insoluble byproducts. The ethyl ether filtrate was taken to dryness to obtain a dark green powder. The solid was dissolved in pentane and chilled to –35 °C. The precipitate solid was collected by filtration, washed with cold pentane and dried under reduced pressure to obtain the desired product as a dark green solid in 49% yield. ^{1}H NMR (400 MHz, Benzene-d_6) δ 10.19 (d, J = 6.3 Hz, 1H), 7.81 (d, J = 6.5 Hz, 1H), 7.47 (s, 2H), 7.18 (s, 0H), 7.03 (s, 2H), 6.90 (s, 1H), 6.66 (dd, J = 6.3, 2.1 Hz, 1H), 6.47 (dd, J = 6.5, 2.2 Hz, 1H), 2.23 (s, 6H), 2.16 (s, 9H), 1.55 (s, 9H), 0.94 (s, 9H), 0.79 (s, 9H).

Pt(^{OMe}ap)(^{tBu}bpy). This compound was prepared as described above for Pt(^{Me2}ap)(^{tBu}bpy) except that 306 mg of 2,4-di-tert-butyl-6-((4-methoxyphenyl)amino)phenol (0.936 mmol, 1 equiv) was used with 500 mg of Pt(^{tBu}bpy)Cl$_2$ (0.936 mmol, 1 equiv). A dark forest-green solid was obtained in 27% yield. ^{1}H NMR (400 MHz, Benzene-d_6) δ 10.19 (d, J = 6.2 Hz, 1H), 7.84 (d, J = 6.4 Hz, 1H), 7.71 – 7.63 (m, 2H), 7.19 (d, J = 1.3 Hz, 2H), 7.04 (d, J = 2.2 Hz, 1H), 7.01 (d, J = 2.2 Hz,

1H), 6.99 (d, J = 2.2 Hz, 1H), 6.92 (d, J = 2.2 Hz, 1H), 6.67 (dd, J = 6.4, 2.0 Hz, 1H), 6.48 (dd, J = 6.4, 2.2 Hz, 1H), 3.37 (s, 3H), 2.15 (s, 9H), 1.57 (s, 9H), 0.95 (s, 9H), 0.78 (s, 9H).

Pd(ap)(tBubpy). A suspension of 57 mg of KH (1.43 mmol, 2 equiv) in THF was added dropwise to 212 mg of 2,4-di-tert-butyl-6-(phenylamino)phenol (0.713 mmol, 1 equiv) in THF and stirred for one hour. The deprotonated ligand solution was added slowly to a suspension of 318 mg of Pd(tBubpy)Cl$_2$ (0.713 mmol, 1 equiv) in CH$_3$CN. The reaction mixture was stirred in the glovebox for 10 hours at ambient temperature. The solvent was removed under reduced pressure leaving a blue-green residue. The residue was triturated with pentane and filtered to obtain a dark blue solid. The solids were dissolved in diethyl ether and filtered to collect insoluble KCl and unreacted metal starting material. The ethyl ether filtrate was taken to dryness, triturated with pentane three times, and dried to obtain a dark blue powder in 58% yield. ^{1}H NMR (400 MHz, Benzene-d$_6$) δ 9.56 (d, J = 6.0 Hz, 1H), 7.84 (d, J = 7.6 Hz, 2H), 7.36 (t, J = 7.6 Hz, 2H), 7.28 – 7.17 (m, 2H), 7.04 (s, 1H), 6.93 (s, 1H), 6.75 (dd, J = 6.0, 1.9 Hz, 1H), 6.52 (dd, J = 6.2, 2.1 Hz, 1H), 2.13 (s, 9H), 1.54 (s, 9H), 0.93 (s, 9H), 0.77 (s, 9H).

Protonated Cationic Complexes

[Pt(HapH)(tBubpy)]CF$_3$SO$_3$. A solution containing 87 mg of Pt(ap)(tBubpy) (0.114 mmol, 1equiv) in THF and a 0.5 M solution of triflic acid in diethyl ether were both frozen in a cold well using liquid nitrogen (LN$_2$). The frozen solutions were partially thawed and 0.23 mL of triflic acid solution (0.114 mmol, 1 equiv) was added dropwise to the Pt(ap)(tBubpy) solution. As the triflic acid was added, the solution began to change from a dark green-blue to a bright orange. The reaction mixture was stirred in the glovebox for 1 hour as it warmed to ambient temperature. The solvent was removed under reduced pressure leaving an orange residue. The orange residue was taken into a 2:1 pentane/ether solution and taken to dryness again. The residue was triturated with

pentane until an orange power was obtained. The orange solid was washed with pentane to obtain the product in quantitative yields. X-ray quality crystals were obtained by dissolving in THF, layering with ether, and cooling to –35 °C or by slow evaporation of a concentrated solution of the product in benzene. ^{1}H NMR (400 MHz, Benzene-d_6) δ 10.42 (s, 1H), 8.95 (t, J = 5.8 Hz, 2H), 8.31 – 8.24 (m, 2H), 8.14 (s, 1H), 8.06 (s, 1H), 7.39 (d, J = 2.2 Hz, 1H), 7.34 (d, J = 2.3 Hz, 1H), 7.10 (dd, J = 6.2, 2.1 Hz, 1H), 6.98 (dd, J = 8.5, 7.4 Hz, 2H), 6.82 (dd, J = 6.1, 2.0 Hz, 1H), 6.75 – 6.65 (m, 1H), 1.88 (s, 9H), 1.30 (s, 9H), 1.14 (s, 9H), 1.07 (s, 9H).

[Pt(apH)(bpy)]CF₃SO₃. Complex was prepared according to the general procedure described for Pt(^{H}apH)(^{tBu}bpy). Anal. calcd. (Found) for $C_{30}H_{34}N_3OPtCF_3SO_3$ (%): C, 46.73 (46.58); H, 4.30 (4.32); N, 5.27 (5.26). ^{1}H NMR (400 MHz, Benzene-d_6) δ 10.10 (s, 1H), 8.77 – 8.67 (m, 2H), 8.21 (d, J = 8.2 Hz, 1H), 8.16 – 8.10 (m, 3H), 7.64 (d, J = 7.8 Hz, 1H), 7.43 (d, J = 2.2 Hz, 1H), 7.35 (t, J = 1.9 Hz, 2H), 6.95 (dtd, J = 21.6, 7.7, 1.6 Hz, 3H), 6.77 – 6.64 (m, 2H), 6.53 (ddd, J = 7.4, 5.8, 1.3 Hz, 1H), 1.76 (s, 9H), 1.28 (s, 9H).

[Pt(^{CF3}apH)(^{tBu}bpy)]CF₃SO₃. Complex was prepared according to the general procedure described for Pt(^{H}apH)(^{tBu}bpy).

[Pt(^{Me2}apH)(^{tBu}bpy)]CF₃SO₃. Complex was prepared according to the general procedure described for Pt(^{H}apH)(^{tBu}bpy). Anal. calcd. (Found) for $C_{40}H_{54}N_3OPtCF_3SO_3$ + Benzene (C_6H_6) (%): C, 55.61 (55.74); H, 5.96 (5.87); N, 4.14 (4.14). ^{1}H NMR (500 MHz, Benzene-d_6) δ 10.36 (s, 1H), 9.07 (d, J = 6.2 Hz, 1H), 8.98 (d, J = 6.0 Hz, 1H), 8.10 (s, 2H), 8.00 (d, J = 2.1 Hz, 1H), 7.92 (d, J = 2.2 Hz, 1H), 7.50 (d, J = 2.2 Hz, 1H), 7.35 (d, J = 2.3 Hz, 1H), 6.78 (dd, J = 6.0, 2.0 Hz, 1H), 6.46 (s, 1H), 2.01 (s, 6H), 1.91 (s, 9H), 1.30 (s, 9H), 1.10 (s, 9H), 1.04 (s, 9H).

[Pt(^{OMe}apH)(^{tBu}bpy)]CF₃SO₃. Complex was prepared according to the general procedure described for Pt(^{H}apH)(^{tBu}bpy). The yellow-orange solid was obtained in 58% yield. ^{1}H NMR (400

MHz, Benzene-d_6) δ 10.35 (s, 1H), 8.98 (d, J = 6.1 Hz, 2H), 8.28 – 8.21 (m, 2H), 8.16 (d, J = 2.0

Hz, 1H), 8.10 (d, J = 2.1 Hz, 1H), 7.44 (d, J = 2.2 Hz, 1H), 7.35 (d, J = 2.2 Hz, 1H), 6.83 (dd, J =

6.2, 2.0 Hz, 1H), 6.65 – 6.58 (m, 2H), 3.02 (s, 3H), 1.89 (s, 9H), 1.34 (s, 9H), 1.15 (s, 9H), 1.09

(s, 9H).

[Pd(^HapH)(^{tBu}bpy)]CF₃SO₃. Complex was prepared according to the general procedure described

for Pt(^HapH)(^{tBu}bpy). ¹H NMR (400 MHz, Benzene-d₆) δ 9.74 (s, 1H), 8.72 (d, J = 5.9 Hz, 1H),

8.49 (d, J = 6.0 Hz, 1H), 8.37 (d, J = 7.9 Hz, 2H), 7.83 (d, J = 15.4 Hz, 2H), 7.42 – 7.33 (m, 2H),

7.03 (t, J = 7.9 Hz, 3H), 6.96 (s, 2H), 6.77 – 6.64 (m, 2H), 1.86 (s, 9H), 1.33 (s, 9H), 1.08 (d, J =

5.2 Hz, 18H).

Synthesis of [Pt(^Risq•)(^Xbpy)][PF₆] (R = H, X = H; R = H, X = tBu; R = OMe, X = tBu). Solid

AgPF₆ (1 equiv) was added to solutions of the neutral complexes (Pt(^Rap)(^Xbpy)) in CH₃CN and

stirred in the glovebox at ambient temperature overnight. The reaction solution was filtered over

celite to remove Ag(0). The solvent was removed under reduced pressure leaving a dark magenta

residue. For all complexes, the residue was triturated with pentane to obtain the one-electron

oxidized complexes of the form, [Pt(^Risq•)(^Xbpy)][PF₆] as paramagnetic, magenta-colored solids

in quantitative yields.

3.6 References

(1)   Deno, N. C.; Peterson, H. J.; Saines, G. S. *Chem. Rev.* **1960**, *60*, 7–14.

(2)   Zhu, X.-Q.; Zhang, M.-T.; Yu, A.; Wang, C.-H.; Cheng, J.-P. *J. Am. Chem. Soc.* **2008**,
       130, 2501–2516.

(3)   Ilic, S.; Kadel, U. P.; Basdogan, Y.; Keith, J. A.; Glusac, K. D. *J. Am. Chem. Soc.* **2018**,
       140, 4569–4579.

(4)   Zhao, H.; Li, Y.; Zhu, X.-Q. *ACS Omega* **2018**, *3*, 13598–13608.

(5)   Lim, C.-H.; Ilic, S.; Alherz, A.; Worrell, B. T.; Bacon, S. S.; Hynes, J. T.; Glusac, K. D.; Musgrave, C. B. *J. Am. Chem. Soc.* **2019**, *141*, 272–280.

(6)   Hu, Y.; Norton, J. R. *J. Am. Chem. Soc.* **2014**, *136*, 5938–5948.

(7)   Wiedner, E. S.; Chambers, M. B.; Pitman, C. L.; Bullock, R. M.; Miller, A. J. M.; Appel, A. M. *Chem. Rev.* **2016**, *116*, 8655–8692.

(8)   Waldie, K. M.; Ostericher, A. L.; Reineke, M. H.; Sasayama, A. F.; Kubiak, C. P. *ACS C* **2018**, *8*, 1313–1324.

(9)   Boyd, E. A.; Lionetti, D.; Henke, W. C.; Day, V. W.; Blakemore, J. D. *Inorg. Chem.* **2018**, *58*, 3606–3615.

(10)   Thompson, E. J.; Berben, L. A. *Angew. Chemie - Int. Ed.* **2015**, *54* (40), 11642–11646.

(11)   Luo, G.-G.; Zhang, H.-L.; Tao, Y.-W.; Wu, Q.-Y.; Tian, D.; Zhang, Q. *Inorg. Chem. Front.* **2019**, *6*, 343–354.

(12)   Gupta, R.; Macbeth, C. E.; Young, V. G.; Borovik, A. S. *J. Am. Chem. Soc.* **2002**, *124* (7), 1136–1137.

(13)   Waidmann, C. R.; Zhou, X.; Tsai, E. A.; Kaminsky, W.; Hrovat, D. A.; Borden, W. T.; Mayer, J. M. *J. Am. Chem. Soc.* **2009**, *131*, 4729–4743.

(14)   Steffensmeier, E.; Swann, M. T.; Nicholas, K. M. *Inorg. Chem.* **2019**, *58*, 844–854.

(15)   Soper, J. D.; Mayer, J. M. *J. Am. Chem. Soc.* **2003**, *125*, 12217–12229.

(16)   Roth, J. P.; Lovell, S.; Mayer, J. M. *J. Am. Chem. Soc.* **2000**, *122*, 5486–5498.

(17)   Wu, A.; Masland, J.; Swartz, R. D.; Kaminsky, W.; Mayer, J. M. *Inorg. Chem.* **2007**, *46*, 11190–11201.

(18)   Britt, R. D.; Sayler, R. I.; Berben, L. A.; Thompson, E. J.; Sherbow, T. J.; Arnold, A.

Chem. - A Eur. J. **2018**, *25* (2), 454–458.

(19)　Mcloughlin, E. A.; Waldie, K. M.; Ramakrishnan, S.; Waymouth, R. M. *J. Am. Chem. Soc.* **2018**, *140*, 13233–13241.

(20)　Rosenkoetter, K. E.; Wojnar, M. K.; Charette, B. J.; Ziller, J. W.; Heyduk, A. F. *Inorg. Chem.* **2018**, *57*, 9728–9737.

(21)　Matsumoto, T.; Chang, H.-C.; Wakizaka, M.; Ueno, S.; Kobayashi, A.; Nakayama, A.; Taketsugu, T.; Kato, M. *J. Am. Chem. Soc* **2013**, *135*.

(22)　Nadif, S. S.; O'Reilly, M. E.; Ghiviriga, I.; Abboud, K. A.; Veige, A. S. *Angew. Chemie - Int. Ed.* **2015**, *54* (50), 15138–15142.

(23)　Rosenkoetter, K. E. Synthesis and Reactivity of Transition Metal Complexes Bearing the Tridentate Bis(2-mercapto-p-tolyl)amine ([SNS]H3) Ligand, 2017.

(24)　Bryant, J. R.; Mayer, J. M. *J. Am. Chem. Soc.* **2003**, *125*, 10351–10361.

(25)　Roth, J. P.; Mayer, J. M. *Inorg. Chem.* **1999**, *38*, 2760–2761.

(26)　Mayer, J. M.; Mader, E. A.; Roth, J. P.; Bryant, J. R.; Matsuo, T.; Dehestani, A.; Bales, B. C.; Watson, E. J.; Osako, T.; Valliant-Saunders, K.; Lam, W. H.; Hrovat, D. A.; Borden, W. T.; Davidson, E. R. *J. Mol. Catal. A Chem.* **2006**, *251*, 24–33.

(27)　Manner, V. W.; Mayer, J. M. *J. Am. Chem. Soc.* **2009**, *31*, 9874–9875.

(28)　Mayer, J. M. *Acc. Chem. Res.* **2011**, *44* (1), 36–44.

(29)　Chirik, P. J. *Inorg. Chem.* **2011**, *50*, 9737–9740.

(30)　Pierpont, C. G.; Buchanan, R. M. *Coord. Chem. Rev.* **1981**, *38*, 45–87.

(31)　Heyduk, A. F.; Zarkesh, R. A.; Nguyen, A. I. *Inorg. Chem.* **2011**, *50*, 9849–9863.

(32)　Ward, M. D.; Mccleverty, J. A. *J. Chem. Soc. Dalt. Trans.* **2002**, 275–288.

(33)　Berben, L. A.; De Bruin, B.; Heyduk, A. F. *Chem. Commun* **2015**, *51*, 1553–1554.

(34)   Borovik, A. S. *Acc. Chem. Res.* **2005**, *38*, 54–61.

(35)   Cook, S. A.; Borovik, A. S. *Acc. Chem. Res* **2015**, *48*, 2407–2414.

(36)   Cameron, L. A.; Ziller, J. W.; Heyduk, A. F. *Chem. Sci.* **2016**, *7*, 1807–1814.

(37)   Kramer, W. W.; Cameron, L. A.; Zarkesh, R. A.; Ziller, J. W.; Heyduk, A. F. *Inorg. Chem.* **2014**, *53*, 8825–8837.

(38)   Sun, X.; Chun, H.; Hildenbrand, K.; Bothe, E.; Weyhermu, T.; Neese, F.; Wieghardt, K. *Inorg. Chem.* **2002**, *41* (16), 4295–4303.

(39)   Chaudhuri, P.; Verani, C. N.; Bill, E.; Bothe, E.; Wieghardt, K. *J. Am. Chem. Soc.* **2001**, *123* (3), 2213–2223.

(40)   Fox, S. G.; Gillard, R. D. *Polyhedron* **1988**, *7* (5), 349–352.

(41)   Choi, Y. S.; Moschetta, E. G.; Miller, J. T.; Fasulo, M.; McMurdo, M. J.; Rioux, R. M.; Tilley, T. D. *ACS Catal.* **2011**, *1* (10), 1166–1177.

(42)   Shadyro, O. I.; Sorokin, V. L.; Ksendzova, G. A.; Polozov, G. I.; Nikolaeva, S. N.; Pavlova, N. I.; Savinova, O. V; Boreko, E. I. *Pharm. Chem. J.* **2003**, *37* (8), 399–401.

(43)   Jacquet, J.; Chaumont, P.; Gontard, G.; Orio, M.; Vezin, H.; Blanchard, S.; Desage-El Murr, M.; Fensterbank, L. *Angew. Chemie - Int. Ed.* **2016**, *55*, 10712–10716.

(44)   Kokatam, S.-L.; Chaudhuri, P.; Weyhermüller, T.; Wieghardt, K. *Dalt. Trans.* **2007**, *0*, 373–378.

(45)   Saouma, C. T.; Kaminsky, W.; Mayer, J. M. *J. Am. Chem. Soc.* **2012**, *134*, 7293–7296.

(46)   Conner, K. M.; Arostegui, A. C.; Swanson, D. D.; Brown, S. N. *Inorg. Chem.* **2018**, *57*, 9696–9707.

(47)   Vogler, A.; Kunkely, H. *Comments Inorg. Chem.* **1990**, *9*, 201–220.

(48)   Kaljurand, I.; Kü, A.; Soovä Li, L.; Rodima, T.; Mä, V.; Leito, I.; Koppel, I. A. *J. Org.*

Chem. **2005**, *70* (3), 1019–1028.

(49)   Hansch, C.; Leo, A.; Taft, R. W. *Chem. Rev* **1991**, *91*, 165–195.

(50)   Hammett, L. P. *Chem. Rev.* **1935**, *17*, 125–136.

(51)   Huang, Y.; Liu, L.; Liu, W.; Liu, S.; Liu, S. *J. Phys. Chem. A* **2011**, *115*, 14697–14707.

(52)   Robert, J. D.; Caserio, M. C. *26.6: CORRELATIONS OF STRUCTURE WITH REACTIVITY OF AROMATIC COMPOUNDS*; 2017.

(53)   Warren, J. J.; Tronic, T. A.; Mayer, J. M. *Chem. Rev.* **2010**, *110*, 6961–7001.

(54)   Armarego, W. L. F.; Chai, C. L. L. *Purification of Laboratory Chemicals (5th Edition)*, 5th ed.; Butterworth-Heinemann, 2003.

(55)   Connelly, N. G.; Geiger, W. E. *Chem. Rev.* **1996**, *96*, 877–910.

Chapter 4

Design and Photophysical Characterization of Iridium(III) Coordination Compounds for Studies of Excited-State Proton Transfer

4.1 Introduction

Proton-transfer reactions are ubiquitous in both biological and chemical processes. For example, photosynthetic organisms use molecular chromophores to capture sunlight. The energy absorbed from the sun generates the molecular excited state of the chromophore, which is then used to drive specific electron and proton transfer processes. These processes ultimately result in the storage of energy in the form of chemical bonds. The archaea, *Halobacterium halobium*, is a photosynthetic organism that relies solely on a light-driven protonic circuit, requiring bacteriorhodopsin with a retinal chromophore, to generate usable cellular energy (Figure 4.1).[1]

Figure 4.1. Light-driven protonic circuit of *Halobacterium halobium*. Figure adapted from reference 1.

In this system, the chromophore retinal is attached via a Schiff base to the amino group of a lysine residue. Upon light excitation, the retinal chromophore undergoes isomerization from all-*trans* to a 13-*cis*, 15-*anti* configuration. This change allows the Asp-85 residue to deprotonate the Schiff base followed by its reprotonation by the Asp-96 residue. This causes retinal to isomerize back to the all-trans form, which is then reprotonated by protons in the cytoplasmic surface. The

protonated Asp-85 residue transfers its proton to the Glu-204 residue, which is the proton release site that liberates a proton into the extracellular environment. This cycle perturbs initial proton gradients that are used to drive the formation of ATP by ATP Synthase as shown in Figure 4.1.[2] This system is an example of light being used to trigger a change in the confirmation of a substrate that subsequently drives the transfer of protons for energy production. Alternatively, certain molecules can experience dramatic changes in their acidity (or basicity) as a result of photoexcitation. Upon illumination, these molecules undergo excited-state proton transfer (ESPT) and liberate (or accept) a proton. These types of molecules are known as photoacids (or photobases) and have been used to study the photochemistry of ESPT. These types of molecules have been investigated for applications such as artificial photosynthetic systems, probes for solvent environments, molecular switches, acid-catalyzed and pH-sensitive reactions, catalyst activation, and the killing of multi-drug resistant bacteria.[3–7]

The electronic structure of a molecule controls physical and chemical properties such as charge distribution, geometry and polarity, ionization potential, electron affinity, and chemical reactivity. Photochemical proton transfer reactions occur due to the redistribution of electron density in a molecule upon its transition from the ground state to a singlet or triplet excited state or metastable state.[8] The redistribution of electron density alters the properties of the molecule, which results in a change in the K_a, the acid dissociation constant for proton dissociation of one of its protic functional groups. A well-known example of a molecule that performs ESPT is phenol, which has a ground state pK_a of 10 and excited-state pK_a (pK_a*) of 4.[9] This occurs because photoexcitation alters the electron density on the phenolic hydroxyl group to lie more on the phenol ring. This makes the hydroxyl group more acidic and decreases the pK_a value in the excited state. This means that in the excited state the phenolic proton becomes more acidic and can

thermodynamically dissociate in a near-neutral-pH solution (pH = ~ 7) such as water. Acid or base

strength can be increased by using light excitation to decrease or increase, respectively, the electron

density near the protic bond.[10]
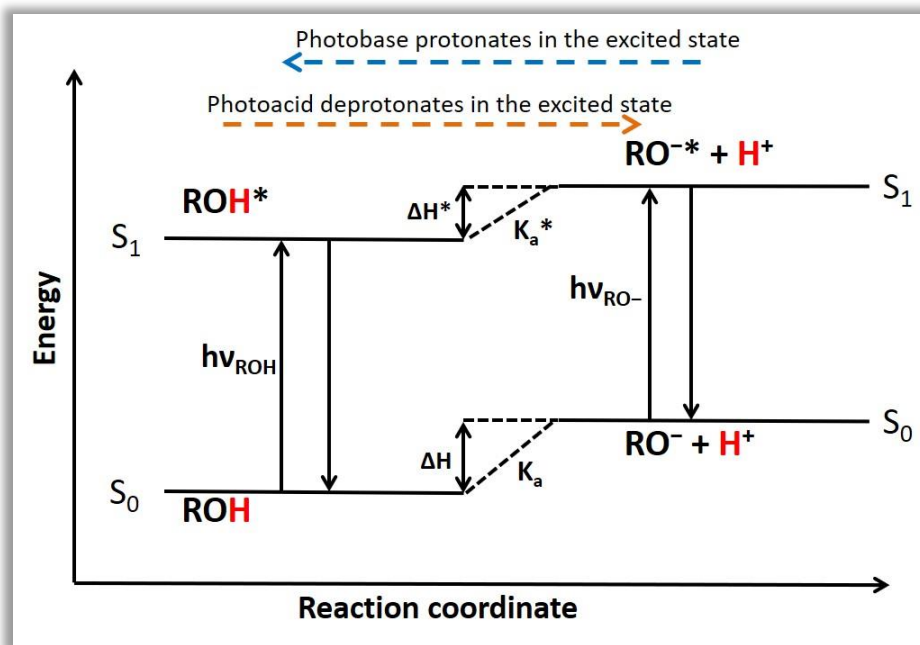
Figure 4.2. Protolytic Förster cycle depicting ESPT from a photoacid (ROH) or photobase (RO⁻).

This type of photoreactivity was first investigated by Förster, who classified the reactivity as ESPT

and developed the well-known Förster cycle (Figure 4.2) to characterize the components and

estimate pK_a^*.[11,12] The relative energies of the acid (ROH) and its conjugate base (RO⁻) are shown

for both the ground state (S_0) and the lowest energy singlet excited state (S_1) in aqueous solution

at pH = 0. Each product (conjugate base and proton) has a higher energy than the reactant

(protonated acid) by $\Delta H°$ (i.e. enthalpy of deprotonation) with respect to the acid because the

dissociation constants, K_a and K_a^*, are < 1 and making the approximation that the change in $\Delta S°$

= 0.[9] This approximation allows one to relate the energy differences of the states with the free

energies for proton transfer, and because dissociation is energetically more favorable in the S_1

state, the $S_0 \rightarrow S_1$ gap is smaller for the conjugate base. The ground state acid and conjugate base can each be converted to their respective excited-states through the absorption of a photon whose energy is equal to $h\nu_{ROH}$ and $h\nu_{RO^-}$, respectively. For simplicity, the energy of the adsorbed photon that promotes the transition into the excited state is illustrated as being equal to the energy of the emission from the excited state to the ground state.[13] However, due to the vibrational levels that are involved in the transitions (omitted from diagram for clarity), on average emitted photons will be lower in energy than the absorbed photons.[8,13] Figure 4.2 illustrates a photoacid (ROH) with $pK_a > pH$ that upon absorption of a photon generates an excited state that at thermal and excited-state-chemical equilibrium deprotonates when $pK_a^* < pH$, and subsequently relaxes back to the ground state from the deprotonated state. The photobase (RO^- in Figure 4.2) with $pK_a < pH$ absorbs a photon and generates an excited state that at thermal and excited-state-chemical equilibrium protonates when $pK_a > pH$, and subsequently relaxes back to the ground state from the protonated state. The most straightforward way to determine if a molecule undergoes ESPT is to monitor the change in the absorption and photoluminescence spectra as a function of pH, and assuming excited-states reach thermal and chemical equilibrium during the excited-state lifetime, calculate the pK_a in each state and determine the ΔpK_a ($\Delta pK_a = pK_a^* - pK_a$). In 1931, Weber reported the first example of ESPT with the organic photoacid 1-naphthylamine-4-sulfonate (NAS).[14,15] The absorption spectrum of NAS was shown to change as a function of pH, but the photoluminescence spectrum did not change until extremely acidic conditions were used. Deprotonation of the emitting molecule in the excited state irrespective of the ground-state species was indicative of photoacidic behavior. Based on the work of Weber, Förster, Weller, Vander Donekt, and Kasha, it is now well established that upon photoexcitation, functional groups such as R-OH become stronger acids, while functional groups such as $R\text{-}CO_2H$ become stronger bases, and that the

magnitude of ΔpK_a is approximately dictated by the dipolar character of the excited state.[16] Today, state-of-the-art photoacids predominately consist of conjugated organic molecules that contain hydroxyl groups such as derivatives of naphthol and hydroxy-pyrene.[17] While organic photoacids are well known, the study of inorganic photoacids is more nascent.

Inorganic coordination compounds that, upon photon absorption, generate intramolecular charge-transfer excited states with large dipolar character have been extensively studied.[18–20] $[Ru^{II}(bpy)_3]^{2+}$, where bpy is 2,2'-bipyridine, is a classic example of these compounds where the thermally-equilibrated excited state, $[Ru(bpy)_3]^{2+*}$, can be directly generated from metal-to-ligand charge-transfer (MLCT) excitation using visible light at approximately 550 nm (2.3 eV). This charge-separated state has localized molecular orbitals that are vacant on the donor sites (Ru $t_{2g}/d\pi$) and filled on the acceptor sites (bpy π^*).[21] This molecule and its synthetic analogs have provided much of the knowledge base on the photophysics and photochemistry of inorganic and organometallic chromophores. When functionalized with an appropriate functional group, $[Ru^{II}(bpy)_3]^{2+}$ is well suited to perform ESPT and act as a photoacid or photobase, due to the large dipolar character it exhibits. In the case of $[Ru^{II}(bpy)_3]^{2+}$, the increase in free energy upon photon absorption can be approximated by the difference between the ground-state reduction potential (E^o) and the excited-state reduction potential (E^{o*}). If this energy difference can be transduced to a change in protic bond strength, the difference in the ground-state acid-dissociation constant (pK_a) and the excited-state acid-dissociation constant (pK_a^*) can also change by this amount of free energy, where $\Delta\Delta G^o \approx -nF(E^o-E^o) \approx 2.303RT(pK_a-pK_a^*)$. The electron redistribution that results after MLCT in an inorganic chromophore can be infinitely tuned by changing the metal identity and/or ligand scaffold. The first example of ESPT using an inorganic coordination compound was reported in 1977 by Wrighton and coworkers using $[Ru^{II}(bpy)_2(2,2'$-bipyridine-4,4'-dicarboxylic

acid)]$^{2+}$.[22] In the excited-state, the reduced acceptor ligand became more Brønsted basic, and thus this compound was a photobase. This same research group followed up a year later with studies using compounds of the form [L$_2$Ru(4,7-dihydroxy-1,10-phenanthroline)]$^{2+}$ in which the identity of the polypyridyl ligand L was varied. The aforementioned compounds were determined to be photoacids with average $\Delta pK_a = 5$ for all the investigated derivatives.[23] During that time, only a handful of inorganic photoacids using polypyridyl ligands were reported in the literature, most of which exhibited small values for $|\Delta pK_a|$.[19,22–30] Since that time, more examples of photoacids and photobases containing other various transition metals have been reported.[6,31–45] It is hypothesized that the small energy conversion efficiencies of organic and inorganic photoacids is due to the small dipolar character in the excited state. Partial or weak intramolecular charge transfer results in small changes in polarity near the protic functional groups and ultimately, a small value for $|\Delta pK_a|$. However, many inorganic compounds exhibit large dipolar excited states and therefore have the potential to exhibit larger ΔpK_a.

Heteroleptic bis-cyclometallated iridium compounds of the form [(C^N)$_2$Ir(N^N)]$^+$ have absorption peaks in the 350 – 500 nm range with extinction coefficients ~5,000 M^{-1} cm^{-1}. These features are generated by singlet-to-triplet MLCT transitions due to strong spin-orbit coupling of iridium from heavy atom effects. This spin-orbit coupling engenders significant allowedness to the formally forbidden triplet to singlet ground state emission. This results in relatively long lifetimes ranging from the nanosecond to microsecond time-scale with quantum yields approaching 100%. The spectroscopic properties of these molecules can be tuned to suite application-based needs through modifications of the cyclometallating and ancillary ligand framework.[46] These types of Ir(III) compounds have been used extensively as phosphorescent organic light-emitting diode materials due to their favorable attributes of reversible photochemistry, microsecond excited-state

lifetimes, near unity quantum yields for emission, synthetic versatility, and tunable photophysical properties via ligand modification. These properties also make them attractive candidates as inorganic photoacids. Synthetic modularity provides a means to install protic functional groups on the donor phenyl pyridine ligand and modify the neutral acceptor ligands to tune the spectroscopic properties. Due to their donating character, the strong-field cyclometallating ligands should become partially oxidized after photoexcitation to promote the desired ESPT. The large donor strength of these ligands results in higher-energy metal-centered (MC, e_g) ligand-field states, thus slowing excited-state deactivation.[47] The long excited-state lifetimes and near unity quantum yields make the complexes well-suited for excited-state pK_a determination by fluorometric titrations.
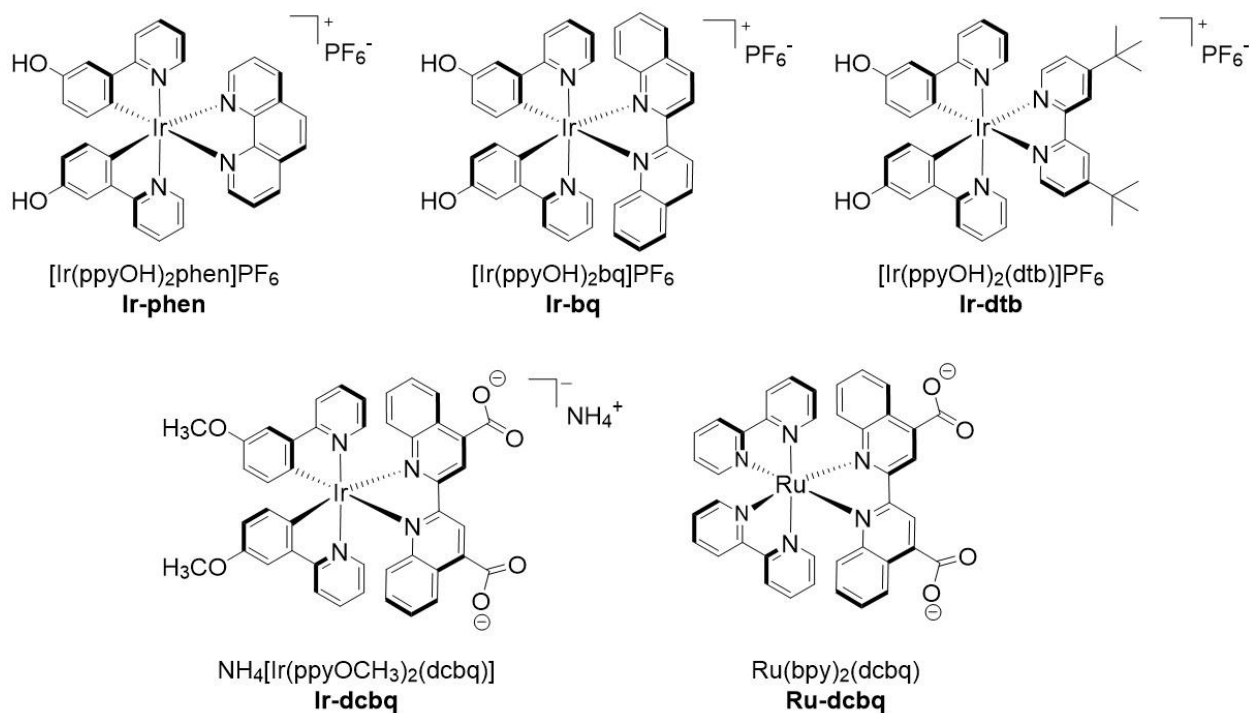
Figure 4.3. Inorganic coordination photoacid/photobase compounds. Ir-phen, Ir-bq, and Ir-dtb are newly synthesized cationic iridium (III) photoacid compounds. Ir-dcbq is anionic iridium (III) photobase and Ru-dcbq is neutral ruthenium (II) photobase.

112

In this work, iridium(III) compounds of the form, $[Ir^{III}(2\text{-}(3\text{-}$ hydroxyphenyl)pyridine$)_2$(N^N)]PF$_6$, where (N^N) is 1,10-phenanthroline (**Ir-phen**), 2,2'-biquinoline (**Ir-bq**), or 4,4'-di-*tert*-butyl-2,2'-bipyridine (**Ir-dtb**) were synthesized and characterized along with an iridium photobase, $[Ir^{III}(2\text{-}(3\text{-methoxyphenyl})\text{pyridine})_2(2,2'\text{-}$ biquinoline-4,4'-dicarboxylic acid)]PF$_6$ (**Ir-dcbq**), and a control ruthenium analog, $[Ru^{II}(\text{bipyridine})_2(\text{dcbq})]$ (**Ru-dcbq**) (Figure 4.3). The identity of the neutral acceptor ligand was varied from **Ir-dtb**, to **Ir-phen**, to **Ir-bq** in order to tune the wavelengths at which the photoacids absorb light. The systematic increase in the extent of conjugation will lower the energy level of the lowest unoccupied molecular orbital and decrease the energy of the charge transfer transition (Figure 4.4). The goal of this proposed research is to impart photoacidity on these Ir(III) d^6 octahedral coordination compounds.
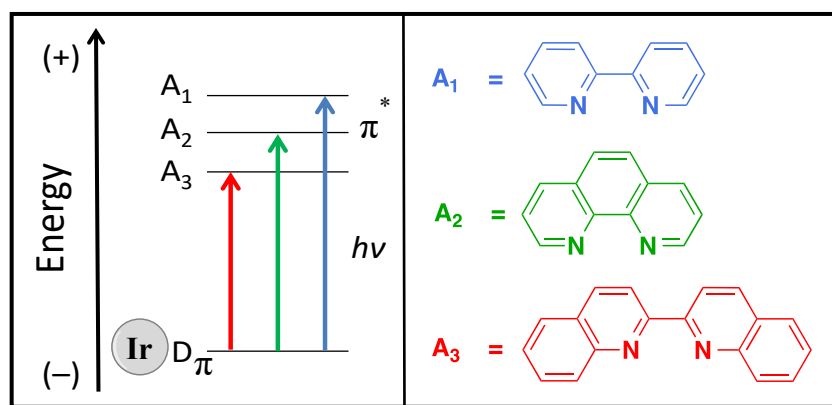
Figure 4.4. Energy-level diagram illustrating that the lowest-energy donor–acceptor (D–A$_n$) absorption transition can be tuned through the choice of acceptor ligand (A$_n$) (panel at right), within the proposed molecular inorganic coordination-compound photoacids.

4.2 Results

4.2.1 Synthesis of Cyclometallated Ir(III) Compounds

Scheme 1 illustrates the pathway used to synthesize pure hydroxyl-containing species of **Ir-phen**, **Ir-bq,** and **Ir-dtb**, in yields of 50-60%. The 2-(3-methoxyphenyl)pyridine (ppyOMe) ligand was synthesized using the well-established Suzuki cross-coupling reaction.[48] and subsequently used to synthesize the cyclometallated iridium(III) chloro-bridged dimer, $[Ir(ppyOMe)_2Cl]_2$, by the Nonoyama reaction.[49] The dimer $[Ir(ppyOMe)_2Cl]_2$ was then treated with the appropriate ancillary ligand under reflux which was followed by anion exchange at 0 °C.[50] This synthesis route produced solids of the desired products, with the general form $[Ir^{III}(ppyOMe)_2(N\char`\^N)]PF_6$. The cationic iridium(III) compounds were then treated with BBr_3 to deprotect the methoxy-substituted position on the phenyl ring and generate a phenol to obtain the desired products, **Ir-phen** (87% yield), **Ir-bq** (48% yield), and **Ir-dtb** (15% yield). The ruthenium photobase, **Ru-dcbq,** was used as received. A brief description of the synthesis is given in the experimental section and can be found elsewhere.[51,52]
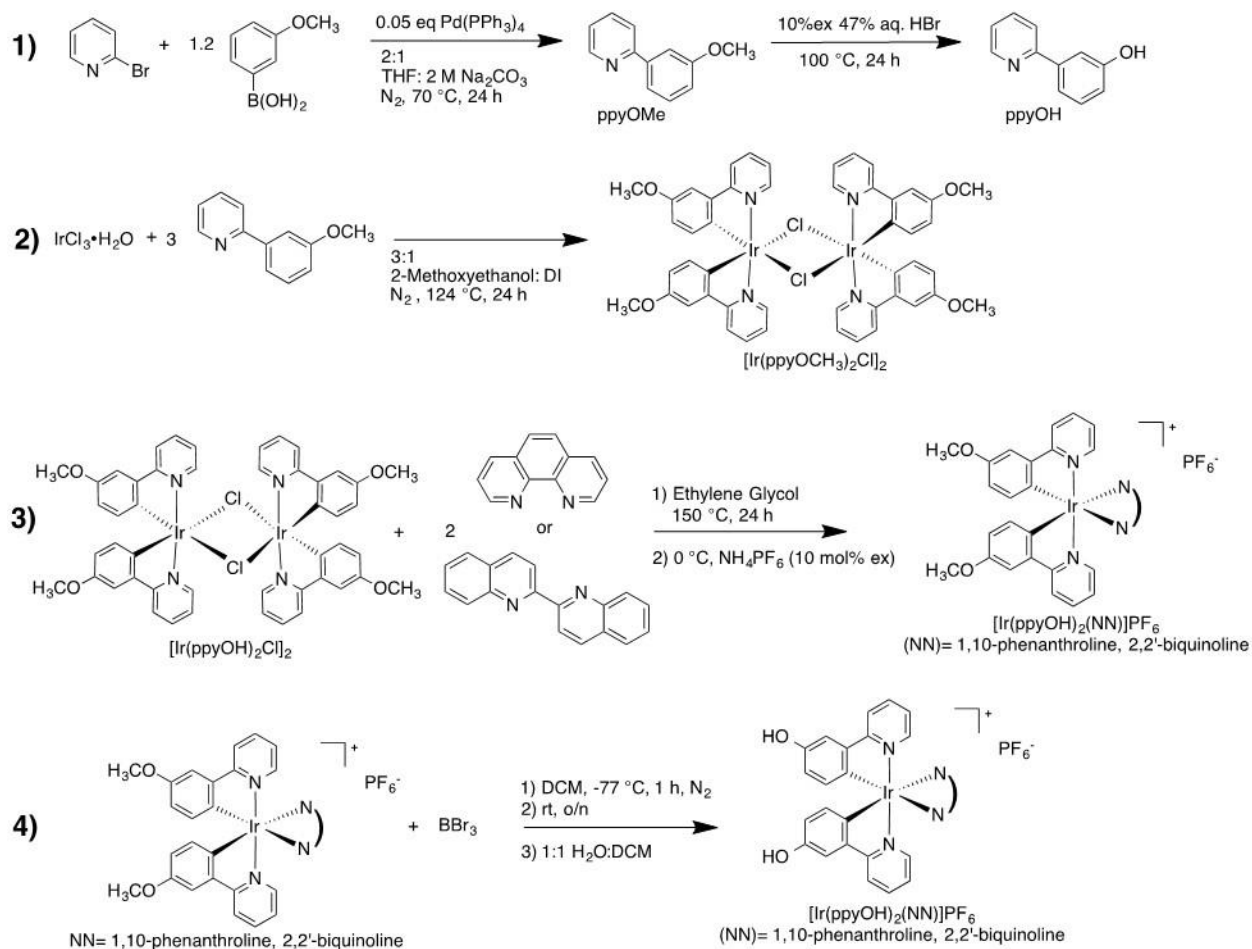
Scheme 4.1. Synthesis of heteroleptic Ir(III) complexes: **Ir-phen**, **Ir-bq**, and **Ir-dtb**.

Due to the low solubility of the [Ir(ppyOMe)$_2$Cl]$_2$ dimer, dimethyl sulfoxide(DMSO)-d$_6$ was used to as the solvent for ^{1}H NMR spectroscopy. DMSO-d$_6$ cleaved the dimer, and the NMR spectra obtained was representative of the DMSO adduct, as previously reported.[28] Analysis by mass spectrometry revealed a monomeric species that is representative of a cleaved dimer with aquo ligands in place of the bridging chlorides. Structural characterization by x-ray crystallography revealed that the [Ir(ppyOMe)$_2$Cl]$_2$ dimer is formed in the solid state (Figure 4.5) even though it was not observed in solution by NMR spectroscopy or mass spectrometry.
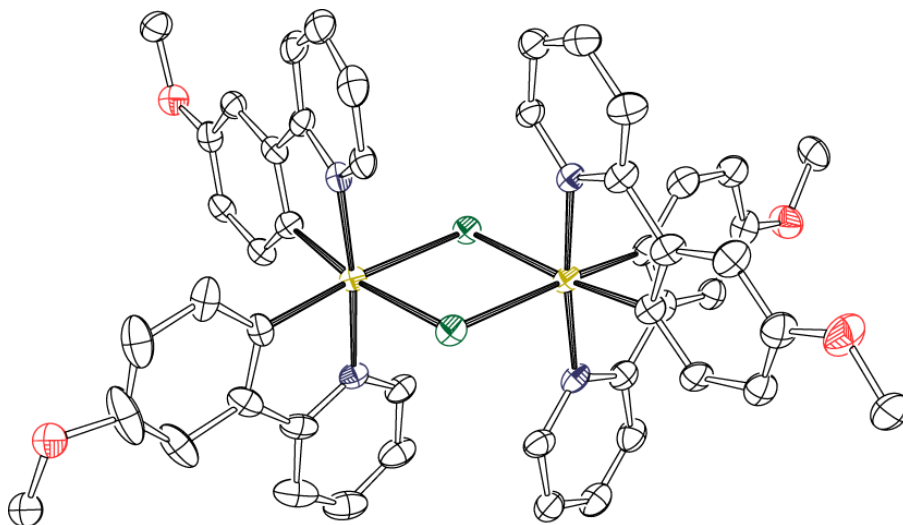
Figure 4.5. ORTEP of the Nonoyama reaction product, [Ir(ppyOMe)$_2$Cl]$_2$ Ellipsoids are shown at 50% probability. Hydrogen atoms and solvent molecules have been omitted for clarity.

The methoxy intermediates were diamagnetic and characterized by ^{1}H NMR spectroscopy in CD$_3$OD or CD$_3$Cl$_3$. All of the iridium complexes showed sharp resonances in the normal diamagnetic region of the spectrum. The aromatic region contained resonances between 6.0 ppm and 8.9 ppm corresponding to the aromatic protons of the two phenyl pyridine ligands and the bipyridyl ligand. In the alkyl region, a singlet around 3.85 ppm integrated to 6 protons and was assigned to the methoxy groups of the phenyl pyridine ligands for all complexes. In the case of **Ir-dtb**, a singlet at 1.47 (18H) corresponding to the two *tert*-butyl groups on bipyridine was observed. The molecular structure of [Ir^{III}(ppyOMe)$_2$(biquinoline)]PF$_6$ (**Ir-bq**), obtained from single-crystal X-ray diffraction experiments, is shown in Figure 4.6. The structural data demonstrated that the complex contains three bidentate ligands coordinated to the iridium metal in a distorted octahedral geometry. The distortion can be quantified using the octahedral distortion parameter (Σ), defined as the sum of the absolute deviations from 90° for the 12 *cis* angles in the coordination sphere;[53,54] $\Sigma = 85.9°$ in **Ir-bq**. The complex contains a PF$_6$ counter ion, which confirms the presence of an

iridium (III) metal center with two anionic ligands and one neutral ligand for an overall cationic complex.
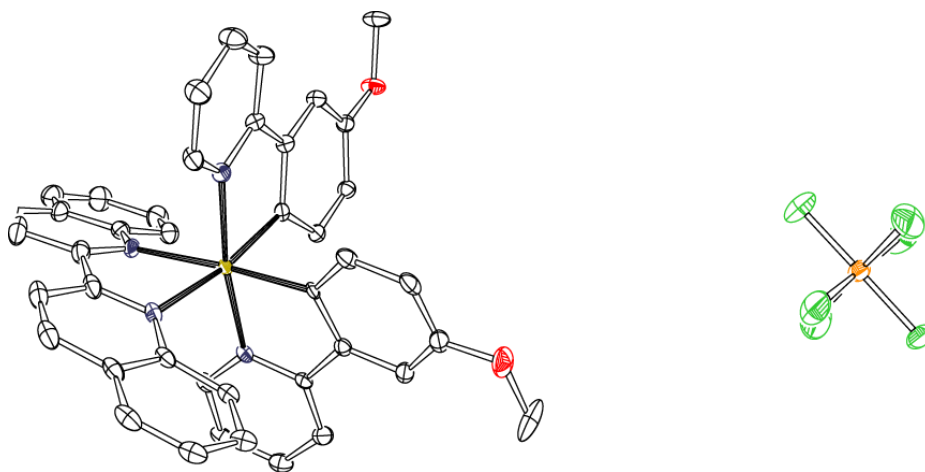
Figure 4.6. ORTEP of [Ir^{III}(ppyOMe)$_2$(biquinoline)]PF$_6$. Ellipsoids are shown at 50% probability. Hydrogen atoms and solvent molecules have been omitted for clarity.

In the final step, the [Ir(ppyOMe)$_2$(N^N)]PF$_6$ complexes were reacted with four equivalents of BBr$_3$ to demethylate [Ir(ppyOMe)$_2$(N^N)]PF$_6$ and obtain the hydroxylated derivatives: [Ir(ppyOH)$_2$(N^N)]PF$_6$. In the first attempts, the final product of this reaction would adhere to the silica column which did not occur when the hydroxyl derivatives were synthesized using ppyOH directly. It was hypothesized that remaining bromide anion, from the reaction with BBr$_3$, displaced the hexafluorophosphate as the negative counterion. Upon of addition of NH$_4$PF$_6$ to the column eluent, the desired [Ir(ppyOH)$_2$(N^N)]$^+$ compound began to move through the column. Being able to purify the products of the BBr$_3$ deprotection reaction by column chromatography allowed for the first successful isolation of pure **Ir-phen**, **Ir-bq**, and **Ir-dtb**. The ^{1}H NMR spectra of the hydroxyl derivatives were consistent with spectra of the methoxy congeners and lacked the –OMe singlet at 3.85 ppm. Despite rigorous attempts, X-ray quality crystals of the hydroxylated Ir(III) compounds (Figure 4.3) could not be obtained.

4.2.2 Electronic Absorption Spectroscopy and pK_a Titrations

All compounds show intense absorption bands with a molar absorption coefficient (ε) of 6,000 M^{-1} cm^{-1} or greater at < 400 nm, moderate absorption bands with ε between 2,000 and 4,000 M^{-1} cm^{-1} in the 400 – 500 nm region, and weak absorption bands with ε values of 1,600 M^{-1} cm^{-1} or less, if any, in the 500 – 700 nm region. Based on previous reports,[43,55–58] the intense absorption bands in the ultraviolet region (below 400 nm) are similar to those observed for the free diimine ligands and therefore are assigned to the spin-allowed intra-ligand (or ligand centered, LC) π-π* transition. Bands in the 390–490 nm range can be assigned to the spin-allowed ^{1}MLCT, dπ-π* transition. The weakest absorbance ranging from 500 – 675 nm can be assigned to the spin-forbidden ^{3}MLCT transitions.[46]

Figure 4.7. (a) The ground state acid-base titrations of **Ir-phen**, carried out using 0.1 M HCl(*aq*) and 0.01 M NaOH(*aq*) solutions, each containing 0.1 mM of **Ir-phen**. (b) The normalized single wavelength data with the fit used to determine the pK_a value.

Figures 4.7–4.9 show the electronic absorption spectra obtained for the spectrophotometric determination of pK_a for **Ir-phen**, **Ir-bq**, and **Ir-dtb**. The acid-base titrations of **Ir-phen** were

carried out using aqueous solutions of 0.1 M HCl and 0.01 M NaOH, each containing 0.1 mM of

Ir-phen. Figure 4.7(a) shows that at the initial pH of 12.75, at which both hydroxyl groups should

be deprotonated, there are absorption peaks at 265 nm and 442 nm. As the pH is decreased to more

acidic values, leading to protonation of the hydroxyl groups, the bands decrease in intensity and

the feature at 440 nm is lost entirely. The change in absorbance at 442 nm was plotted as a function

of pH to determine a ground state pK_a value of 10.3 for **Ir-phen**.
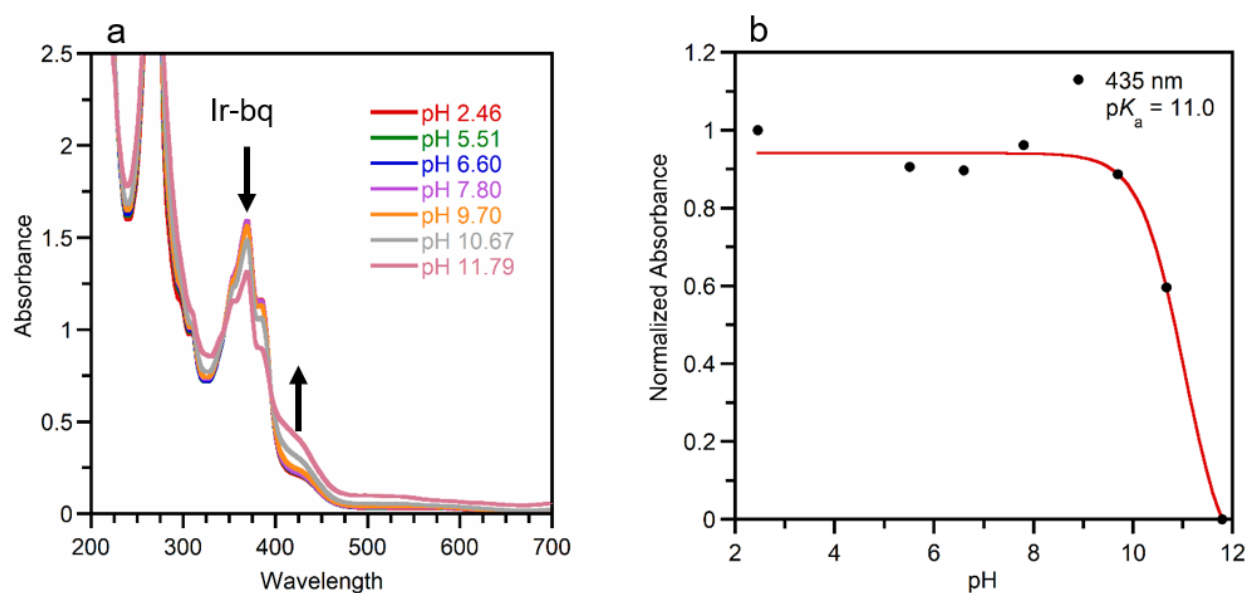
Figure 4.8. (a) The ground state acid-base titrations of **Ir-bq**, carried out using 0.1 M HCl and 0.01 M NaOH solutions in CH₃CN, each containing 0.1 mM of **Ir-bq**. (b) The normalized single wavelength data with the fit used to determine the pK_a value.

Due to the low solubility of **Ir-bq** in water, the titration of **Ir-bq** was performed using solutions

of 0.1 M HCl and 0.01 M NaOH in acetonitrile, each containing 0.1 mM of **Ir-bq**. Figure 4.8(a)

shows that at the initial pH of 2.46, at which both hydroxyl groups should be protonated, there are

absorption peaks at 350 nm, 370 and 435 nm. As the pH is increased to more basic values, leading

to deprotonation of the hydroxyl groups, the bands at 350 and 370 nm decreased in intensity and

the band at 435 increased in intensity while maintaining clear isosbestic points at 320 and 400 nm.

The change in absorbance at 435 nm was plotted as a function of pH to determine a ground state

pK_a value of 11.0 (Figure 4.8b) for **Ir-bq.** The titration of **Ir-dtb** was also performed in acetonitrile

with 0.06 mM of **Ir-dtb**. Figure 4.9(a) shows that at the initial pH of 4.95, the absorption spectrum

of **Ir-dtb** contains peaks at 275 nm, 308 and 440 nm. As the pH is increased to more basic values,

the band at 275 and 308 nm increased in intensity and the band at 440 nm decreased only initially.

When the change in absorbance at 275 nm was plotted as a function of pH, two inflection points

were observed. The first inflection point corresponding to a pK_a value of 6.6 was attributed to a

potential impurity and the second inflection point corresponding to a pK_a of 10.7 was assigned to
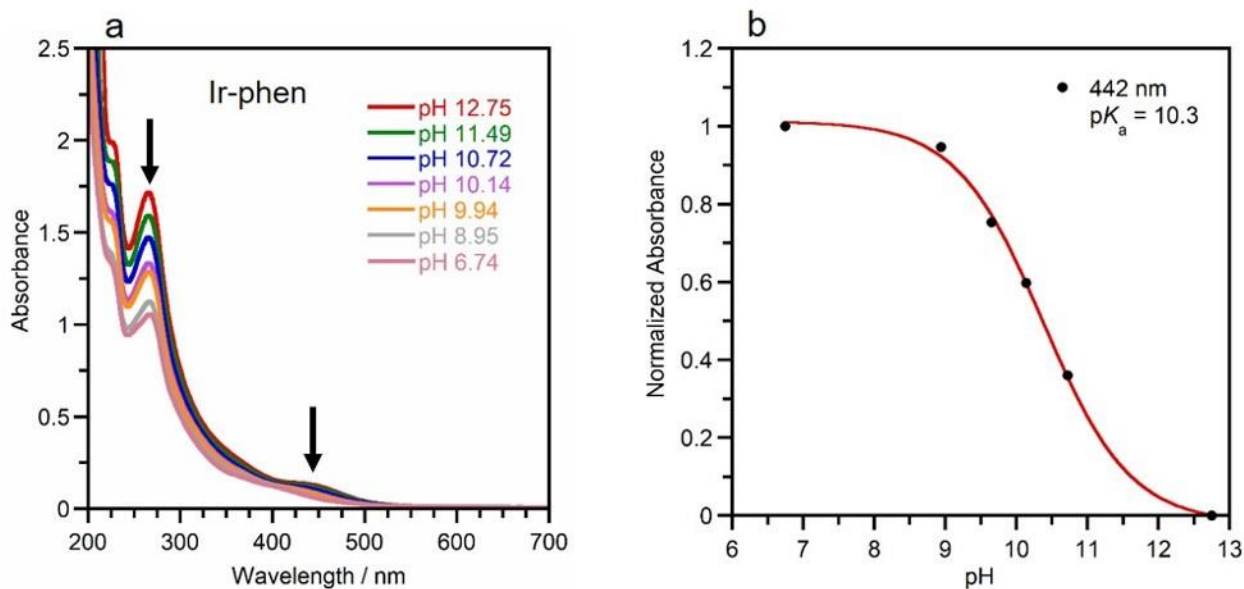
the hydroxyl group of interest.
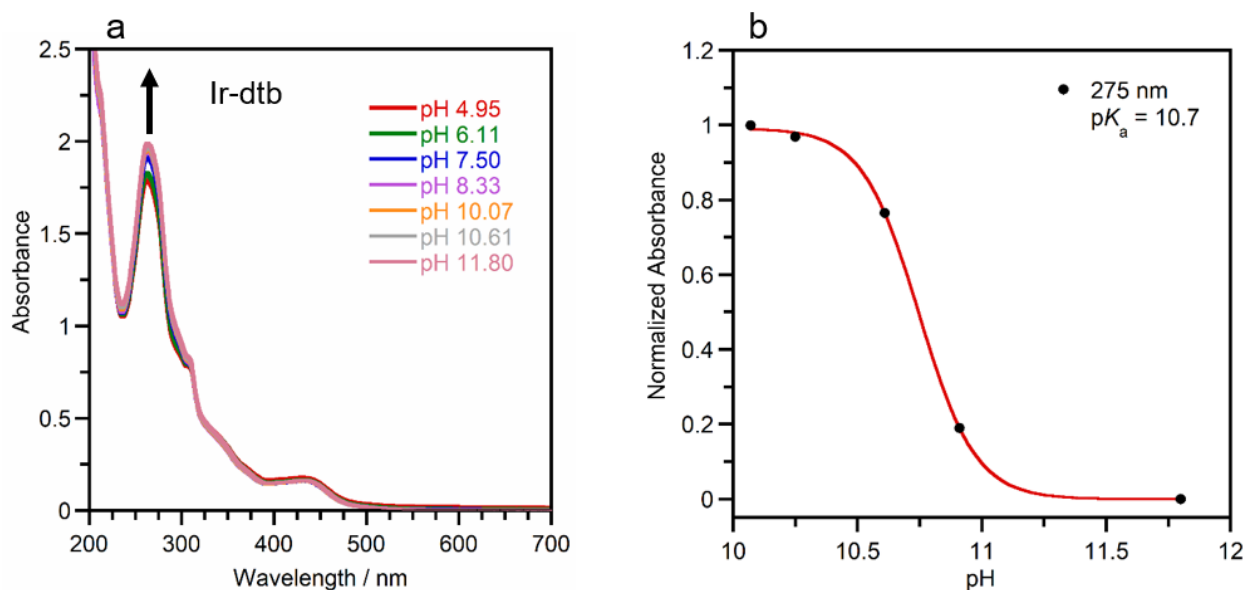
Figure 4.9. (a) The ground state acid-base titrations of **Ir-dtb**, carried out using 0.1 M HCl and 0.01 M NaOH solutions in CH$_3$CN, each containing 0.06 mM of **Ir-dtb**. (b) The normalized single wavelength data with the fit used to determine the pK_a value.

The titrations of **Ir-dcbq**, a potential photobase, were carried out using aqueous solutions

of 0.1 M HCl and 0.01 M NaOH, each containing 0.1 mM of **Ir-dcbq**. Figures 4.10(a) shows that

as the compound was titrated from acidic to basic pH, the peak at 275 nm had an increase in

120

intensity, the peak around 380 nm increased in intensity and blue shifted to 350 nm, and the peaks at 420 and 600 nm decreased, and blue shifted slightly. The change in absorbance at 380 nm was plotted as a function of pH to determine a ground state pK_a value of 3.4 for **Ir-dcbq**. For reference, a ruthenium complex like those previously reported was also characterized. The base-titrations of **Ru-dcbq** were carried out in aqueous solutions with 9% ethanol (due to decreased solubility of **Ru-dcbq**). Figure 4.11(a) shows that as the compound was titrated from acidic to basic pH, the features of the absorption peaks at 275, 350, 425, and 550 nm changed in shape and in some cases showed a small blue shift. The absorbance at 390 nm was plotted as a function of pH to determine a ground state pK_a value of 2.0 for **Ru-dcbq**.

Figure 4.10. (a) The ground state acid-base titrations of **Ir-dcbq** carried out in 0.1 M HCl(*aq*) and 0.01 M NaOH(*aq*), each containing 0.1 mM of **Ir-dcbq**. (b) The normalized single wavelength data with the fit used to determine the pK_a value.
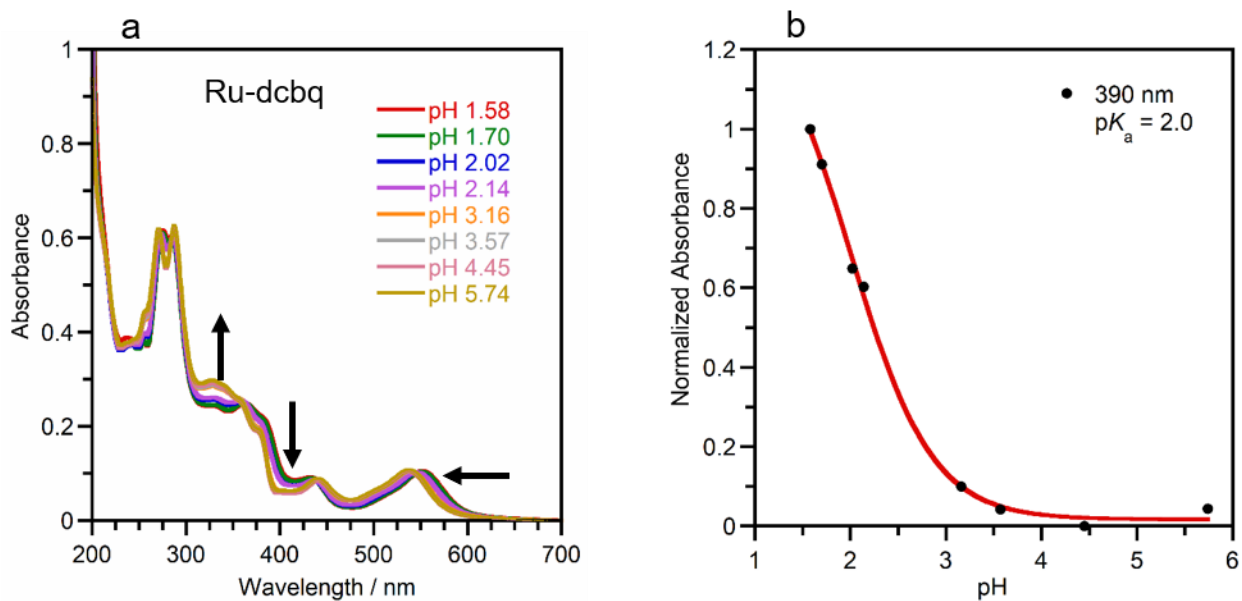
Figure 4.11. (a) The ground state acid-base titrations of **Ru-dcbq** carried out using 0.1 M HCl(*aq*) and 0.01 M NaOH(*aq*) with 9% ethanol, each containing 0.1 mM of **Ru-dcbq**. (b) The normalized single wavelength data with the fit used to determine the pK_a value.

4.2.3 Photoluminescence Spectroscopy

Photoluminescence spectroscopy was used to measure the fluorescence of each compound and fluorometric titrations were performed in order to determine the excited state pK_a, pK_a^*. This method was selected because bis-cyclometallated iridium compounds are strong emitters and previous reports of ruthenium photobases used this method to measure pK_a^*. As seen in Figure 4.12(a), **Ru-dcbq** was excited at 525 nm and the photoluminescence titration showed an increase in emission intensity at 770 nm as the pH increased. The emission intensity at 770 nm was plotted as a function of pH to determine a pK_a^* value of 3.4. Using the pK_a^* and the pK_a value determined from the absorption titration a ΔpK_a (pK_a^* – pK_a) of 0.9 was determined. The ΔpK_a suggested mild photobasic behavior for **Ru-dcbq**. For all the iridium compounds, pK_a^* could not be accurately determined using fluorescence titrations. The addition of protic functional groups to the ligand scaffold resulted in an unexpected quenching of the emission typically observed for these

compounds. In addition to weak emission intensity, the following issues were encountered: (1) the emission spectrum would show multiple emission peaks with varying intensities, (2) the emission wavelength was higher in energy than the excitation wavelength, and (3) the emission features observed would change based on the excitation wavelength that was used. While these observations could be a result of some unique or uncommon photochemical phenomena, undetected impurities from the compound synthesis could not be conclusively eliminated as a contributing factor.
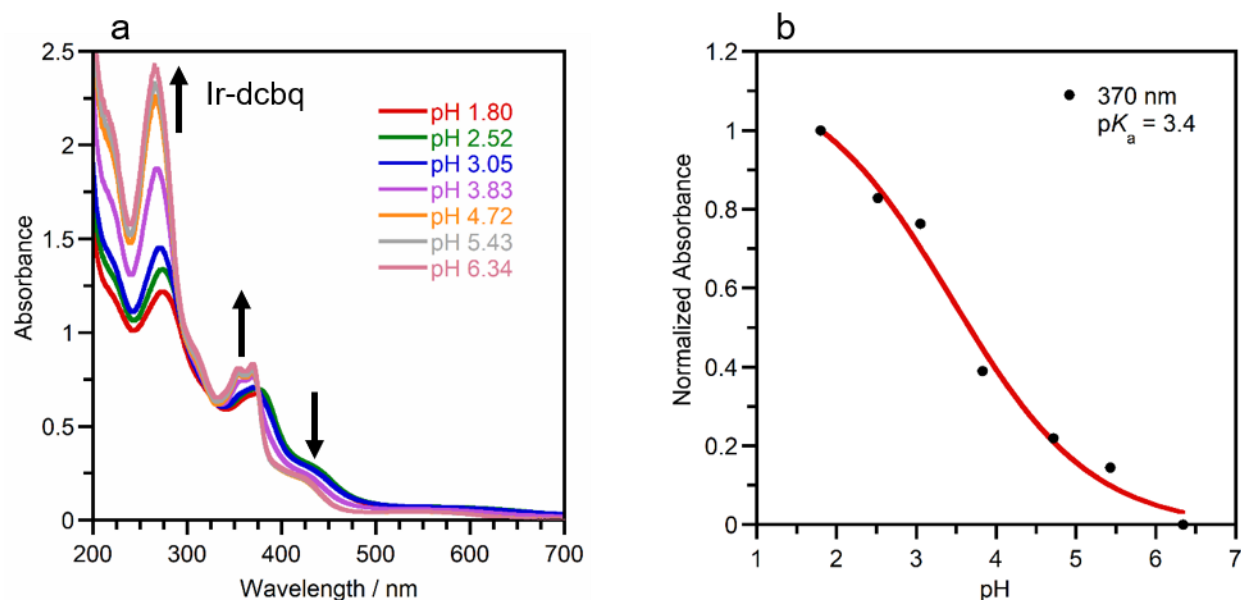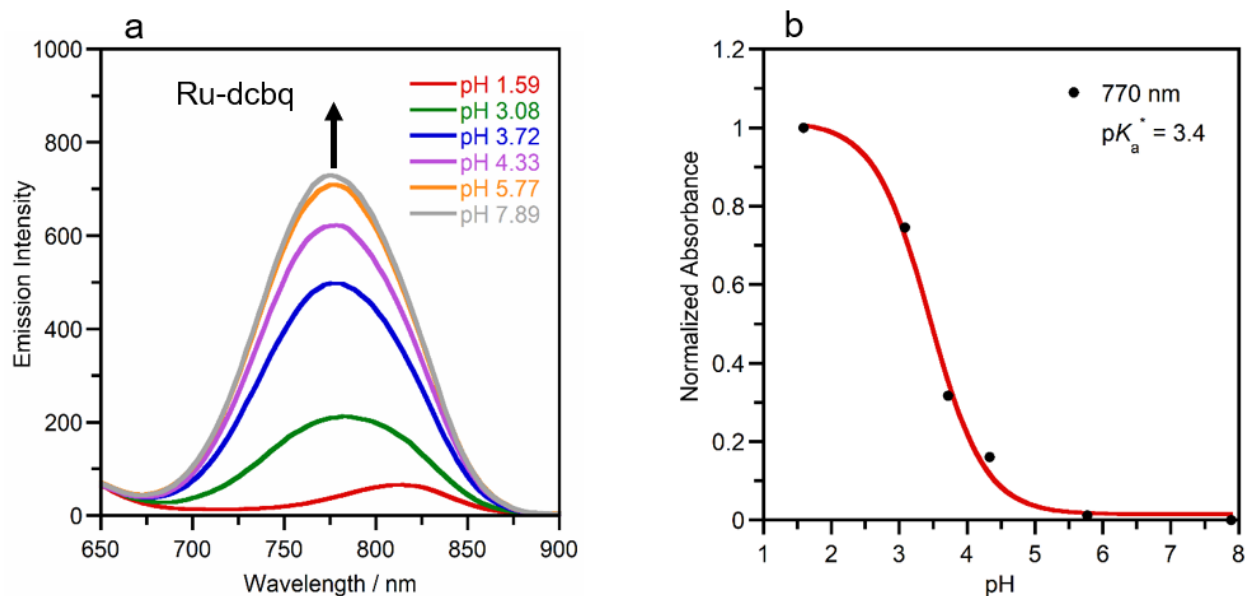

Figure 4.12. (a) The excited-state acid-base titrations of **Ru-dcbq**, carried out in 0.1 M HCl(*aq*) and 0.01 M NaOH(*aq*), each containing 0.1 mM of **Ru-dcbq**. (b) The normalized single wavelength data with the fit used to determine the pK_a* value.

4.3 Discussion

To the best of our knowledge, cationic iridium(III) compounds with a hydroxyl group on the cyclometaling ligand have not been previously reported for studies of ESPT. In the early stages of this research, the addition of a hydroxyl group to the phenyl ring resulted in synthetic challenges that prevented the isolation of the pure product. In order to overcome those obstacles, the methoxy

functional group was left as a protecting group on 2-phenyl pyridine and the cationic cyclometallating iridium(III) compounds were generated with 2-(3-methoxyphenyl)pyridine (ppyOMe). Contrary to the viscous oil products generated using ppyOH, ppyOMe resulted in cleaner reactions from which solid products could be isolated and purified with ease. Despite the harsh conditions of the deprotection reactions, the methoxy derivatives were successfully treated with BBr$_3$ to convert the methoxy functional group into a hydroxyl without compromising the stability of ligands coordination to the metal.

Acid-base titrations were carried out by using 0.1 M HCl and 0.1 M NaOH solutions, each containing a known concentration of the appropriate photoacid/base. The pH was monitored using a pH meter and the electronic absorption spectra were obtained at varying pH values. The absorption at a single wavelength was plotted against the pH of the solution and a nonlinear Boltzmann fit was used to determine the pK_a of the protic functional group from the inflection point of the titration curve. Performing acid-base titrations in aqueous solutions is common practice; however, some of the compounds were insoluble in water and required a nonaqueous solvent for the acid-base titrations. **Ir-phen** and **Ir-dcbq** were water soluble and their acid-base titrations were performed using aqueous solutions of HCl and NaOH. The solubility of **Ir-phen** and **Ir-dcbq** in water is significant because it makes these compounds viable for applications that require an aqueous environment. The titrations of **Ru-dcbq** were carried out in aqueous solutions containing 9% ethanol; no special considerations were taken during the titrations because the solutions were >90% aqueous. On the other hand, **Ir-dtb** and **Ir-bq** were titrated from an initially acidic pH to alkaline pH using solutions of HCl and NaOH in acetonitrile. Since acetonitrile is a nonaqueous solvent, its properties had to be taken into consideration. Acetonitrile is polar like water, but it is aprotic. This means it is not capable of hydrogen bonding or serving as a proton ion

source the way water does. Acetonitrile has a relatively large dielectric constant (ε) of 37.5, which is a desirable feature for acid-base reactivity because it makes it favorable for ions pairs to dissociate into individual solvated ions. Lastly, acetonitrile it has low basicity and even lower acidity than water (CH_3CN autoprotolysis constant, $pK_{ap} \approx 33$), and that low acidity means it is not good at solvating anions. Based on these properties, compounds in acetonitrile will have different interactions with the environment than those in water, which will influence the acid-base properties observed. The compilation of published pK_a values for acids and bases in acetonitrile demonstrate that a pK_a value determined in acetonitrile is typically larger than when measured in water. For example, the reported pK_a value for phenol is 9.95 in water and 29.14 in acetonitrile. Another factor that must be considered when transitioning to measurements in an organic solvent is whether pH can be measured in a nonaqueous solution using a traditional pH electrode and meter like done for the work herein. Challenges such as electrode dehydration, miscibility of the electrode solution and sample, and unstable readings and drift can result in loss of measurement precision. The glass bulb of the electrode has a hydrated gel outer layer that is responsible for sensing the hydrogen ion activity of the solution. If this gel layer becomes dehydrated by a nonaqueous solvent this will disrupt the sensing and lead to decreased precision. If the sample is immiscible with the fill solution of the electrode, a junction potential will develop and lead to a bias in the results. The electrical components of the meter will also be limited by a sample that has a high impedance or is a poor electrical conductor. Even though relatively stable measurements of pH were obtained, the measurement is also limited by the fact that pH, as measured in water, is the negative log of hydronium ion activity in an aqueous solution. Therefore, the values obtained for **Ir-bq** and **Ir-dtb** represent an "operational" value that is strictly based on the pH meter in the acetonitrile solution, which is complicated by the fact that the pH was calibrated using aqueous standards.

Table 4.1 lists the calculated pK_a values for all the compounds reported. The pK_a values determined for the photoacids **Ir-dtb**, **Ir-phen**, and **Ir-bq** ranged from 10 to 11, which is within the range of the values of phenol in water. Although a much higher value is expected for the systems measured in acetonitrile, this was not observed. An alternative measurement for proton activity that may result in better accuracy and precision in the future is to use a method in which pK_a is determined using the acid dissociation equilibrium reaction and mass balance, such as that reported for similar systems.[59,60]

Table 4.1. Experimentally determined pK_a and pK_a* values for photoacids and photobases.

Complex	pK_a	pK_a*	ΔpK_a
[Ir(ppyOH)$_2$phen]PF$_6$	10.3	--	--
[Ir(ppyOH)$_2$bq]PF$_6$	11.0	--	--
[Ir(ppyOH)$_2$dtb]PF$_6$	10.7	--	--
NH$_4$[Ir(ppyOMe)$_2$dcbq]	3.4	--	--
[Ru(ppyOMe)$_2$dcbq]	2.0	3.4	0.9

As previously mentioned, the base-titrations for **Ru-dcbq** were performed using solutions of HCl and NaOH in 9% ethanol in deionized water. **Ru-dcbq** was determined to have a ΔpK_a value of +1.4. The magnitude of the change is suggestive of weak photobasic behavior. The ΔpK_a is the same order of magnitude as that reported for by Sasse and coworkers for [Ru(bpy)2(4,4'-dicarboxylic acid-2,2'-bipyridine)]$^{2+}$, ΔpK_a = 1.6. This result is unexpected because the incorporation of the two cyclometalling ligands functionalized with the electron donating methoxy groups (ppyOMe) was expected to strongly shift electron density toward the carboxylic acid functional groups on the biquinoline ligand and result in a significantly stronger base. The small ΔpK_a could be a result of the ppyOMe ligands donating electron density to the oxidized metal center generated by MLCT. The difference between **Ru-dcbq** and [Ru(bpy)$_2$(4,4'-dicarboxylic

acid-2,2'-bipyridine)]$^{2+}$ is that the former has the protic groups on 2,2'-biquilione which has greater conjugation and hence a lower energy LUMO than that 2,2'-bipyridine. The similarity in ΔpK_a for these two compounds suggest that changes in the energy of the LUMO to alter the energy of the charge transfer does not significantly impact the ΔpK_a.

Definitive pK_a^* values could not be obtained for the iridium compounds due to inconclusive photoluminescence data. However, preliminary data suggested that these compounds also had weak to no photoacidic/photobasic behavior, like that observed for **Ru-dcbq**. This was unexpected because the larger contribution from the cyclometalating ligand to the HOMO gives these compounds enhanced (mixed-metal-ligand)-to-ligand charge transfer ((ML)L'CT) character which should result in a large excited-state dipole. However, it is hypothesized that having two ppyOH ligands that donate towards the metal center could result in a weaker dipole because it is shared by the two donating ligands. To investigate this hypothesis, tris-heteroleptic compounds containing only one ppyOH could be synthesized. This modification could also prevent complications that may arise when trying to measure pK_a with two protic functional groups on one compound. Furthermore, other factors that affect our ability to measure pK_a^* must be considered. Measurements of chemical properties such as the acid dissociation constant, K_a, in the ground state can be carried out rather easily, however, the determination of these properties in the excited state is not as straightforward due to the short lifetime of the excited state.[8] For most molecules, the singlet excited state, S_1, has a lifetime ranging from 10^{-6} s (μs) to 10^{-9} s (ns) and a triplet excited state, T_1, has a lifetime of 10^{-6} s (μs) to seconds.[61] Meanwhile, proton dissociation, solvation, and mobility occur on the picosecond time scale.[10] Since fluorescence occurs rapidly and can be easily measured, it can be used to determine the excited state acidity constant (K_a^*) of the singlet molecular excited state.[62] However, the excited state of a molecule can return to the ground state

via radiative photon emission (fluorescence/phosphorescence), or nonradiative processes such as: vibrational relaxation, bond dissociation or rearrangement, or change in electron spin multiplicity.[8,62] Rapid relaxation to the ground state via a nonradiative pathway can kinetically outcompete ESPT and therefore, prevent measurement of pK_a* by direct fluorescence titrations.

After deprotonation, the proton can also participate in an adiabatic recombination reaction (equation 4.1) or in a nonadiabatic quenching reaction (equation 4.2).[10]

$$RO^{-*} + H^+ \xrightarrow{k_a} ROH^* \qquad (4.1)$$

$$RO^{-*} + H^+ \xrightarrow{k_q} ROH \qquad (4.2)$$
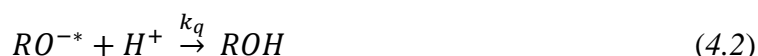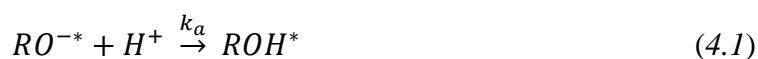
These reactions were first observed at low pH values where they could occur with the homogenous distribution of protons. Harris and Selinger showed that nonadiabatic proton quenching was a major factor in the excited-state kinetics of 1-naphthol. Their study demonstrated that ROH* and RO$^-$* could be quenched by protons with the latter being quenched more than an order-of-magnitude faster.[63] It was later learned that these reactions could also occur at neutral pH values with the geminate proton.[64] In the iridium systems reported, the weak emission that prevents direct measurement of pK_a^*, could be a result of (1) nonradiative decay caused by the hydroxyl functionalization, (2) picosecond excited-state lifetimes, or (3) quenching resulting from a proton transfer reaction.

4.4 Conclusions

The goal of this project was to synthesize cyclometallated inorganic coordination compounds that would function as photoacids and/or photobases for the study of excited-state proton transfer. Toward this, a series of bis-cyclometallated iridium compounds were synthesized

and studied by physical methods in order to understand how the addition of a hydroxyl group affected the photophysical properties of the compounds. Electronic absorption spectroscopy measurements of all the compounds showed absorption bands in the visible region with $\varepsilon < \sim 3000$ $M^{-1}\ cm^{-1}$ attributed to spin-allowed ^{1}MLCT $d\pi$-π^* transitions. These molar absorption coefficients are within the range typically observed for these types of compounds. The emission spectra of the cyclometallated Ir(III) compounds reveal that there is a significant decrease in emission intensity in comparison to previously reported analogs with no functional groups on the phenyl pyridine ligand. This modification could affect the functionality of **Ir-phen**, **Ir-bq**, and **Ir-dtb** as photoacids and **Ir-dcbq** as a photobase if the low emission intensity is a result of a very short excited-state lifetime. If the excited-state lifetimes are too short the rate of excited-state decay will outcompete the rate of deprotonation, which occurs on the picosecond time scale. The weak emission could also be a result of a quenching reaction following deprotonation. Based on these studies, the iridium systems would not be suitable candidates to observe for photoacid/photobase chemistry. **Ru-dcbq** had the most promising results, with a $\Delta pK_a = +1.4$, indicative of an increase in the basicity in the excited state but the magnitude of this value was not larger than previously reported ruthenium systems. The unexpected and undesired small magnitude of the ΔpK_a value leaves room for improvement. The iridium systems will require a redesign in order to overcome the emission quenching observed in the current system. Additionally, the pK_a values for all compounds must be measured under identical solvent conditions using a probe-free method in order to obtain accurate values and make structure–property comparisons.

4.5 Experimental

General Procedures. All chemicals and solvents were purchased from commercial sources and used as received unless otherwise noted. 2-(3-methoxyphenyl)pyridine (ppyOMe) was

synthesized using the well-established Suzuki reaction followed with a deprotection step using hydrobromic acid to obtain 3-(pyridin-2-yl)phenol (ppyOH). Alternatively, a direct synthesis of ppyOH by a patented method analogous to the Suzuki Cross Coupling was attempted.[65] All measurements were performed at room temperature (~22 °C), unless noted otherwise.

Physical Methods. NMR spectra were collected on Bruker Avance 500 and CRYO 500 MHz spectrometers. Chemical shifts are reported in parts per million relative to the solvent peaks for ^{1}H or ^{13}C in DMSO, CD_3OD, or $CDCl_3$. Electronic absorption spectra were recorded using an Agilent Cary 60 UV–Vis spectrophotometer. Electronic emission spectra were recorded using a Cary Eclipse spectrophotometer.

General 2-(3-methoxyphenyl)pyridine (*ppyOMe*) Synthesis. In a two-neck round bottom flask, 2-bromopyridine (96 mg, 0.6 mmol), and 3-methoxy-phenylboronic acid (104 mg, 0.76 mmol) were combined with tetrahydrofuran and 2 M Na_2CO_3. The mixture was purged with nitrogen while stirring for 20 min. $Pd(PPh_3)_4$ (38 mg, 0.03 mmol) was added under positive pressure. The reaction vessel was sealed and heated for 12 h at 70 °C while stirring. The mixture was allowed to cool to room temperature, quenched with water, extracted with dichloromethane, and concentrated under reduced pressure. The residue was then dissolved in ethyl acetate and washed with a brine solution (3 x 20 mL). The solvent was evaporated under reduced pressure to obtain a cloudy yellow oil. The crude product was purified by flash chromatography (silica gel, 16% ethyl acetate in hexanes, v/v) to yield a hazy oil (1.02 g, 51% yield). ^{1}H NMR (500 MHz, Chloroform-*d*) δ 8.76 (ddd, 1H), 7.81 (m, 2H), 7.66 (dd, 1H), 7.60 (ddd, 1H), 7.44 (t, 1H), 7.31 (m, 1H), 7.04 (ddd, 1H), 3.96 (s, 3H, -OCH_3 peak). MS (ESI LC-TOF): *m/e* [ppyOMe + H]$^+$ 186.6.

Synthesis of [Ir(ppyOMe)₂Cl]₂. The Ir(III) intermediates were prepared and isolated according to the established Nonoyama procedure[49] and other literature methods.[42,66] The cyclometallating ligand, ppyOMe (3 equiv) and $IrCl_3 \cdot xH_2O$ (1 equiv) were dissolved in a 2-methoxyethanol and water (3:1) solution. The reaction mixture was refluxed at 120 °C with constant stirring for 24 h, then cooled to room temperature. For [Ir(ppyOMe)₂Cl]₂., the resulting orange precipitate was collected by vacuum filtration, washed with diethyl ether and water, and dried to yield the product (430 mg, 43% yield). X-ray quality crystals were grown by slow diffusion of dichloromethane/diethylether. ¹H NMR (400 MHz, DMSO-d_6) δ 9.76 (s, 1H), 9.48 (s, 1H), 8.26 (s, 1H), 8.15 (s, 1H), 8.04 (s, 1H), 7.95 (s, 1H), 7.38 (s, 3H), 7.31 (s, 1H), 6.46 (d, J = 8.4 Hz, 1H), 6.37 (s, 1H), 6.05 (s, 1H), 5.47 (s, 1H), 3.62 (d, J = 7.0 Hz, 6H). MS (ESI LC-TOF): *m/e* [Ir(ppyOMe)₂(H₂O)₂] + 2Na⁺]⁺ - 643.06.

Synthesis of [Ir(ppyOMe)₂L]⁺PF₆⁻, (L= 2,2'-biquinoline (bq), 1,10'-phenanthroline (phen), 4,4'-di-tert-butyl-2,2'-dipyridyl (dtb), 2,2'-biquinoline-4,4'-dicarboxylic acid (dcbq). Based on the method published by Lowry and coworkers,[42] [Ir(ppyOMe)₂Cl]₂ (1 equiv) and the appropriate neutral ligand (3 equiv) in dichloromethane/methanol (2:1, v/v) were refluxed at 55 °C with constant stirring for 24 h. After cooling to room temperature, the vial was then placed in an ice bath and a solution of aqueous ammonium hexafluorophosphate (1 g in 10 mL of deionized water) was added drop wise into the vial. The resulting suspension was filtered to collect the solid product that was bright orange ([Ir(ppyOMe)₂phen]PF₆, 406 mg, 67% yield), forest green ([Ir(ppyOMe)₂bq]PF₆, 76 mg, 93% yield), bright orange (([Ir(ppyOMe)₂dtb]PF₆, 70 mg, 43% yield), and bright green ([Ir(ppyOMe)₂dcbq]PF₆, 48 mg, 50% yield).

[Ir(ppyOMe)₂phen]PF₆ − MS (ESI LC-TOF): *m/e* [Ir(ppyOMe)₂phen]⁺- 741.47. ¹H NMR (500 MHz, Methanol-d_4) δ 8.78 (dd, J = 8.3, 1.5 Hz, 2H), 8.41 (dd, J = 5.0, 1.5 Hz, 2H), 8.31 (s, 2H),

8.15 (d, J = 8.5 Hz, 2H), 8.01 – 7.91 (m, 2H), 7.86 – 7.78 (m, 2H), 7.51 (d, J = 2.7 Hz, 2H), 7.46 (d, J = 5.9 Hz, 2H), 6.90 (ddd, J = 7.4, 5.8, 1.4 Hz, 2H), 6.71 (dd, J = 8.3, 2.7 Hz, 2H), 6.30 (d, J = 8.3 Hz, 2H), 3.85 (s, 6H). ^{13}C NMR (126 MHz, Methanol-d_4) δ 167.90, 156.60, 151.00, 148.68, 146.85, 144.25, 138.34, 138.07, 131.87, 128.13, 126.46, 122.99, 119.72, 117.37, 109.85.

[Ir(ppyOMe)₂bq]PF₆ − MS (ESI LC-TOF): m/e [Ir(ppyOMe)₂bq]$^+$- 817.59 ^{1}H NMR (500 MHz, Chloroform-d) δ 8.89 (d, J = 8.8 Hz, 2H), 8.75 (d, J = 8.6 Hz, 2H), 8.04 (d, J = 9.0 Hz, 2H), 7.96 (d, J = 8.3 Hz, 2H), 7.83 (d, J = 8.0 Hz, 2H), 7.77 (d, J = 6.8 Hz, 4H), 7.55 (q, J = 8.9, 8.2 Hz, 2H), 7.25 (ddd, J = 8.7, 6.8, 1.5 Hz, 2H), 7.21 (d, J = 2.7 Hz, 2H), 6.98 (t, J = 6.6 Hz, 2H), 6.68 (dd, J = 8.4, 2.7 Hz, 2H), 6.14 (d, J = 8.4 Hz, 2H), 3.84 (s, 6H). ^{13}C NMR (126 MHz, Methanol-d_4) δ 150.01, 140.85, 138.01, 131.20, 130.89, 129.85, 128.75, 128.34, 128.05, 122.78, 121.48, 119.65, 117.31, 109.71.

[Ir(ppyOMe)₂dtb]PF₆ − MS (ESI LC-TOF): m/e [Ir(ppyOMe)₂dtb]$^+$ − 827.23. ^{1}H NMR (499 MHz, Methanol-d_4) δ 8.71 (d, J = 2.0 Hz, 2H), 8.14 (d, J = 8.2 Hz, 2H), 7.99 (d, J = 5.9 Hz, 2H), 7.92 – 7.79 (m, 2H), 7.66 – 7.56 (m, 4H), 7.46 (d, J = 2.7 Hz, 2H), 7.07 (ddd, J = 7.3, 5.7, 1.4 Hz, 2H), 6.65 (dd, J = 8.4, 2.6 Hz, 2H), 6.19 (d, J = 8.3 Hz, 2H), 3.82 (s, 6H), 1.47 (s, 18H).

NH₄[Ir(ppyOMe)₂dcbq] (Ir-dcbq) − MS (ESI LC-TOF): m/e [Ir(ppyOMe)₂dcbq]$^-$ 903.08. ^{1}H NMR (500 MHz, Methanol-d_4) δ 8.83 (s, 2H), 8.41 (s, 2H), 8.17 (d, J = 9.0 Hz, 2H), 8.05 (d, J = 8.2 Hz, 2H), 7.92 (d, J = 5.7 Hz, 2H), 7.83 (s, 2H), 7.57 (d, J = 6.0 Hz, 2H), 7.36 (d, J = 2.8 Hz, 2H), 7.19 (td, J = 8.7, 7.1, 4.1 Hz, 2H), 7.01 (ddd, J = 7.4, 5.9, 1.5 Hz, 2H), 6.66 (s, 2H), 6.11 (d, J = 8.4 Hz, 2H), 3.82 (d, J = 4.8 Hz, 6H)

Synthesis of [Ir(ppyOH)₂L]$^+$PF₆$^-$, (L= phenanthroline, Ir-phen; biquinoline, Ir-bq; 4,4'-di-tert-butyl-2,2'-dipyridyl, Ir-dtb) by BBr₃. This procedure was adapted based on previous methods reported in the literature.[67–71] [Ir(ppyOMe)₂L]$^+$PF$^-_6$ (L= biquinoline, phenanthroline)

was dried on a Schlenk line overnight. The vial was taken into the glovebox, and

[Ir(ppyOMe)$_2$L]PF$_6$ was dissolved in dichloromethane (8 mL). The reaction vial was then placed

in a cold well at –78 °C for 10 minutes with constant stirring. 1 M BBr$_3$ in dichloromethane (6

equiv, 1 equiv/OMe group) was then added dropwise into the cold reaction vial. The reaction

mixture produced fumes and changed colors from green to red (bq) or orange to yellow (phen).

The cold reaction was left to stir for 1 h at –78 °C. The cold bath beneath the well was removed,

and the reaction vial under stirring was allowed to warm up to room temperature overnight. The

sealed reaction vial was brought out of the glovebox and quenched by pouring it into a 10 mL

mixture of dichloromethane and water (1:1). The mixture was poured into a separatory funnel

and washed with water (3 x 15 mL). The dichloromethane layer was dried over MgSO$_4$ and

concentrated under reduced pressure to obtain the solid product that was orange (**Ir-phen**, 84

mg, 87% yield), forest green (**Ir-bq**, 8 mg, 48% yield), or yellow (**Ir-dtb,** 10 mg, 15% yield).

[Ir(ppyOH)$_2$phen]PF$_6$. MS (ESI LC-TOF): *m/e* [Ir(ppyOH)$_2$phen]$^+$- 713.07 ^{1}H NMR (499

MHz, Methanol-d_4) δ 8.77 (dd, *J* = 8.2, 1.4 Hz, 2H), 8.43 (dd, *J* = 5.0, 1.4 Hz, 2H), 8.31 (d, *J* =

4.5 Hz, 3H), 8.03 (d, *J* = 7.9 Hz, 2H), 7.94 (dd, *J* = 8.3, 5.1 Hz, 2H), 7.82 – 7.75 (m, 2H), 7.44

(d, *J* = 5.6 Hz, 2H), 7.39 – 7.33 (m, 3H), 6.93 – 6.82 (m, 2H), 6.60 (dd, *J* = 8.2, 2.6 Hz, 2H), 6.22

(d, *J* = 8.2 Hz, 2H).

[Ir(ppyOH)$_2$bq]PF$_6$. MS (ESI LC-TOF): *m/e* [Ir(ppyOH)$_2$bq]$^+$- 789.13 ^{1}H NMR (499 MHz,

DMSO-d_6) δ 9.00 (d, *J* = 8.9 Hz, 1H), 8.92 (d, *J* = 8.8 Hz, 1H), 8.83 (dd, *J* = 8.6, 1.0 Hz, 3H),

8.60 (d, *J* = 8.7 Hz, 3H), 8.27 – 8.17 (m, 3H), 8.17 – 8.05 (m, 3H), 7.99 (dd, *J* = 8.8, 4.8 Hz, 1H),

7.93 – 7.77 (m, 4H), 7.70 (ddd, *J* = 8.1, 6.8, 1.2 Hz, 3H), 7.66 – 7.56 (m, 1H), 7.29 – 7.17 (m,

2H), 7.09 – 6.92 (m, 1H), 6.50 (d, *J* = 8.0 Hz, 1H), 5.88 (d, *J* = 8.2 Hz, 1H).

[Ir(ppyOH)₂dtb]PF₆. MS (ESI LC-TOF): *m/e* [Ir(ppyOH)₂dtb]$^+$- 801.27. ^{1}H NMR (499 MHz, Methanol-*d₄*) δ 8.70 (d, *J* = 6.0 Hz, 2H), 8.12 – 7.94 (m, 4H), 7.94 – 7.78 (m, 2H), 7.61 (d, *J* = 5.6 Hz, 4H), 7.33 (d, *J* = 16.2 Hz, 2H), 7.05 (dd, *J* = 15.9, 9.3 Hz, 2H), 6.55 (dd, *J* = 10.2, 7.8 Hz, 2H), 6.09 (t, *J* = 9.1 Hz, 2H), 1.47 (s, 18H).

Synthesis of Ru(bpy)₂Cl₂. RuCl₃·3H₂O, bipyridine, and LiCl were refluxed in dimethylformamide (50 mL) for 8 h while stirring. The reaction mixture was cooled to room temperature and acetone was added. The solution was then cooled to 0 °C. Filtering yielded a red to red-violet solution and a dark green-black microcrystalline product. The solid was washed three times with water followed by diethyl ether.

Synthesis of Ru(bpy)₂(dcbq). Ru(bpy)₂Cl₂·2H₂O and dcbq-(Na)₂ were added to N₂-saturated deionized water. It was then refluxed for 8 h under N₂. This resulted in the formation of a brick red precipitate that was filtered and washed with deionized water followed by acetone.

4.6 References

(1)   Tributsch, H. *Ionics (Kiel).* **2000**, *6*, 161–171.

(2)   Henderson, R. *Annu. Rev. Biophys. Bioeng.* **1977**, *6*, 87–109.

(3)   Britt, R. D.; Sayler, R. I.; Berben, L. A.; Thompson, E. J.; Sherbow, T. J.; Arnold, A. *Chem. - A Eur. J.* **2018**, *25* (2), 454–458.

(4)   Demianets, I.; Hunt, J. R.; Dawlaty, J. M.; Williams, T. J.; Loker, K. B. *Organometallics* **2019**, *38*, 200–204.

(5)   Luo, G.-G.; Zhang, H.-L.; Tao, Y.-W.; Wu, Q.-Y.; Tian, D.; Zhang, Q. *Inorg. Chem. Front.* **2019**, *6*, 343–354.

(6)   Demianets, I.; Hunt, J. R.; Dawlaty, J. M.; Williams, T. J. *Organometallics* **2019**, *38*, 200–204.

(7)   Tatum, L. A.; Foy, J. T.; Aprahamian, I. *J. Am. Chem. Soc* **2014**, *136*, 17438–17441.

(8)   Halpern, A. M.; McBane, G. C. *Experimental Physical Chemistry*; 2006.

(9)   Lakowicz, J. R. *Principles of Fluorescence Spectroscopy 2nd Ed.*; 1999.

(10)   Agmon, N. *J. Phys. Chem. A* **2005**, *109* (1), 13–35.

(11)   Förster, T. *Z. Elektrochem.* **1950**, *54*, 42.

(12)   Förster, T. *Z. Elektrochem.* **1950**, *54*, 531.

(13)   Grabowski, Z. R.; Rubaszewska, W. *J. Chem. Soc. Faraday Trans. 1* **1977**, *73*, 11–28.

(14)   Weber, K. *Z Phys. Chem. B* **1931**, *15*, 18.

(15)   Vos, J. G. *Polyhedron* **1992**, *11* (18), 2285–2299.

(16)   Arnaut, L. G.; Formosinho, S. J. *J. Photochem. Photobiol. A Chem.* **1993**, *75* (1), 1–20.

(17)   Clower, C.; Solntsev, K. M.; Kowalik, J.; Tolbert, L. M.; Huppert, D. *J. Phys. Chem. A* **2002**, *106* (13), 3114–3122.

(18)   Meyer, T. J. *Pure Appl. Chem.* **1986**, *58* (9), 1193–1206.

(19)   Juris, A.; Balzani, V.; Barigelletti, F.; Campagna, S.; Belser, P.; Zelewsky, A. Von. *Coord. Chem. Rev.* **1988**, *84*, 85–277.

(20)   Chen, P.; Meyer, T. J. *Chem. Rev.* **1998**, *98* (4), 1439–1477.

(21)   Thompson, D. W.; Ito, A.; Meyer, T. J. *Pure Appl. Chem.* **2013**, *85* (7), 1257–1305.

(22)   Giordano, P. J.; Bock, R.; Wrighton, M. S.; Interrante, L. V.; Williams, R. F. X. *J. Am. Chem. Soc.* **1977**, *99* (9), 3187–3189.

(23)   Giordano, P. J.; Bock, R.; Wrighton, M. S. *J. Am. Chem. Soc.* **1978**, *100*, 6960–6965.

(24)   Lay, P. A.; Sasse, W. H. F. *Inorg. Chem.* **1984**, *23* (12), 4123–4125.

(25)   Mesmaeker, A. K.; Jacquet, L.; Nasielski, J. *Inorg. Chem.* **1988**, *27*, 4507–4514.

(26)   Hosek, W.; Tysoe, S. A.; Gafney, H. D.; Baker, A. D.; Strekas, T. C. *Inorg. Chem.* **1989**, *28* (17), 1228–1231.

(27)   Shinozaki, K.; Kaizu, Y.; Hirai, H.; Kobayashi, H. *Inorg. Chem.* **1989**, *28* (13), 3675–3679.

(28)   Nazeeruddin, M. K.; Kalyanasundaram, K. *Inorg. Chem.* **1989**, *28*, 4251–4259.

(29)   Davila, J.; Bignozzi, C. A.; Scandola, F. *J. Phys. Chem.* **1989**, *93* (4), 1373–1380.

(30)   Chang, Y. J.; Laneman, S.; Hopkins, J. B. *Chem. Phys. Lett.* **1989**, *156* (5), 421–424.

(31)   Kalyanasundaram, K.; Nazeeruddin, M. K. *Inorganica Chim. Acta* **1990**, *171* (2), 213–216.

(32)   Das, S.; Saha, D.; Mardanya, S.; Sujoy, B. *Dalt. Trans.* **2012**, *41*, 12296–12310.

(33)   Maity, D.; Bhaumik, C.; Karmakar, S.; Baitalik, S. *Inorg. Chem.* **2013**, *52*, 7933–7946.

(34)   Stewart, D. J.; Concepcion, J. J.; Brennaman, M. K.; Binstead, R. A.; Meyer, T. J. *PNAS* **2013**, *110*, 876–880.

(35)   Suna, Y.; Ertem, M. Z.; Wang, W.; Kambayashi, H.; Manaka, Y.; Muckerman, J. T.; Fujita, E.; Himeda, Y. *Organometallics* **2014**, *33*, 6519–6530.

(36)   Maity, D.; Mardanya, S.; Karmakar, S.; Baitalik, S. *Dalt. Trans.* **2015**, *44*, 10048–10059.

(37)   Alazaly, A. M. M.; Amer, A. S. I.; Fathi, A. M.; Abdel-sha, A. A. *J. Photochem. Photobiol. A Chem.* **2018**, *364*, 819–825.

(38)   Leasure, R. M.; Sacksteder, L.; Nesselrodt, D.; Reitz, G. A.; Demas, J. N.; DeGraff, B. A. *Inorg. Chem.* **1991**, *30*, 3722–3728.

(39)   Liu, W.; Welch, T. W.; Thorp, H. H. *Inorg. Chem.* **1992**, *31*, 4044–4045.

(40)   Cummings, S. D.; Eisenberg, R. *Inorg. Chem.* **1995**, *34*, 3396–3403.

(41)   Tolbert, L. M.; Solntsev, K. M. *Acc. Chem. Res.* **2002**, *35* (1), 19–27.

(42)   Lowry, M. S.; Hudson, W. R.; Pascal, R. A.; Bernhard, S. *J. Am. Chem. Soc.* **2004**, *126* (19), 14129–14135.

(43)   Zhao, Q.; Liu, S.; Shi, M.; Wang, C.; Yu, M.; Li, L.; Li, F.; Yi, T. *Inorg. Chem.* **2006**, *45* (16), 1704–1711.

(44)   Wenger, O. S. *Chem. - A Eur. J.* **2011**, *17* (42), 11692–11702.

(45)   Leavens, B. B. H.; Trindle, C. O.; Sabat, M.; Altun, Z.; Demas, J. N.; Degraff, B. A. *J. Fluoresc.* **2012**, *22*, 163–174.

(46)   Kappaun, S.; Slugovc, C.; List, E. J. *Int. J. Mol. Sci.* **2008**, *9* (8), 1527–1547.

(47)   Wagenknecht, P. S.; Ford, P. C. *Coord. Chem. Rev.* **2011**, *255*, 591–616.

(48)   Miyaura, N.; Suzuki, A. *Chem. Rev.* **1995**, *95* (7), 2457–2483.

(49)   Nonoyama, M.; Yamasaki, K. *Inorg. Nucl. Chem. Lett.* **1971**, *7*, 943–946.

(50)   Li, J.; Djurovich, P. I.; Alleyne, B. D.; Tsyba, I.; Ho, N. N.; Bau, R.; Thompson, M. E.

Polyhedron **2004**, *23*, 419–428.

(51)   Sauve, G.; Cass, M. E.; Coia, G.; Doig, S. J.; Lauermann, I.; Pomykal, K. E.; Lewis, N. S. *J. Phys. Chem. B* **2000**, *104* (29), 6821–6836.

(52)   Hoertz, P. G.; Staniszewski, A.; Marton, A.; Higgins, G. T.; Incarvito, C. D.; Rheingold, A. L.; Meyer, G. J. *J. Am. Chem. Soc.* **2006**, *128* (25), 8234–8245.

(53)   B Drew, M. G.; Harding, C. J.; McKee, V.; M, G. G.; Ne, J. *J. Chem. Soc. Chem. Commun.* **1995**, *0*, 1035–1038.

(54)   Du, K.; Thorarinsdottir, A. E.; David Harris, T. *J. Am. Chem. Soc* **2019**, *141*, 52.

(55)   Dragonetti, C.; Falciola, L.; Mussini, P.; Righetto, S.; Roberto, D.; Ugo, R.; Valore, A.; De Angelis, F.; Fantacci, S.; Sgamellotti, A.; Ramon, M.; Muccini, M. *Inorg. Chem.* **2007**, *46* (21), 8533–8547.

(56)   Frey, J.; Curchod, B. F. E.; Scopelliti, R.; Tavernelli, I.; Rothlisberger, U.; Nazeeruddin, M. K.; Baranoff, E. *Dalton Trans.* **2014**, *43* (15), 5667–5679.

(57)   Ladouceur, S.; Fortin, D.; Zysman-Colman, E. *Inorg. Chem.* **2010**, *49* (12), 5625–5641.

(58)   Zanoni, K. P. S.; Kariyazaki, B. K.; Ito, A.; Brennaman, M. K.; Meyer, T. J.; Iha, N. Y. M. *Inorg. Chem.* **2014**, *53*, 4089–4099.

(59)   Rosenkoetter, K. E. Synthesis and Reactivity of Transition Metal Complexes Bearing the Tridentate Bis(2-mercapto-p-tolyl)amine ([SNS]H3) Ligand, 2017.

(60)   Saouma, C. T.; Kaminsky, W.; Mayer, J. M. *J. Am. Chem. Soc.* **2012**, *134*, 7293–7296.

(61)   University of Basel: Department of Physics. Fluorescence and Phosphorescence https://fp.physik.unibas.ch/documents/fp28_Fluorescence_ and_Phosphorescence.pdf

(accessed Apr 12, 2015).

(62)   Kilislioglu, A.; Tepavcevic, S. *Photophysics and Molecular Spectroscopy: Excited State Properties of 2-Naphthol*; 2010.

(63)   Harris, C. M.; Selinger, B. K. *J. Phys. Chem.* **1980**, *84* (1), 255.

(64)   Pines, E.; Huppert, D. *J. Chem. Phys* **1986**, *84*, 3576–3577.

(65)   Labrie, F.; Singh, S.; Gauthier, S.; Frechette, Y.; Chenard, S.; Breton, R. Helix 12 Directed Steroidal Pharmaceutical Products. WO2005066194, 2005.

(66)   Peng, T.; Yang, Y.; Liu, Y.; Ma, D.; Hou, Z.; Wang, Y. *Chem. Commun.* **2011**, *47* (11), 3150–3152.

(67)   Snyder, S. a; Zografos, A. L.; Lin, Y. *Angew. Chem. Int. Ed. Engl.* **2007**, *46* (43), 8186–8191.

(68)   Pawlak, J. M.; Khau, V. V.; Hutchison, D. R.; Martinelli, M. J. *J. Org. Chem.* **1996**, *61* (8), 9055–9059.

(69)   Yamashita, T.; Kawai, N.; Tokuyama, H.; Fukuyama, T. *J. Am. Chem. Soc.* **2005**, *127*, 15038–15039.

(70)   Cheng, C.; Pan, L.; Chen, Y.; Song, H.; Qin, Y.; Li, R. *J. Comb. Chem.* **2010**, *12*, 541–547.

(71)   Cheng, P.; Clive, D. L. J.; Fernandopulle, S.; Chen, Z. *Chem. Commun.* **2013**, *49* (6), 558–560.